



A new variational wave function with backflow correlations for frustrated Hubbard models

Thesis submitted for the degree of
Doctor Philosophiae

Candidate:
Luca Fausto Tocchio

Supervisors:
Prof. Sandro Sorella
Dr. Federico Becca

October 2008

Contents

Introduction	iii
Overview	ix
1 Mott insulators and Spin liquids	1
1.1 Experimental examples	2
1.1.1 Transition-metal oxides	2
1.1.2 Layered organic salts	3
1.1.3 Cs_2CuCl_4	5
1.1.4 Herbertsmithite	8
1.2 The concept of spin liquid	9
1.3 The Hubbard model	12
1.4 The Heisenberg model	15
2 The variational approach	19
2.1 Variational Monte Carlo	20
2.2 Variational wave functions	24
2.2.1 The variational approach in the Heisenberg model	25
2.2.2 The variational approach in the Hubbard model	26
2.3 Backflow wave function	30
2.4 Comparison with the S -matrix strong-coupling expansion	33
2.5 The minimization algorithm	34
2.5.1 The logarithmic derivative of the backflow pa- rameters	40
2.6 Green's Function Monte Carlo	41
2.6.1 Importance sampling	43
2.6.2 Forward walking technique	44
2.6.3 Many walker formulation	46
2.6.4 Fixed Node approximation	47
2.7 Testing the accuracy of the backflow wave function . .	49

3	The square lattice	57
3.1	Connection with the Heisenberg model	60
3.2	The variational phase diagram	61
3.3	Green's Function Monte Carlo on the square lattice . .	68
4	The triangular lattice	71
4.1	The anisotropic triangular lattice with $t > t'$	73
4.2	The anisotropic triangular lattice with $t' > t$	78
	Conclusions and perspectives	87
	Acknowledgments	91
	Bibliography	93

Introduction

Quantum theory of solids developed after the famous Bloch's theorem, in which Schrodinger's equation was solved for a system of non-interacting electrons, leaving in a periodic potential generated by the ions. This theory led to a good understanding of the electronic properties, like conductance or specific heat, for many different materials (For a detailed review see Ref. [1, 2, 3]). If electron-electron interaction is added as a perturbation, its only effect is to renormalize the various bands and electrons can still be treated as non-interacting particles. In particular, a theory for the interacting gas of electrons has been developed by Landau [4] and predicts that the excitations close to the Fermi surface can be described as non-interacting "quasiparticles", that is particles dressed by the interaction.

Within the independent-electron approach, it is possible to distinguish in a straightforward way a metal from an insulator, by simply looking at the filling of the electronic bands. Indeed, an odd number of electrons per unit cell naturally implies a partially filled conduction band and, therefore, a metallic behaviour. Nevertheless, it is experimentally observed that, when electron-electron repulsion is sufficiently strong, the independent-electron picture fails and the system can be insulating even with an odd number of electrons per unit cell. These materials are called *Mott insulators* [5] and were experimentally observed for the first time within the family of transition-metal compounds [6].

In these materials, a transition-metal atom is surrounded by ligand atoms with a strong tendency towards negative valence, like Oxygen. Valence electrons have a predominant *d* character, that implies a very small overlap between the atomic states on nearest-neighbour atoms. Discrepancies with the independent-electron approach can be observed comparing experimental data on photoemission spectra with the results of band-structure calculations, based, e.g., on the local-density approximation [7]. In Fig. (1) data are shown for five transition-metal compounds varying the ratio between the effective on-site Coulomb repulsion U_{eff} and the bandwidth W for *d*-band electrons. Photoemission spectra of ReO_3 are in agreement with band structure calcula-

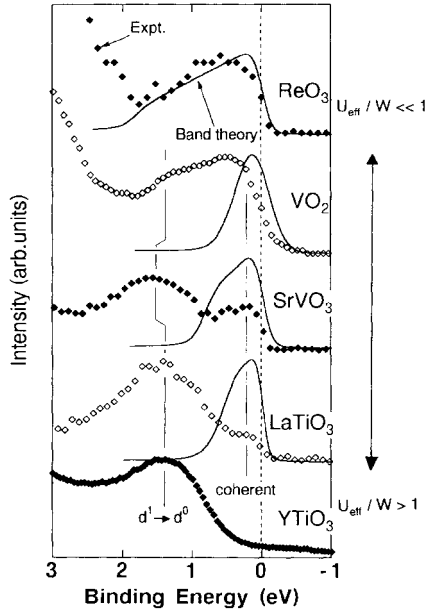


Figure 1: Photoemission spectra (diamond symbols) for various transition-metal compounds, in the d -band region. The ratio U_{eff}/W increases from top to bottom. Data are compared with the density of states given by band-structure calculations (solid curves) [8].

tions, because, due to the extended nature of the Re $5d$ wave functions, $U_{\text{eff}}/W \ll 1$. Then, going from VO_2 to LaTiO_3 , the peak around the Fermi energy becomes weaker and weaker, while there is the appearance of a new peak at $\sim 1.5\text{eV}$, that is not predicted by a theory of non-interacting electrons, and can be attributed to an effect of the electron-electron repulsion. Indeed, in the insulating YTiO_3 , the only feature is the $\sim 1.5\text{eV}$ peak, that has no counterpart in the calculated density of states [8].

Nowadays, a lot of attention is focused on a particular class of Mott insulators that can exhibit a paramagnetic insulating state down to zero temperature, the so-called *spin liquid*. Experimental signatures of such a state has been recently discovered in some materials that have an almost bidimensional crystal structure with a triangular or a Kagomé lattice [9, 10, 11, 12, 13, 14]. Indeed, they are examples of *frustrated* materials, where the presence of competing magnetic interactions may destroy or strongly suppress long-range magnetic order. Proving the existence of spin-liquid ground states is one of the greatest challenges in contemporary quantum condensed matter physics, since

the ground state of a classical Hamiltonian is always expected to be ordered at very low temperature. Moreover, a spin liquid may exhibit exotic behaviours, like fractional excited states, that is neutral excitations carrying non-integer values of the spin.

From a theoretical point of view, the description of a strongly-correlated electron model is another great challenge in condensed matter physics. In this thesis, we focus on the Hubbard model, where electrons move on a lattice within a tight-binding scheme and correlation is introduced through an on-site repulsive term U . Another widely used model is the Heisenberg one, that is the large- U limit of the Hubbard model, in which electrons are frozen on lattice sites and interaction is restricted to spin degrees of freedom. However, the total suppression of charge fluctuations offers a rather unrealistic picture of correlated insulators, where charge fluctuations are surely present at small length scales. Although these models are very simple in their formulation, they can be solved exactly only in one dimension, so that, in the interesting 2D case, we need accurate numerical techniques to describe their ground-state properties.

In particular, in this thesis, we deal with Monte Carlo techniques, that allow us to evaluate multidimensional integrals in a stochastic way. This is very useful for quantum many body problems, where, in general, the calculation of expectation values cannot be handled analytically, because the correlated wave function of the system cannot be factorized into one-particle states. We focus on Variational and Green's Function Monte Carlo techniques [15, 16, 17]. These approaches are based on an approximate form for the ground-state wave function which contains the physically relevant terms for the correct description of the Mott insulating state. In particular, we are interested in accurate wave functions to describe a spin-liquid ground state. For the Heisenberg model, this approach works remarkably well and a spin liquid can be stabilized [18, 19] by means of a fully-projected¹ BCS mean-field wave function. On the contrary, for the Hubbard model, spin-liquid wave functions are able to capture the metal-insulator transition by means of a long-range Jastrow factor [20], but they are poorly accurate in the insulating phase, so that magnetic ground states are always favoured.

The poor accuracy of the spin-liquid wave functions is particularly evident in the strong-coupling regime, where they fail to reproduce the super-exchange physics. In this respect, we look for an improvement of the wave function that mimics the effect of the virtual hopping, leading us to the super-exchange mechanism. Good candidates for this are the so-called *backflow* correlations, that were introduced a long time ago

¹With full projection we mean the complete neglect of doubly occupied sites.

by Feynman and Cohen [21] to obtain a quantitative description of the roton excitation in liquid Helium. The term backflow came out because it creates a return flow of current, opposite to the one computed with the original wave function.

The backflow term has been implemented within quantum Monte Carlo calculations to study bulk liquid ^3He [22, 23] and then applied to weakly correlated electron systems. In particular, backflow correlations turned out to be crucial in improving the description of the electron jellium model both in two and three dimensions [24, 25]. More recently, backflow has been applied also to metallic hydrogen [26] and to small atoms and molecules [27], where significant improvements in the total energy have been obtained.

Here, we have established that backflow correlations are crucial also in strongly correlated lattice models, to get a remarkably accurate ground-state energy. We have compared our results with exact calculations on small lattice sizes and also with other more established approaches, like the S -matrix expansion [28] at strong coupling or the Pfaffian ansatz to combine magnetism and superconductive pairing [29]. Moreover, by means of backflow correlations, we are able to fill up the difference between the energies of the spin-liquid state in the Hubbard model at increasing U and the energy obtained within the Heisenberg model, using the fully-projected BCS wave function [30].

We have applied backflow correlations to the trial wave functions that approximate the ground state of the Hubbard model on the square lattice with nearest and next-nearest neighbour couplings, t and t' . Indeed, this model represents a simple prototype for frustrated electronic materials: in the presence of a next-neighbour hopping t' there is no more the perfect nesting condition that, in the unfrustrated case, leads to antiferromagnetic order for any finite U . We have been able to stabilize a spin-liquid phase at strong coupling and large enough frustrating ratio t'/t , *only* by inserting backflow correlations [30]. Moreover, we settled the boundaries of two magnetically-ordered phases and the metal-insulator transition. Magnetic properties have been assessed by means of Green's Function Monte Carlo.

We focused also on the anisotropic triangular lattice, on which many experiments have been performed in recent years, with a great debate about the nature of the insulating region: commensurate magnetic order, spiral phases or spin liquid? We considered two main regimes of anisotropy: in one of them, where the lattice is a set of squares, frustrated by a weak diagonal bond, the insulating phase is magnetically ordered in a commensurate way. In the other regime, that corresponds to a set of weakly coupled chains, there are evidences that backflow

correlations favour a spin-liquid phase with one-dimensional features [31].

Overview

The thesis is organized as follows:

- In chapter 1, we introduce the key concepts of Mott insulator and spin liquid, focusing, in particular, on the property of a spin-liquid phase. We also present the main experiments where a Mott insulating and, especially, a spin-liquid behaviour has been observed. The chapter closes with a detailed description of the Hubbard and the Heisenberg Hamiltonians, which can capture the physics of strongly-correlated electron systems.
- In chapter 2, we introduce the electronic wave functions used to approximate the exact ground state of correlated models. We focus in particular on backflow correlations, that we apply, for the first time, on a lattice model. Moreover, we introduce the numerical techniques used in this thesis. We describe the Variational Monte Carlo method, the optimization algorithm and Green's Function Monte Carlo with the fixed-node approximation. In the last part of the chapter, we compare our results for the Hubbard model with the exact ones on small lattice sizes and with other established approaches.
- In chapter 3, we present our phase diagram for the Hubbard model on the square lattice with nearest and next-nearest neighbour couplings. A particular emphasis is given on the spin liquid phase, we can stabilize at strong coupling and large enough frustration, by means of backflow correlations. Our results are compared with the other ones existing in literature.
- In chapter 4, we present our results on the triangular lattice in presence of anisotropy, focusing on two main regimes. In one case, the ground state is magnetically ordered, while in the other one there are evidences that backflow correlations favour a spin-liquid nature of the ground state, with one-dimensional features.

Chapter 1

Mott insulators and Spin liquids

Since its early applications, the independent-electron approach has led to a good understanding of the electronic properties of many different materials. In this theory, the electrons are treated as non-interacting particles, leaving in a periodic potential generated by the ions. This scheme allows one to distinguish in a straightforward way a metal from an insulator by simply looking at the filling of the electronic bands. Indeed, if electron-electron interaction is added as a perturbation, its only effect is to renormalize the various bands and electrons can still be treated as non-interacting particles. Therefore, the metallic or insulating behaviour is determined only by the existence of an energy gap between the highest occupied level and the lowest unoccupied one. Within this picture, an odd number of electrons per unit cell naturally implies a partially filled conduction band, and, therefore, a metallic behaviour. Nevertheless, it is experimentally observed that, when electron interaction is sufficiently strong, the independent-electron picture fails and the system can be insulating even with an odd number of electrons per unit cell. These materials, whose insulating character is induced by electron correlation, are called *Mott insulators* [5].

The interest in the physics of Mott insulators is strongly increased soon after the discovery of High-temperature superconductors [32]. Indeed, all these kinds of materials are characterized by a universal phase diagram where superconductivity emerges upon doping a Mott insulator.

We present, in the first section of this chapter, various experimental examples of insulators driven by strong correlation, both in three and two dimensions. We start from the metal-transition compounds, in which a Mott insulating behaviour was firstly observed, and move

to a class of Mott insulators in two dimensions, that can exhibit a paramagnetic insulating state down to zero temperature, the so-called *spin liquid*. Within this class we may describe Layered Organic Salts, Cs_2CuCl_4 and Cs_2CuBr_4 , all with a triangular lattice, or the recently discovered Herbertsmithite ($\text{ZnCu}_3(\text{OH})_6\text{Cl}_2$), described by a $S = 1/2$ Kagomé lattice. All these materials are examples of frustrated systems, in which the presence of competitive magnetic interactions or the lattice geometry can contribute to destroy or strongly suppress the magnetic order.

In the second section we address in some detail the concept of spin liquid and the idea of frustration, that can favour disordered states. Then, in the third section we introduce microscopic Hamiltonians, which can capture the physics of strongly-correlated electron systems. We focus on the Hubbard model, in which electrons move on a lattice within a tight-binding scheme and correlation is introduced through an on-site repulsive term U . We also present in the fourth section the Heisenberg model, that is the large- U limit of the Hubbard model, in which electrons are frozen on lattice sites and interaction is restricted to spin degrees of freedom. These two models cannot be exactly solved in general, so we will introduce in the next chapter some numerical techniques that allow us to describe their ground state properties with very good accuracy.

1.1 Experimental examples

In the following, we will show different classes of materials where correlation plays a fundamental role. These systems are generally characterized by partially-filled valence bands and an insulating behaviour, implying the failure of the band-theory approach in predicting their properties. We start from the transition-metal compounds, in which a Mott insulating behaviour was firstly observed, and then we introduce the recently discovered two-dimensional compounds, that do not present any kind of magnetic order down to zero temperature, showing a spin-liquid behaviour.

1.1.1 Transition-metal oxides

The theoretical studies of electron correlation take origin from the transition-metal compounds [6], where a transition-metal atom is surrounded by ligand atoms with a strong tendency towards negative valence (i.e. Oxygen). In these materials, valence electrons have a predominant d character, that implies a very small overlap between the

atomic states on nearest-neighbour atoms. More precisely, the overlap is often determined by indirect transfer of d -orbitals through the ligand p orbitals of the atom located between the transition-metal atoms, contributing to create a narrow bandwidth.

The most celebrated transition-metal oxide, that displays a Mott insulating state, is Vanadium Sesquioxide (V_2O_3). This material crystallizes in a corundum structure, in which the V^{3+} ions are arranged in V-V pairs along the z axis and form a honeycomb lattice in the xy plane. Each V ion has a $3d^2$ electronic configuration and is surrounded by an octahedron of O atoms. One electron per V resides in a singlet bond among the V-V pairs; the remaining electron per V determines the electric and the magnetic properties of this material. The pure stoichiometric V_2O_3 is an antiferromagnetic insulator below $T_{\text{Neel}} \sim 160\text{K}$ at ambient pressure. The antiferromagnetic-paramagnetic transition at the Neel temperature is at the same time a metal-insulator transition, of first order character: the resistivity drops abruptly [33] after T_{Neel} . In order to observe a metal-insulator transition induced by bandwidth control, it is possible to apply pressure which, by compressing the lattice, widens the bands. Indeed, one finds that T_{Neel} decreases with increasing pressure and the antiferromagnetic phase is completely suppressed at $P \sim 24\text{Kbar}$. The effect of applying a positive pressure can be equally recast by substituting some V atoms with Ti impurities, since the Ti ions have smaller size. On the other hand, it is possible to increase the interatomic distance by introducing impurities that are bigger than the V ions. This is realized by substituting Cr atoms to V. Considering the $(V_{1-x}Cr_x)_2O_3$ system, one recovers, above a certain temperature, a paramagnetic insulating state. The resulting phase diagram [34] is shown in Fig. (1.1).

1.1.2 Layered organic salts

Layered organic materials are a very interesting example of strongly correlated systems in which frustration may play an important role into their magnetic and superconductive properties. Their lattice is essentially triangular in the layers and the inter-layer coupling is almost irrelevant. In general these materials are referred to as $k - (\text{ET})_2X$ or $k - (\text{BEDT-TTF})_2X$, where BEDT-TTF or ET denotes the bis(ethylenedithio)-tetrathiafulvalene, X indicates an organic monovalent anion and k defines the different arrangements of the molecules on each lattice site. The general structure is constituted by conducting ET layers, where couples of dimerized ET molecules are arranged into a triangular lattice, see Fig. (1.2). In each dimer, two degenerate highest-occupied molecular orbitals (HOMO) belonging to each

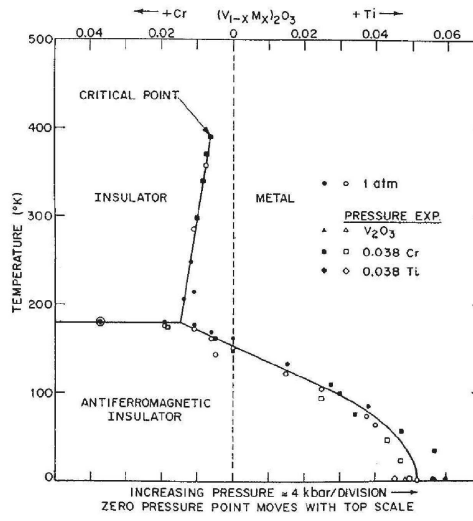


Figure 1.1: Generalized phase diagram of V_2O_3 as a function of doping with Cr or Ti (which corresponds to vary the pressure) and as function of temperature [34].

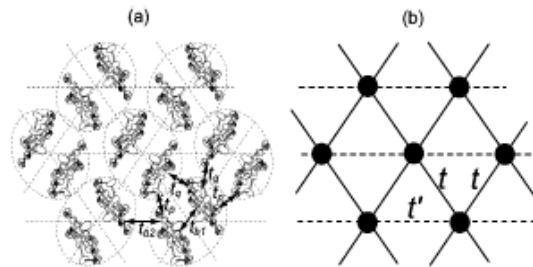


Figure 1.2: Crystal structure of an ET layer for $k-(ET)_2Cu_2(CN)_3$. Couples of ET molecules dimerize and can be regarded as a dimer unit sitting on a site of a triangular lattice.

ET molecule are split into bonding and anti-bonding HOMO's, forming two bands that are separated by an energy gap. Since one hole is introduced into the dimer by the ion X , the upper band, which is the anti-bonding HOMO band, is half filled, while the lower one does not participate to the conduction.

In this section we focus on the $k - (\text{ET})_2\text{Cu}_2(\text{CN})_3$ compound that was studied by Kanoda's group [9, 10]. The crystal structure of the conducting layers is triangular, and the lattice is almost isotropic. Indeed, the ratio of the transfer integrals t and t' is almost unity, $t'/t = 1.06$; this number was calculated by means of quantum chemistry calculations, using the Hückel approximation [35]. The compound was studied first at ambient pressure [9], mainly by means of Nuclear Magnetic Resonance (NMR), and no long-range magnetic ordering was observed down to 32 mK. Indeed, no splitting was observed in the NMR absorption spectra, see Fig. (1.3). These results are in sharp contrast with another Mott insulator $k - (\text{ET})_2\text{Cu}[\text{N}(\text{CN})_2]\text{Cl}$ with $t'/t \sim 0.75$, which exhibits the magnetic transition at $T_N = 27$ K, at ambient pressure, see Fig. (1.3). The transition is denoted by a splitting in the NMR absorption spectrum.

In a subsequent work [10] the pressure-temperature phase diagram was proposed, see Fig. (1.4). They reported on the NMR and resistance studies of the Mott transition under pressure. By increasing pressure, the spin liquid phase gives way to a metal or superconducting phase. In addition, there is a metallic crossover region close to the insulator where a deviation from the Fermi-liquid features was observed, like in the temperature dependence of resistivity.

1.1.3 Cs_2CuCl_4

Actually, the first experimental example of a Mott insulator showing a spin liquid behaviour is the compound Cs_2CuCl_4 , which was studied by R. Coldea and coworkers [11]. The structure of this material would be orthorhombic, but the very small interlayer coupling allows us to consider this material as a sum of almost independent layers with a 2D triangular structure. Since electron-electron repulsion is quite strong in this material, the authors considered the spin-spin interaction J , instead of the hopping parameter t . The lattice in each layer is anisotropic, indeed, the spin-spin interaction J (referred to the full-line bonds in Fig. (1.2)) is about one third of J' (referred to the dashed-line bonds); data on the interaction parameters are obtained experimentally. The compound was studied at ambient pressure using neutron scattering measurements: while below $T_N = 0.62\text{K}$ the small interlayer coupling stabilizes 3D magnetic order, at higher temperatures a spin

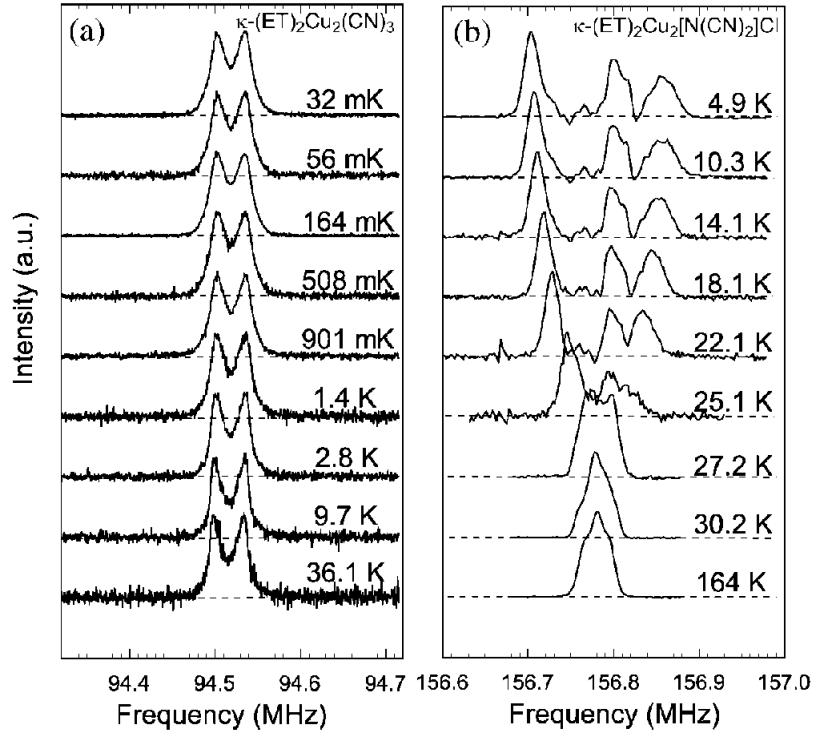


Figure 1.3: ^1H NMR absorption spectra for single crystals of $\kappa\text{-(ET)}_2\text{Cu}_2(\text{CN})_3$ and $\kappa\text{-(ET)}_2\text{Cu}_2[\text{N}(\text{CN})_2]\text{Cl}$ under the magnetic field perpendicular to the conducting planes [9].

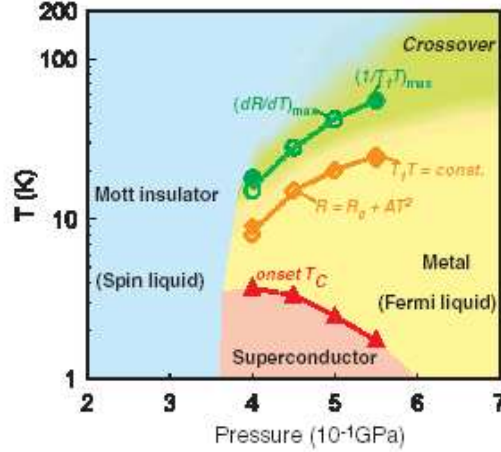


Figure 1.4: The pressure-temperature phase diagram of $k-(\text{ET})_2\text{Cu}_2(\text{CN})_3$, constructed on the basis of resistance and NMR measurements, under hydrostatic pressure [10].

liquid phase is observed. In Fig. (1.5) the neutron scattering intensity as a function of energy is shown, in the ordered phase at 0.1 K and in the paramagnetic phase at 15 K. The magnetic peak disappears at 15 K and is replaced by a broad paramagnetic signal. Because in a neutron scattering process the total spin changes by $\Delta S_{\text{total}} = 0$ or 1, the absence of single particle peaks and the presence of excitation continua may imply that the underlying excitations carry fractional quantum numbers. This kind of excitations will be briefly discussed in the next section.

Magnetic fields applied within the 2D planes are able to suppress completely long-range order, at least down to 35 mK, above 2.1 T.

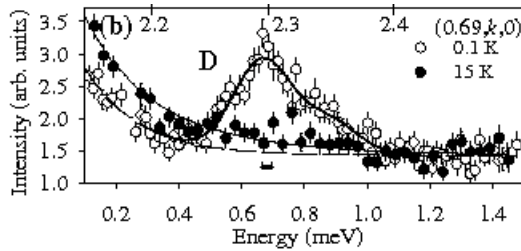


Figure 1.5: Neutron scattering intensity as a function of energy in the magnetically ordered phase at 0.1 K (open circles) and in the paramagnetic phase at 15 K (solid circles) [11].

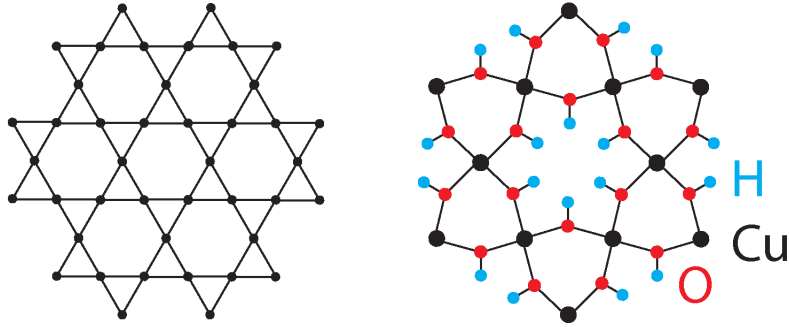


Figure 1.6: Lattice structure of $\text{ZnCu}_3(\text{OH})_6\text{Cl}_2$. The Cu layers have a Kagomé crystal structure.

Susceptibility measurements showed no evidence of a phase transition between the spin liquid behaviour in zero field above $T_N = 0.62\text{K}$ and the disordered phase found for fields greater than 2.1 T. This indicates that fields applied within the 2D planes stabilize the fractional spin-liquid state.

1.1.4 Herbertsmithite

The compound $\text{ZnCu}_3(\text{OH})_6\text{Cl}_2$, known as herbertsmithite, is the first experimentally studied material [12, 13, 14], with $\text{spin}=1/2$ and crystal structure described by a 2D Kagomé lattice, that is a lattice of corner-sharing triangles, see Fig. (1.6). Indeed, $\text{ZnCu}_3(\text{OH})_6\text{Cl}_2$ consists of Cu Kagomé layers separated by non-magnetic Zn layers.

The Kagomé lattice received a lot of theoretical interest, before it was experimentally studied. The huge degeneracy in the classical ground state has led to consider this lattice suitable for a spin-liquid ground state. Theories based on numerical diagonalization or approximate solutions of the Heisenberg Hamiltonian favour non-magnetic ground states [36], that do not break any symmetry of the Hamiltonian [37] and put an upper limit on the excitation gap to magnetic $\Delta S = 1$ excitations of $J/20$, where J is the energy scale in the Heisenberg Hamiltonian [38]. The magnetic gap is filled with a continuum of low-lying singlet excitations.

Recent experiments performed in Ref. [12], using neutron scattering measurements, show an excitation spectrum consistent with the picture of deconfined spinons in a spin liquid. They found no evidence of a spin gap down to $J/170$, much lower than the prediction from exact diagonalization studies [38]. Moreover, their observation of a diffusive

momentum dependence for the inelastic scattering suggests that if a singlet spin-liquid picture is correct, than the singlets are not restricted to nearest-neighbour dimers, because no well defined length scale is indicated by the data. These observations are coherent with the picture of gapless excitations carried by $S = 1/2$ spinons.

Moreover, in Ref. [13] Ofer and coworkers performed spin susceptibility measurements as a function of the magnetic field. They observed no peak in the susceptibility, indicating the absence of magnetic ordering. They also performed experiments using nuclear magnetic measurements, based in particular on the spin-lattice relaxation rate, finding a negligibly small gap between the ground state and the first magnetic excitation.

Finally also in Ref. [14], a study based on muon spin rotation did not find evidence of a magnetic transition down to 50 mK. Moreover, a study of the whole family $\text{Zn}_x\text{Cu}_{4-x}(\text{OH})_6\text{Cl}_2$, was performed, varying the concentration of Zn and Cu. A crossover from a paramagnetic-like ground state to a magnetically ordered one was observed around $x = 0.5$.

1.2 The concept of spin liquid

Here, we want to discuss the concept of spin liquid, emerging when magnetic long-range order is destroyed by quantum fluctuations, at zero temperature. The formation of a spin-liquid phase is favoured when three conditions are met: a low value of the spin, the presence of frustrating couplings and a low dimensionality. Indeed, low values of the spin, like in an electron system where $S = 1/2$, favour a spin liquid phase, while higher values of the spin are less affected by quantum fluctuations and tend to form ordered ground states. Another element that favours disordered ground states is the presence of frustration, leading to competing magnetic interactions, that can destroy long-range order. In Fig. (1.7) we show two frustrated lattices studied in this thesis. In the triangular one, frustration has a topological origin, while on the square lattice frustration is introduced by extending spin interaction to next-nearest neighbours. Finally, also low dimensionality can help the ground state to be a spin liquid. Indeed, quantum fluctuations become more and more important when the dimensionality is lowered: in one dimension no magnetic long-range order is possible, in two dimensions many experiments suggest the existence of a spin-liquid ground state, while in three dimensions spin liquids are theoretically possible, but a priori more difficult to observe, mostly because Neel ordered states are more stable in higher dimensions. However, much effort is now devoted

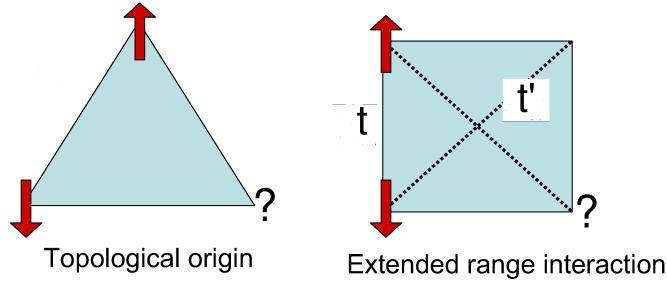


Figure 1.7: Frustrated antiferromagnetic interactions on the triangular lattice and on the square lattice with coupling extended to next-nearest neighbours.

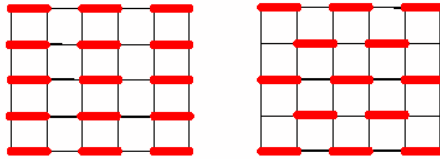


Figure 1.8: Examples of valence-bond crystals on the square lattice. Singlets are indicated by red thick lines.

to the study of disordered ground states in frustrated 3D lattices, like the pyrochlore one [39].

The precise definition of a spin liquid may be subtle. A first one can be to define spin liquids as states without magnetic long-range order at $T = 0$. However, within this class, there are also the so-called valence-bond crystals, which present a broken translational symmetry, forming a dimer order. These states can be pictured by considering a collection of short-range singlets that form some pattern (see Fig. (1.8)). Since there is the breaking of some lattice symmetry, the ground state is degenerate and there is a gapped spectrum. In fact, excitations with $\Delta S = 1$ may be obtained by breaking a singlet (where in general the true excitation will be dressed by singlet-singlet interaction).

A possible more refined definition could characterize a spin liquid as a state without any spontaneously broken symmetry, at $T = 0$. This definition excludes Neel ordered states, which break the $SU(2)$ symmetry, and also valence-bond crystals, which break some lattice symmetries. However, within this definition we still have to distinguish between an even and an odd number of electrons per unit cell. In the first case, like on a 2-leg ladder (see Fig. (1.9)), the singlets can form a

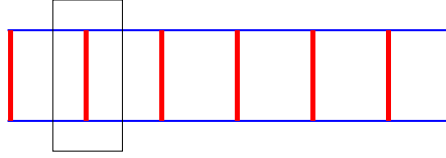


Figure 1.9: Example of a 2-leg ladder. The singlets accommodate along the rungs. The black square encloses an unit cell.

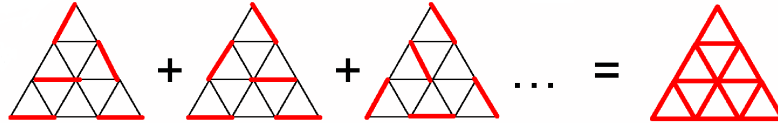


Figure 1.10: Example of a short-range RVB state on the triangular lattice, as a linear superposition of valence-bond configurations.

pattern that accommodates in a unit cell, without breaking any lattice symmetry. As a consequence, the ground state is non-degenerate, with a finite gap to $\Delta S = 1$ excitations.

On the contrary, if the ground state does not break any symmetry *and* accommodates an odd number of electrons per unit cell, a genuine spin liquid is possible. A convenient description can be achieved by the so-called Resonant Valence Bond (RVB) state [40], constructed as a linear superposition of valence-bond configurations, that can be short-range or long-range, in order to recover a spatially uniform state (see Fig. (1.10)). The system resonates among the various valence-bond configurations, recalling the Pauling idea of resonance in the benzene molecule. The RVB state can be either gapless with a non-degenerate ground state or gapped with a topological degeneracy in the ground state [41]. However, the key ingredient of a RVB state is *fractionalization*, that is the elementary excitations (called spinons) carry fractional spin $\Delta S = 1/2$, instead of $\Delta S = 1$.

This behaviour is in sharp contrast with valence-bond crystals, where the only possible excitations have integer values of the spin. Indeed, as sketched in Fig. (1.11), after the creation of the basic excitation, that is a triplet, with energy cost J , the two excited spins can travel in the lattice, modifying the pattern of singlets. However, the two spins cannot move independently as $S = 1/2$ excitations: as the distance r between the spins increases, the loss in energy $V(r)$ becomes bigger. When $V(r)$ reaches $2J$, it is more convenient to create

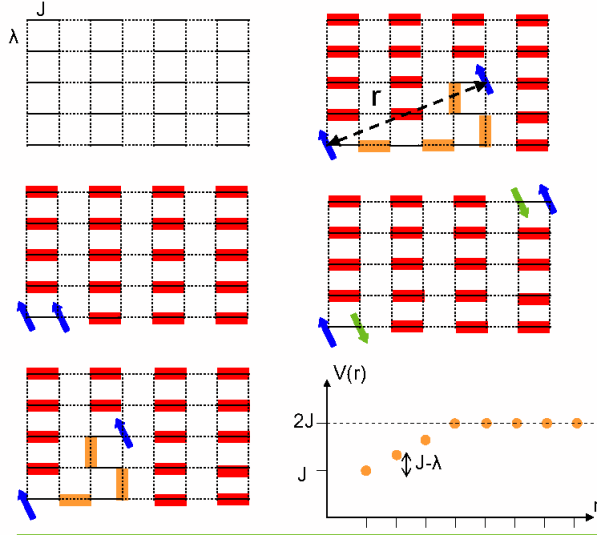


Figure 1.11: Model pattern of singlets on the square lattice. Singlets lie on the bonds with continuous lines, gaining an energy J , while singlets that lie on the dotted bonds would gain only an energy $\lambda \ll J$. When a triplet excitation forms, the two excited spins can propagate in the lattice modifying the pattern of singlets, with an increasing loss of energy $V(r)$. When $V(r)$ is equal to $2J$ two independent triplets form.

two triplets than to let the distance r increase more. On the contrary, since in the RVB state there is no dimer order and the singlets resonate among all the possible configurations, the two spinons can propagate freely, as independent excitations with $\Delta S = 1/2$.

1.3 The Hubbard model

The Hubbard model is the simplest example of a microscopic Hamiltonian that takes into account the electron-electron interaction and its competition with the kinetic energy. It was independently introduced by Hubbard [42], Gutzwiller [43] and Katsmori [44] in order to understand magnetism in transition metals. Currently it is widely used in order to understand strongly-correlated electron systems, like the ones described in the experimental section.

We focus on the one-band Hubbard Hamiltonian, defined on a lattice of L sites. The assumption *one band* means that only one Wannier state per site is considered. This approximation is valid when the Fermi energy lies within a single conduction band, implying an irrelevant con-

tribution of the other bands. The Hamiltonian can be written as:

$$\mathcal{H} = - \sum_{i,j,\sigma} t_{ij} c_{i,\sigma}^\dagger c_{j,\sigma} + U \sum_i n_{i,\uparrow} n_{i,\downarrow}, \quad (1.1)$$

where $c_{i,\sigma}^\dagger (c_{i,\sigma})$ creates (destroys) an electron with spin σ on site i and $n_{i,\sigma} = c_{i,\sigma}^\dagger c_{i,\sigma}$ is the occupation number operator. Since only one atomic level per atom is considered, each lattice site can appear in four different quantum states:

$$\begin{aligned} &|0\rangle_i \text{ site } i \text{ empty} \\ &|\uparrow\rangle_i = c_{i,\uparrow}^\dagger |0\rangle \text{ site } i \text{ occupied by an } \uparrow \text{ electron} \\ &|\downarrow\rangle_i = c_{i,\downarrow}^\dagger |0\rangle \text{ site } i \text{ occupied by a } \downarrow \text{ electron} \\ &|\uparrow\downarrow\rangle_i = c_{i,\uparrow}^\dagger c_{i,\downarrow}^\dagger |0\rangle \text{ site } i \text{ doubly occupied.} \end{aligned} \quad (1.2)$$

The first term in Eq. (1.1) expresses the kinetic part \mathcal{K} , which delocalizes the N electrons among the lattice. The hopping parameters t_{ij} control the bandwidth of the system and depend on the overlap between orbitals on sites i and j :

$$t_{i,j} = \int dr \phi_i^*(r) \left(\frac{\nabla^2}{2m} + V_{\text{ion}} \right) \phi_i(r), \quad (1.3)$$

where $\phi_i(r)$ is a Wannier orbital centered on site i and V_{ion} is the potential created by the positive ions forming the lattice. We work in a translationally invariant system, in which the parameters t_{ij} depend only on the distance among the sites i and j on the lattice. Furthermore, we regard the hoppings parameters as non-zero only if the sites i and j are nearest neighbours or, at most, next-nearest neighbour sites. The kinetic term \mathcal{K} can be diagonalized in a basis of Bloch states:

$$\mathcal{K} = \sum_{k,\sigma} \epsilon_k c_{k,\sigma}^\dagger c_{k,\sigma} \quad \epsilon_k = -2t \sum_{i=1}^d \cos(k_i), \quad (1.4)$$

where $c_{k,\sigma}^\dagger$ is the Fourier transform of $c_{i,\sigma}^\dagger$ and a d -dimensional cubic lattice has been assumed.

The second term in Eq. (1.1) is the Coulomb repulsion between two electrons sharing the same orbital:

$$U = \int dr_1 dr_2 |\phi_i(r_1)|^2 \frac{e^2}{|r_1 - r_2|} |\phi_i(r_2)|^2, \quad (1.5)$$

that is just the short-range part of the true Coulomb interaction.

Since the Hubbard Hamiltonian is the sum of two terms, one diagonal in real space and the other one diagonal in Fourier space, an exact solution of this model is missing in general and the model can be exactly solved only in one dimension [45]. Then, we need approximate numerical techniques to study the ground state properties. In next chapter, we will introduce in some detail the numerical methods used in this thesis to afford the Hubbard model on the square and on the triangular lattice.

However, we can draw some general considerations on the ground state properties of the Hubbard model. Indeed, the form of the Hubbard Hamiltonian suggests that its phase diagram comes out from two opposite tendencies: from one side the hopping term tends to delocalize the electrons in the crystal and from the other side the interaction term encourages the electrons to occupy different sites, otherwise the system must pay an energy cost U per each doubly occupied site. Whenever the electron density is away from *half-filling*, i.e., $n = N/L \neq 1$, the number of holes or doubly occupied sites is always different from zero and charge fluctuations are possible with a small energy cost. In this case, the ground state of the system is predicted to be metallic for every value of the ratio U/t , where t is an hopping integral that is taken as the energy scale. Furthermore, the possible occurrence of superconductivity in the Hubbard model for $n \neq 1$ has been widely investigated and there are now important evidences that superconductivity emerges at finite doping [46]. Instead, at *half-filling* ($n = 1$) each site is, in average, singly occupied. The two tendencies of delocalizing and localizing the electrons depend on the ratio U/t and on the level of frustration present in the system. However, regardless of frustration, for $U/t = 0$ the system is a non-interacting metal, while for $t/U = 0$ the system is an insulator with no charge fluctuations. The presence of these two limiting cases suggest the existence of a phase transition at a finite value of U/t : the *Mott metal-insulator transition*. As we will present in the forthcoming, the effect of frustration is to modify the critical U at which the metal-insulator transition occurs. However, the role of frustration can be more dramatic in determining the magnetic properties in the insulating phase. While an unfrustrated lattice has an instability towards magnetic ordering as soon as $U/t > 0$ [47], the presence of frustration, leading to competing magnetic interactions, can destroy long-range order and open the route to a spin-liquid state.

In the following, we show briefly that the Hubbard model has a tendency towards antiferromagnetic order on a hypercubic lattice at half filling with only nearest-neighbour couplings, that is the prototype of a lattice without frustration. This is strictly true in more than one

dimension, where quantum fluctuations destroy magnetic order and the system is a non-magnetic insulator, in which spin correlations decay with a power-law [48]. Using the Random-Phase Approximation, we can get the following expression for the spin susceptibility $\chi(\mathbf{Q})$, where \mathbf{Q} is the pitch vector corresponding to a given magnetic order:

$$\chi(\mathbf{Q}) \sim \frac{\chi^0(\mathbf{Q})}{1 - U\chi^0(\mathbf{Q})}, \quad (1.6)$$

where the bare susceptibility $\chi^0(\mathbf{Q})$ is given by:

$$\chi^0(\mathbf{Q}) = \frac{1}{L} \sum_k \frac{f_k - f_{k+\mathbf{Q}}}{\epsilon_{k+\mathbf{Q}} - \epsilon_k}, \quad (1.7)$$

f_k is the Fermi occupation number and ϵ_k are the energy levels associated to the unperturbed ground state at $U = 0$. The magnetic instability occurs when the denominator in Eq. (1.6) vanishes, i.e., for $U\chi^0(\mathbf{Q}) = 1$. This condition is known as the Stoner criterion. If we consider standard antiferromagnetic Neel order in two dimensions, the pitch vector is $\mathbf{Q} = (\pi, \pi)$; then, since on a square lattice with only nearest neighbour couplings, the Fermi vector k_F satisfies a perfect nesting condition, i.e. $\epsilon_{k_F+\mathbf{Q}} = \epsilon_{k_F}$, there is a divergence, like $\ln^2(L)$, in $\chi^0(\mathbf{Q})$ at $\mathbf{Q} = (\pi, \pi)$. Since the bare susceptibility diverges, the Stoner criterion signals a tendency towards antiferromagnetic ordering for any non-zero U .

1.4 The Heisenberg model

In the following, we want to introduce briefly the Heisenberg model, that is the limit of the Hubbard model when U/t goes to infinity, at half-filling. The Heisenberg model is the simplest one to describe an insulator, because there are no charge degrees of freedom and electron interaction is restricted to the spin sector. In order to derive the Heisenberg model from the infinite- U limit of the Hubbard one, we start from a fully insulating state with exactly one electron per lattice site. This state is 2^L degenerate, where L is the number of lattice sites, because we can accommodate electrons with spin up or down on every site. Then we add the kinetic term \mathcal{K} in the Hubbard Hamiltonian (1.1), using second-order perturbation theory, to the degenerate manifold of ground states. Let us focus on two states which only differ in the spin configurations of two nearest neighbour sites: $|\sigma_i\sigma_j\rangle$ and $|\sigma'_i\sigma'_j\rangle$. Within second order in t we obtain a matrix element between these two states

given by¹:

$$t^2 \sum_n \sum_{\sigma, \sigma'} \langle \sigma_i \sigma_j | (c_{i, \sigma}^\dagger c_{j, \sigma} + \text{H.c.}) | n \rangle \frac{1}{E_0 - E_n} \langle n | (c_{i, \sigma'}^\dagger c_{j, \sigma'} + \text{H.c.}) | \sigma'_i \sigma'_j \rangle, \quad (1.8)$$

where $E_0 = 0$ is the ground state energy and $|n\rangle$ an excited state with energy E_n . Since hopping creates one empty and one doubly occupied site out of two singly occupied ones, $E_0 - E_n = U$. Moreover, the sum over the intermediate states acts as a complete sum, so that we can write also

$$-\frac{t^2}{U} \sum_{\sigma, \sigma'} \langle \sigma_i \sigma_j | (c_{i, \sigma}^\dagger c_{j, \sigma} c_{j, \sigma'}^\dagger c_{i, \sigma'} + c_{j, \sigma}^\dagger c_{i, \sigma} c_{i, \sigma'}^\dagger c_{j, \sigma'}) | \sigma'_i \sigma'_j \rangle. \quad (1.9)$$

We recall that the spin \mathbf{S}_i on site i is defined as:

$$\mathbf{S}_i = \frac{1}{2} \sum_{\sigma, \sigma'} c_{i, \sigma}^\dagger \boldsymbol{\tau}_{\sigma, \sigma'} c_{i, \sigma'}, \quad (1.10)$$

where $\boldsymbol{\tau} = (\tau_1, \tau_2, \tau_3)$, being τ_i 's the Pauli matrices. Using Eq. (1.10) we find that:

$$\begin{aligned} & -\frac{t^2}{U} \sum_{\sigma, \sigma'} (c_{i, \sigma}^\dagger c_{j, \sigma} c_{j, \sigma'}^\dagger c_{i, \sigma'} + c_{j, \sigma}^\dagger c_{i, \sigma} c_{i, \sigma'}^\dagger c_{j, \sigma'}) \\ &= \frac{t^2}{U} \sum_{\sigma, \sigma'} 2c_{i, \sigma}^\dagger c_{i, \sigma'} c_{j, \sigma'}^\dagger c_{j, \sigma} - (n_{i, \sigma} + n_{j, \sigma}) \delta_{\sigma, \sigma'} \\ &= \frac{4t^2}{U} \left[\mathbf{S}_i \mathbf{S}_j + \frac{1}{4} (n_i n_j - n_i - n_j) \right]. \end{aligned} \quad (1.11)$$

Since the last term is a constant over states where each site is singly occupied, we come to the conclusion that, in the large- U limit, the effective Hamiltonian is given by:

$$\mathcal{H}_{\text{Heis}} = J \sum_{\langle i, j \rangle} \mathbf{S}_i \mathbf{S}_j, \quad (1.12)$$

where we summed over all the couples of nearest-neighbour sites and defined $J = \frac{4t^2}{U}$. Therefore, the second order perturbation theory in the kinetic part of the Hubbard Hamiltonian created virtual hoppings of antiparallel neighbouring spins, which form an intermediate doubly occupied site. These virtual hoppings give origin to the antiferromagnetic

¹We assume for simplicity that hopping is restricted to nearest-neighbour sites. Extension to next-nearest neighbours is straightforward

Heisenberg Hamiltonian of Eq. (1.12), usually called *super-exchange*. This Hamiltonian describes the low-energy properties of the Hubbard model at half-filling for very large U/t and the corresponding ground state is smoothly connected to the insulating phase found for large U/t in the Hubbard model.

Chapter 2

The variational approach

In this chapter, we introduce the electronic wave functions used to approximate the exact ground state of correlated models. A particular emphasis will be given to backflow correlations, that represent the core of this thesis, where they are implemented in lattice models for the first time. Moreover, we are going to present the Monte Carlo methods [49] that allow us to evaluate, by means of a stochastic sampling, integrals over a multidimensional space. This is very useful for quantum many body problems, where in general the calculation of expectation values cannot be handled analytically, since the correlated wave function of the system cannot be factorized into one-particle states.

The core of all Monte Carlo methods is the Metropolis algorithm [50] which generates a Markov chain, i.e., a random walk in configuration space. The configurations sampled during the random walk are distributed according to a given stationary probability distribution, after a certain number of steps required to reach equilibrium.

In the first section, we introduce the variational Quantum Monte Carlo approach, consisting in the direct application of the Metropolis algorithm to sample the probability distribution given by the squared modulus of a given variational wave function.

In the second section, we present the correlated variational wave functions that are traditionally used to describe a magnetic ground state or a disordered spin-liquid one. We refer both to the Heisenberg and to the Hubbard models, introduced in the previous chapter to describe strongly-correlated electron systems. However, the wave function so far used for a spin-liquid ground state can be poorly accurate in two dimensions, especially in presence of frustration, and so we introduce in the third section new correlation effects, taking the clue from the backflow contribution, whose relevance has been emphasized for various interacting systems on the continuum.

In the fourth section, we compare backflow correlations with a more traditional approach to deal with the strong-coupling regime: the S -matrix expansion [28].

The fifth section is devoted to the stochastic reconfiguration algorithm [51], which allows us to minimize the variational energy in presence of a large number of parameters in the correlated wave function. In particular, we describe how to minimize the variational parameters appearing in backflow correlations. The sixth section goes on with Monte Carlo techniques, presenting the so-called Green's function Monte Carlo approach [15, 16], that allows us to systematically improve the variational energies. Indeed, this technique would allow us to extract the actual ground state from a given Hamiltonian \mathcal{H} , but the presence of the *sign problem* for fermions requires the use of the Fixed Node approximation [17] for a stable numerical calculation.

Finally, in the seventh section, we compare the variational energies of our wave functions, improved by means of backflow correlations, with the exact ones obtained using the Lanczos method [52], for small lattice sizes. Furthermore, we make a comparison of our variational and Fixed Node energies with the ones obtained using two different variational wave functions: the Lanczos step one [53] and the one that combines superconductivity and magnetism through the Pfaffian ansatz [29].

2.1 Variational Monte Carlo

The key ingredient of a Variational Monte Carlo (VMC) approach is the property of quantum mechanics, that the expectation value of an Hamiltonian \mathcal{H} over any trial wave function $|\Psi\rangle$, gives an upper bound to the exact ground-state energy E_0

$$E = \frac{\langle \Psi | \mathcal{H} | \Psi \rangle}{\langle \Psi | \Psi \rangle} \geq E_0. \quad (2.1)$$

This can be easily seen by inserting the complete set of eigenfunctions $|\Phi_i\rangle$ of \mathcal{H} with energies E_i

$$\frac{\langle \Psi | \mathcal{H} | \Psi \rangle}{\langle \Psi | \Psi \rangle} = \sum_i E_i \frac{|\langle \Phi_i | \Psi \rangle|^2}{\langle \Psi | \Psi \rangle} = E_0 + \sum_i (E_i - E_0) \frac{|\langle \Phi_i | \Psi \rangle|^2}{\langle \Psi | \Psi \rangle} \geq E_0. \quad (2.2)$$

In this way, if we have a set of different wave functions, we can choose the best approximation of the ground state simply by looking at the lowest expectation value of the energy. From this consideration, it is already clear that the key ingredient in VMC is constructing accurate trial wave functions, that give energies as close as possible to the actual ground-state one. Moreover, the variational approach represents a

straightforward technique that is able to deal with strongly-correlated systems, since a good guess on the ground-state wave function allows us to derive directly the properties of the corresponding phases.

The general form for a correlated wave function is usually given by:

$$|\Psi\rangle = \mathcal{P}(\{v_i\})|D(\{\Delta_i\})\rangle, \quad (2.3)$$

where $\mathcal{P}(\{v_i\})$ is the correlation factor (or *projector*) and $|D(\{\Delta_i\})\rangle$ is a mean-field Slater determinant. The determinantal part ensures the correct antisymmetry when particles are interchanged, while the projector \mathcal{P} inserts correlations into the wave function. Notice that $\{v_i, \Delta_i\}$ is a set of variational parameters which must be properly optimized, as discussed in a forthcoming section, to minimise the expectation value of the variational energy E . Moreover, we search variational wave functions that are size consistent. This means that the accuracy in the variational energy per site does not become worse as the system size is increased. The requirement of size consistency guarantees that the energy obtained on a finite lattice is already a good estimate of the thermodynamic limit.

The variational expectation values (2.1) cannot be calculated exactly, in an analytical way, for correlated wave functions, like the ones introduced in Eq. (2.3). Moreover, due to the rapid growth of the Hilbert space with the lattice size, exact diagonalization techniques can be applied only for very small clusters and, therefore, on larger sizes the most efficient way to compute observables, depending on a large number of variables, is to use the Monte Carlo approach. In order to show how a statistical approach can be used to calculate expectation values like (2.1), we introduce a complete set of states $|x\rangle$ on which correlated wave functions can be easily calculated:

$$\frac{\langle\Psi|\mathcal{H}|\Psi\rangle}{\langle\Psi|\Psi\rangle} = \frac{\sum_{x,x'} \Psi(x')\mathcal{H}_{x',x}\Psi(x)}{\sum_x \Psi^2(x)}, \quad (2.4)$$

where $\Psi(x) = \langle x|\Psi\rangle$, $\mathcal{H}_{x',x} = \langle x'|\mathcal{H}|x\rangle$ and we assumed real wave functions. We choose the set of states $|x\rangle$ to be the electronic configurations in real space. In particular, for the Hubbard model, since each site can be either singly occupied, by a spin up or down, empty or doubly occupied, the generic state reads, for instance, $|x\rangle = |\uparrow, \uparrow\downarrow, 0, \uparrow, \downarrow, 0, \downarrow, \uparrow\downarrow, \uparrow, \dots\rangle$.

Defining the *local energy* E_x as

$$E_x = \frac{\langle x|\mathcal{H}|\Psi\rangle}{\langle x|\Psi\rangle} = \sum_{x'} \frac{\Psi(x')}{\Psi(x)} \mathcal{H}_{x',x}, \quad (2.5)$$

Eq. (2.4) can be written as:

$$E = \frac{\langle \Psi | \mathcal{H} | \Psi \rangle}{\langle \Psi | \Psi \rangle} = \frac{\sum_x E_x \Psi^2(x)}{\sum_x \Psi^2(x)}. \quad (2.6)$$

Since the number of configurations $|x'\rangle$ connected to $|x\rangle$ is limited to a very small fraction of the Hilbert space, the local energy is generally computable in a very efficient way, even when the wave function $|\Psi\rangle$ contains strongly-correlated terms. Moreover, the local energy E_x depends crucially on the choice of the wave function $|\Psi\rangle$. In particular, if $|\Psi\rangle$ is an eigenstate of \mathcal{H} with eigenvalue E , the local energy does not depend on $|x\rangle$, namely $E_x = E$ with no fluctuations: this is the so-called zero variance property.

In general, the evaluation of the local energy can be done by generating a sample X of \mathcal{N} configurations, according to the probability distribution

$$\bar{P}_x = \frac{\Psi^2(x)}{\sum_{x'} \Psi^2(x')}, \quad (2.7)$$

and then averaging the values of the local energy over these configurations

$$E \simeq \frac{1}{\mathcal{N}} \sum_{x \in X} E_x. \quad (2.8)$$

The simplest method to generate a set of configurations according to the probability distribution $\bar{P}(x)$ is the Metropolis algorithm [50], which tells us that starting from a configuration $|x\rangle$, a new configuration $|x'\rangle$ is accepted if a random number η , between 0 and 1, satisfies the condition

$$\eta < \frac{\bar{P}_{x'}}{\bar{P}_x} = \left[\frac{\Psi(x')}{\Psi(x)} \right]^2, \quad (2.9)$$

otherwise the configuration is kept equal to the old one, i.e., $|x'\rangle = |x\rangle$.

The first step for applying the Metropolis algorithm in VMC is to choose the initial configuration $|x_0\rangle$, corresponding to a set of coordinates $\{x_i\}_0$ for the N particles on the lattice, either randomly or taking them from a previous Monte Carlo run. Then, a new trial configuration $|x^T\rangle$ is chosen by moving one of the particles from its position to a new one. If this configuration is accepted, with probability

$$\mathcal{P}_{x_0 \rightarrow x^T} = \min[1, \mathcal{R}] \quad \text{with} \quad \mathcal{R} = \left| \frac{\Psi(x^T)}{\Psi(x_0)} \right|^2, \quad (2.10)$$

it becomes the new set of coordinates $\{x_i\}_1$. This is done in practice by extracting a positive random number $0 < \eta \leq 1$; if $\mathcal{R} \geq \eta$ then $|x_1\rangle = |x^T\rangle$, otherwise the proposed move is rejected and $|x_1\rangle = |x_0\rangle$.

This procedure is repeated in order to generate a Markov chain, that is a random walk in the configuration space. Moreover, the definition (2.10) guarantees that every configuration $|x_n\rangle$ at step n depends only on the configuration $|x_{n-1}\rangle$ at step $n - 1$.

After a certain number of steps M , known as thermalization time, the configurations $|x_{n>M}\rangle$ are independent from the initial condition $|x_0\rangle$ and are distributed according to the probability:

$$\bar{P}_x = \frac{|\Psi(x)|^2}{\sum_{x'} |\Psi(x')|^2}. \quad (2.11)$$

The existence of a stationary distribution \bar{P}_x is guaranteed by a sufficient (but not necessary) condition, that is the *detailed balance* condition:

$$\mathcal{P}_{x \rightarrow x'} \bar{P}_x = \mathcal{P}_{x' \rightarrow x} \bar{P}_{x'}. \quad (2.12)$$

This relationship indicates that the number of processes undergoing a transition $|x\rangle \rightarrow |x'\rangle$ has to be exactly compensated, to maintain a stable stationary condition, by the same amount of reverse processes $|x'\rangle \rightarrow |x\rangle$. Moreover, the convergence to the same \bar{P}_x from any initial condition $|x_0\rangle$ is guaranteed if the Markov chain is *ergodic*, i.e. any configuration can be reached, in a sufficiently large number of Markov iterations, starting from any initial configuration $|x_0\rangle$.

Notice that this algorithm does not require to know the normalization of the wave function, since it only deals with ratios over different configurations. This is a great advantage of Monte Carlo methods, since in general the normalization is impossible to compute for large systems.

Finally, the expectation value $\langle O \rangle$ of any operator O (like energy, as mentioned above) reduces to average over the values assumed by O along the \mathcal{N} steps of the Markov chain:

$$\bar{O} = \frac{1}{\mathcal{N}} \sum_{x \in X}^{\mathcal{N}} O(x), \quad (2.13)$$

where $O(x)$ is the observable O , calculated for the configuration $|x\rangle$. Indeed, the central limit theorem ensures that

$$\lim_{\mathcal{N} \rightarrow \infty} \bar{O} = \langle O \rangle, \quad (2.14)$$

where $\langle O \rangle$ is the true expectation value of O calculated from the probability \bar{P}_x . The statistical error related to the fact that we are sampling a finite set of configurations can be deduced from the variance

$$\sigma^2(\bar{O}) = \langle (\bar{O} - \langle O \rangle)^2 \rangle. \quad (2.15)$$

One can show that the statistical error scales as the square root of the inverse length \mathcal{N} of the Markov chain, namely

$$\sigma^2(\bar{O}) \simeq \frac{\tau}{\mathcal{N}} \sigma^2(O), \quad (2.16)$$

where $\sigma^2(O) = \langle (O^2 - \langle O \rangle^2) \rangle$ and τ is the autocorrelation time, i.e. the number of steps of the Markov chain which separate two statistically independent configurations. Therefore, for large enough samplings, the average quantities calculated with the Metropolis algorithm give reliable estimates of the true expectation values of the system.

In order to calculate expectation values among uncorrelated samplings, the bin technique is usually employed. This simply corresponds to average first among M_{bin} configurations, according to (2.13):

$$\bar{O}_n^{bin} = \frac{1}{M_{bin}} \sum_{i=nM_{bin}+1}^{(n+1)M_{bin}} O(x_i). \quad (2.17)$$

In this way the quantities \bar{O}_n^{bin} are less correlated than the original $O(x_i)$. Then the calculation of the expectation value follows:

$$\bar{O} = \frac{1}{N_{bin}} \sum_{n=1}^{N_{bin}} \bar{O}_n^{bin}, \quad (2.18)$$

where $N_{bin} = \mathcal{N}/M_{bin}$. The bin technique does not affect the average value, whereas, if M_{bin} is large enough, we can safely assume that $\tau \sim 1$ and the variance can be evaluated in the standard way as

$$\sigma^2(\bar{O}) = \frac{1}{N_{bin}(N_{bin} - 1)} \sum_{n=1}^{N_{bin}} (\bar{O}_n^{bin} - \langle O \rangle)^2. \quad (2.19)$$

2.2 Variational wave functions

As already mentioned in the previous section, the choice of an accurate wave function for the actual ground state of a correlated electronic system is the key ingredient in a Variational Monte Carlo approach. Traditionally, the general form for a correlated wave function is usually given by Eq. (2.3), with a set $\{v_i, \Delta_i\}$ of variational parameters which must be properly optimized, as discussed in a forthcoming section, to minimise the expectation value of the variational energy. In the following, we will introduce explicitly the wave functions that attempt to reproduce the ground state of both the Heisenberg and the Hubbard model, that were introduced in the previous chapter as the basic models to describe strongly-correlated electron systems.

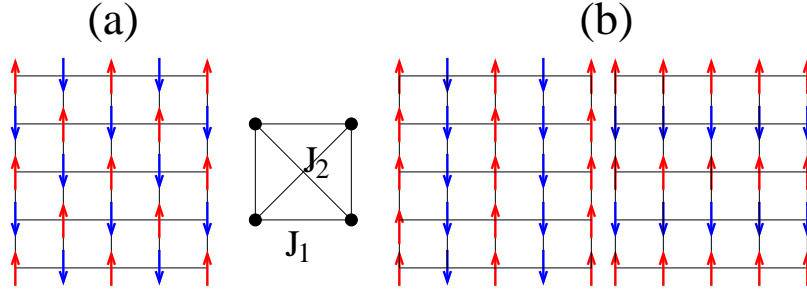


Figure 2.1: Two kinds of magnetic phases on the square lattice with nearest (J_1) and next-nearest (J_2) neighbour interaction. The first one (a) has pitch vector $\mathbf{Q} = (\pi, \pi)$, while the second one has two equivalent pitch vectors $\mathbf{Q} = (\pi, 0)$ and $\mathbf{Q} = (0, \pi)$.

2.2.1 The variational approach in the Heisenberg model

The ground state of a spin model, described by a frustrated Heisenberg model, can be either magnetically ordered or in a disordered spin-liquid state, if frustration is strong enough to destroy long-range order.

The determinant part of a wave function describing a magnetically ordered phase can be chosen as the ground state of a mean-field magnetic Hamiltonian¹:

$$\mathcal{H}_{\text{AF}} = \Delta_{\text{AF}} \sum_j \exp[i\mathbf{Q}\mathbf{R}_j](\mathbf{S}_j \cdot \mathbf{n}_j), \quad (2.20)$$

where \mathbf{R}_j are the position of the lattice sites, $\mathbf{S}_j \cdot \mathbf{n}_j$ is the component of the spin-operator $\mathbf{S}_j = (S_j^x, S_j^y, S_j^z)$ along the direction of the classical order \mathbf{n}_j and \mathbf{Q} is the pitch vector, depending on the nature of the magnetic order. For example, on a square lattice with nearest (J_1) and next-nearest (J_2) neighbour interactions, two different magnetic phases can be stabilized [54]. The first phase shown in Fig. (2.1), stable for small J_2/J_1 , has pitch vector $\mathbf{Q} = (\pi, \pi)$, while the second phase, stable for higher values of J_2/J_1 , has pitch vectors $\mathbf{Q} = (\pi, 0)$ and $\mathbf{Q} = (0, \pi)$. On top of the determinant, we should apply a correlation factor \mathcal{P} that, in this case, takes the form of a long-range spin-Jastrow factor:

$$J_s = \exp \left[\frac{1}{2} \sum_{i,j} v_{ij} S_i^z S_j^z \right], \quad (2.21)$$

where S_j^z is the z -component of the spin associated to the particle on site j . This particular term, that couples the z -component of the electron spin on different lattice sites, induces spin fluctuations orthogonal

¹We are assuming that the electron spins are ordered in a collinear way.

to the ordering direction. In this way, it allows us to reproduce the correct spin-spin correlations at large distance [55]. Moreover, the exponential form guarantees the size consistency of the wave function.

On the other hand, in order to describe a spin-liquid ground-state in the Heisenberg model, we can consider the ground state $|\text{BCS}\rangle$ of a BCS Hamiltonian,

$$\mathcal{H}_{\text{BCS}} = \sum_{i,j,\sigma} t_{ij} c_{i,\sigma}^\dagger c_{j,\sigma} - \mu \sum_{i,\sigma} c_{i,\sigma}^\dagger c_{i,\sigma} + \sum_{i,j} \Delta_{ij} \left(c_{i,\uparrow}^\dagger c_{j,\downarrow}^\dagger + c_{j,\uparrow}^\dagger c_{i,\downarrow}^\dagger \right) + \text{H.c.}, \quad (2.22)$$

and then we can apply to it the so-called Gutzwiller projector:

$$\mathcal{P}_G = \prod_i (1 - n_{i,\uparrow} n_{i,\downarrow}), \quad (2.23)$$

that removes the double occupancies, not allowed for the Heisenberg model ($n_{i,\sigma}$ is just the number operator for an electron of spin σ on site i). Due to the presence of the Gutzwiller projector, the singlet pairs created by the BCS Hamiltonian do not overlap in real space and this wave function can be described by a superposition of valence bond states. Then, the full wave function is a good candidate to describe a Resonant Valence Bond state [40, 56]: $|\text{RVB}\rangle = \mathcal{P}_G |\text{BCS}\rangle$. In fact, in Ref. [18] a true spin liquid is stabilized in the frustrated Heisenberg model on the square lattice for $0.4 \lesssim J_2/J_1 \lesssim 0.6$, using this kind of wave function.

2.2.2 The variational approach in the Hubbard model

It is in general more complicated to choose an accurate wave function for the ground state of the Hubbard model, rather than for the Heisenberg model, because now the possibility for the electrons to hop from one site to the other adds new scales of energy to the spin interaction J . In particular, we have to take into account the hopping integral t , that tends to delocalize the electrons, and the on-site electron-electron repulsion U . As a consequence, a good wave function should describe a metal-insulator transition (MIT) at some finite value of the ratio U/t , in presence of frustration.

If the insulating state is magnetically ordered, an accurate wave function for the Hubbard model can be chosen in a manner similar to what already done for the Heisenberg model. The determinantal part of the wave function is the ground state $|\text{AF}\rangle$ of a mean-field Hamiltonian

$$\mathcal{H}_{\text{AF}} = \sum_{i,j,\sigma} t_{ij} c_{i,\sigma}^\dagger c_{j,\sigma} + \Delta_{\text{AF}} \sum_j \exp[i\mathbf{Q}\mathbf{R}_j] (\mathbf{S}_j \cdot \mathbf{n}_j), \quad (2.24)$$

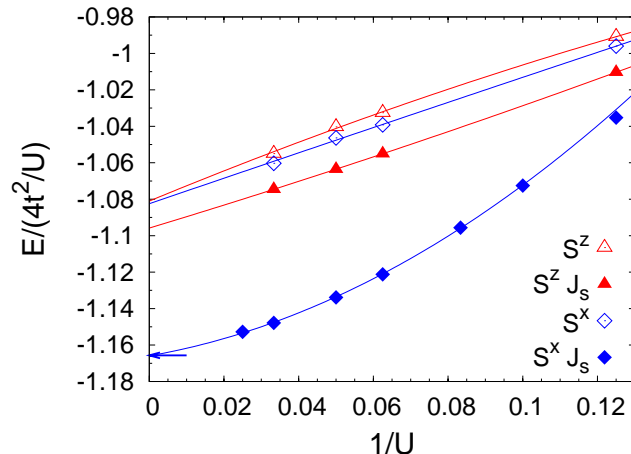


Figure 2.2: Variational energies in the Hubbard model on a 98-site square lattice (in unit of $J = 4t^2/U$), with only nearest neighbour coupling, at increasing U , for different variational wave functions. Empty triangles and empty rhombi correspond to energies computed using a simple mean-field $|\text{AF}\rangle$ wave function, with magnetic ordering along the z or the x direction, respectively. Full triangles correspond to energies computed adding a Jastrow factor parallel to the direction of the magnetic ordering z . Full rhombi correspond to energies computed using a Jastrow term orthogonal to the direction of the magnetic ordering x . The arrow indicates the variational energy obtained in the Heisenberg model using a spin-Jastrow factor (see Eq. (2.21) over the ground state of the magnetic Hamiltonian (2.20).

that now includes a kinetic term in addition to the magnetic one. The correlation factor acting on $|\text{AF}\rangle$ is the same spin-Jastrow term of Eq. (2.21), that ensures the correct spin-spin correlations at large distance. In Fig. (2.2), we show the variational energies, for increasing U , for the Hubbard model on a square lattice with only nearest neighbour hopping, using four different kinds of magnetic wave functions. Empty symbols correspond to energies computed using a simple mean-field $|\text{AF}\rangle$ wave function, with magnetic ordering along the x or the z direction. Only a small energy gain can be obtained by inserting a spin-Jastrow term (see Eq. 2.21), if the magnetic ordering, induced by the mean-field Hamiltonian, is in the z direction, parallel to the fluctuations induced by the Jastrow factor. On the contrary, if the magnetic ordering induced by the mean-field Hamiltonian is in the x direction, the accuracy in ground state energies is highly improved and, moreover, the variational energies in the Hubbard model extrapolate to the variational energy in the Heisenberg model, as U is increased.

At variance of the magnetically ordered phases, it is much more difficult to describe accurately a spin-liquid state in the Hubbard model, as we are going to present in the forthcoming sections. Since the variational state must contain charge fluctuations, the simplest generalization of the $\mathcal{P}_G|\text{BCS}\rangle$ wave function, introduced for the Heisenberg model, is to release the constraint of no-double occupancies, defining a soft Gutzwiller projector \mathcal{G} [57]:

$$\mathcal{G} = \exp\left[-g \sum_i n_{i,\uparrow} n_{i,\downarrow}\right]. \quad (2.25)$$

This correlation factor takes into account that the expectation value of the energy in the Hubbard Hamiltonian contains a repulsive term for two electrons of opposite spins, located on the same lattice site. It is important to stress that this energy loss cannot be avoided within the simple $|\text{BCS}\rangle$ wave function; in fact it is not possible to suppress charge fluctuations, reducing the number of doubly occupied sites, within the BCS Hamiltonian and the Gutzwiller term is unavoidable. Numerical studies, done by using Quantum Monte Carlo [58, 59], and exact analytic treatments in one dimension [60] clarified that the Gutzwiller correlation factor is not sufficient to create an insulator in any finite dimension. In particular, for any finite U , the g parameter is finite, leading to a certain number of double occupancies, and the system turns out to be metallic. This is due to the fact that, once a pair of empty-doubly occupied sites is formed, these objects are free to move without paying any further energy cost, and, therefore, they can participate to the conduction events (In the forthcoming we will indicate empty sites as *holons* and doubly occupied sites as *doublons*). More specifically, at half-filling, holons are positively charged objects, while the doublons are negatively charged. When an electric field is applied to the system, they are free to move in opposite directions, and the system shows a metallic behaviour.

In order to describe a metal-insulator transition at a finite value of U , early variational wave functions [61, 62], were constructed, introducing short-range correlations among empty and doubly occupied sites. However, these attempts failed to describe properly an insulating state and the description of a metal-insulator transition within a spin-liquid wave function was obtained only very recently by Capello *et al.* [20], inserting a long-range charge-Jastrow in the wave function:

$$J = \exp\left[\frac{1}{2} \sum_{i,j} v(r_{ij}) n_i n_j\right], \quad (2.26)$$

where $v(r_{ij}) = v(|r_i - r_j|)$ are variational parameters, which for isotropic

systems depend only on the relative distance among the particles, and n_i is the particle density at position r_i . The wave function describing a spin liquid in the Hubbard model reads $|\Psi_{\text{SL}}\rangle = J|\text{BCS}\rangle$, where $|\text{BCS}\rangle$ is the ground state of the Hamiltonian (2.22). It can be easily proved that the long-range coupling $n_i n_j$ in the charge-Jastrow factor includes holon-holon and doublon-doublon repulsion as well as holon-doublon attraction, if $v(r_{ij}) < 0$. Indeed, introducing the doublon $D_i = n_{i,\uparrow} n_{i,\downarrow}$ and the holon $H_i = (1 - n_{i,\uparrow})(1 - n_{i,\downarrow})$ operators, the Jastrow correlation $n_i n_j$ can be written as:

$$n_i n_j = D_i D_j + H_i H_j - H_i D_j - D_i H_j + n_i + n_j - 1 . \quad (2.27)$$

The Jastrow factor has a long story in physics, in particular the most interesting analytical and numerical results concerning the properties of the Jastrow wave function come from its wide applications in Helium physics. In this field it is worth mentioning the very early approach of McMillan [63], who used a parametrization of the Jastrow term coming from the solution of the corresponding two-body problem. The form of the Jastrow factor has been subsequently finetuned [64, 65, 66, 67] in order to reproduce accurately the properties of the ^4He liquid state. It turned out that, even if the ground-state energy is well approximated by using a short-range correlation term, the addition of a structure in the parameters $v(r_{ij})$, at large distances, is fundamental to reproduce correctly the pair distribution function and the structure factor of the liquid.

However, we observed that the wave function $|\Psi_{\text{SL}}\rangle = J|\text{BCS}\rangle$ is poorly accurate in two dimensions, for strongly correlated lattice models, especially in presence of frustration. For example, in Fig. (2.3) we show the variational energy for the Hubbard model on the square lattice, using $|\Psi_{\text{SL}}\rangle$ as the trial wave function. We consider both the unfrustrated case with only nearest-neighbour hopping t and the frustrated case with a further next-nearest-neighbour coupling t' . Especially in presence of frustration, the variational energies loose accuracy for increasing interaction U and do not match the variational energy of the corresponding Heisenberg models, obtained with a $\mathcal{P}_G|\text{BCS}\rangle$ wave function. In order to improve the accuracy of the $|\Psi_{\text{SL}}\rangle$ wave function in the Hubbard model, we introduce new correlation effects, that go beyond the Jastrow factor. We take the clue from the backflow contribution, whose relevance has been emphasized for various interacting systems on the continuum.

2.3 Backflow wave function

We mentioned in the previous section that the wave function describing a spin liquid state, $|\Psi_{\text{SL}}\rangle$, can be poorly accurate in a 2D frustrated system. This is particularly evident in the strong-coupling regime. In fact, if we want to satisfy the single-occupancy constraint, which characterizes the highly repulsive limit of the Hubbard model, we need to apply the full Gutzwiller projector on top of the $|\Psi_{\text{SL}}\rangle$ wave function. In this way, charges are frozen in the lattice sites and there is no way to generate virtual hopping processes, by means of the kinetic term. The absence of the virtual hopping processes fails to reproduce the super-exchange physics, that is crucial in the strong-coupling regime.

In this respect, we look for an improvement of the wave function that mimics the effect of the virtual hopping, leading us to the super-exchange mechanism. Good candidates for this are the so-called backflow correlations, that were introduced a long time ago by Feynman and Cohen [21] to obtain a quantitative description of the roton excitation in liquid Helium. The term backflow came out because it creates a return flow of current, opposite to the one computed with the original wave function. Conservation of the particle current and the variational principle lead then to the optimal backflow.

The backflow term has been implemented within quantum Monte

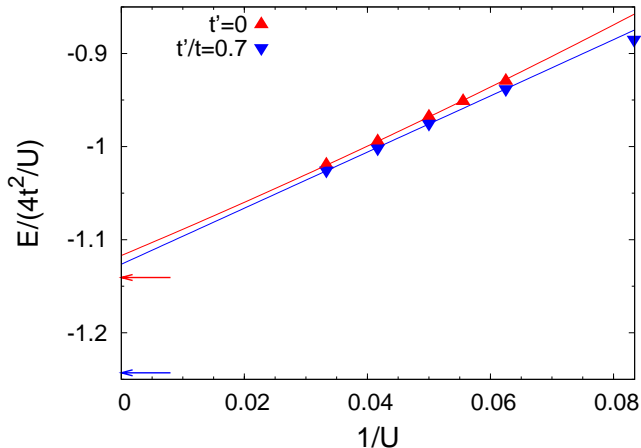


Figure 2.3: Variational energies in the Hubbard model (in unit of $J = 4t^2/U$) using $|\Psi_{\text{SL}}\rangle$ as a trial wave function, for a 98-site lattice. We consider both the unfrustrated and the frustrated case with $t'/t = 0.7$. Arrows indicate the variational results obtained by applying the full Gutzwiller projection to the $|\text{BCS}\rangle$ state for the corresponding Heisenberg models.

Carlo calculations to study bulk liquid ^3He [22, 23] and then applied to weakly correlated electron systems: Backflow correlations turned out to be crucial in improving the description of the electron jellium model both in two and three dimensions, in particular for correlation energies and pair distribution functions. Furthermore, backflow correlations were found to be important in determining the Fermi-liquid parameters [24, 25]. More recently, backflow has been applied also to metallic hydrogen [26] and to small atoms and molecules [27], where significant improvements in the total energy have been obtained. In all these contexts, the backflow term corresponds to consider fictitious coordinates of the particles (Helium atoms or electrons) \mathbf{r}_α^b , which depend on the positions of the other ones,

$$\mathbf{r}_\alpha^b = \mathbf{r}_\alpha + \sum_{\beta} \eta_{\alpha,\beta}[x](\mathbf{r}_\beta - \mathbf{r}_\alpha), \quad (2.28)$$

where \mathbf{r}_α are the actual particle positions and $\eta_{\alpha,\beta}[x]$ are variational parameters depending in principle on all the coordinates $\{\mathbf{r}_\alpha\}$, namely, on the many-body configuration $|x\rangle$.

The variational wave functions introduced in the previous section (spin liquid and magnetic ones) are constructed by means of single particle orbitals, defined as the eigenstates of an appropriate mean-field Hamiltonian. Now, these orbitals should be calculated in the new positions, i.e., $\phi(\mathbf{r}_\alpha^b)$. However, since we work on a lattice, electron coordinates cannot vary with continuity so that Eq.(2.28) is not strictly applicable in practice. To overcome this problem, we introduced an alternative definition of backflow correlations by considering a linear expansion of each single-particle orbital:

$$\phi_k(\mathbf{r}_\alpha^b) \sim \phi_k^b(\mathbf{r}_\alpha) \equiv \phi_k(\mathbf{r}_\alpha) + \sum_{\beta} c_{\alpha,\beta}[x]\phi_k(\mathbf{r}_\beta), \quad (2.29)$$

where $c_{\alpha,\beta}[x]$ are suitable coefficients.

The next question is how to determine the coefficients $c_{\alpha,\beta}[x]$. In the Hubbard model, we can consider the $U \gg t$ limit, where a recombination of neighbouring charge fluctuations (i.e., empty and doubly-occupied sites) is clearly favoured and can be obtained by the following ansatz for the backflow term:

$$\phi_k^b(\mathbf{r}_{i,\sigma}) \equiv \eta_0 \phi_k(\mathbf{r}_{i,\sigma}) + \eta_1 \sum_j t_{ij} D_i H_j \phi_k(\mathbf{r}_{j,\sigma}), \quad (2.30)$$

where we used the notation that $\phi_k(\mathbf{r}_{i,\sigma}) = \langle 0|c_{i,\sigma}|\phi_k\rangle$ are the eigenstates of the mean-field Hamiltonian, $D_i = n_{i,\uparrow}n_{i,\downarrow}$, and $H_i = h_{i,\uparrow}h_{i,\downarrow}$,

with $h_{i,\sigma} = (1 - n_{i,\sigma})$, so that D_i and H_i are non zero only if the site i is doubly occupied or empty, respectively; finally η_0 and η_1 are variational parameters (we can assume that $\eta_0 = 1$ if $D_i H_j = 0$).

As a consequence, the determinant part of the wave function already includes correlation effects due to the presence of the many-body operator $D_i H_j$. This allows us to modify the nodal surface² of the electronic wave function, a very important and new ingredient of the backflow term, considering that the so important and celebrated Jastrow factor can modify just the amplitude of the wave function. In the following sections, we will see that the ability of changing the nodes is crucial also to improve the accuracy within Green's function Monte Carlo [15, 16].

Now it is worth mentioning that the correlation among holons and doublons, introduced in Eq. (2.30), is quite similar to the one present in a kind of Jastrow introduced by Shiba [62]:

$$J_{\text{Shiba}} = \exp \left(v \left[\sum_i D_i \prod_{j \text{ n.n. } i} (1 - H_j) + \sum_i H_i \prod_{j \text{ n.n. } i} (1 - D_j) \right] \right), \quad (2.31)$$

in which the amplitude of the electronic wave function is suppressed when a doubly occupied site has no neighbouring empty sites. However, since in a Jastrow factor correlation effects are not included in the determinant part of the wave function, it turns out to be much less accurate than backflow correlations, as detailed later on. Furthermore, the simultaneous presence of a Shiba Jastrow and of a backflow term in the wave functions does not bring any improvement in the variational energy.

A further generalization of the new ‘‘orbitals’’ can be made by taking all the possible virtual hoppings of the electrons:

$$\begin{aligned} \phi_k^b(\mathbf{r}_{i,\sigma}) &= \eta_0 \phi_k(\mathbf{r}_{i,\sigma}) + \eta_1 \sum_j t_{ij} D_i H_j \phi_k(\mathbf{r}_{j,\sigma}) \\ &+ \eta_2 \sum_j t_{ij} n_{i,\sigma} h_{i,-\sigma} n_{j,-\sigma} h_{j,\sigma} \phi_k(\mathbf{r}_{j,\sigma}) \\ &+ \eta_3 \sum_j t_{ij} (D_i n_{j,-\sigma} h_{j,\sigma} + n_{i,\sigma} h_{i,-\sigma} H_j) \phi_k(\mathbf{r}_{j,\sigma}), \quad (2.32) \end{aligned}$$

where η_0 , η_1 , η_2 and η_3 are variational parameters. In particular, the term multiplied by η_2 takes into account hoppings that create a new holon-doublon pair, while the term multiplied by η_3 describes hoppings that do not change the total number of doubly occupied and empty

²The nodal surface is the region where the electronic wave function changes its sign.

sites. While Eq. (2.30) preserves the spin $SU(2)$ symmetry, the generalized equation (2.32) may break it. However, the optimized wave function always has a very small value of the total spin square, i.e. $\langle S^2 \rangle \sim 0.001$ for 50 sites. Moreover, we have noticed that, for example, in the region relevant for a spin liquid on a square lattice, Eq. (2.30) is already able to stabilize a disordered phase, while the additional parameters η_2 and η_3 give only a small improvement in the ground-state energy.

As discussed in the next chapter, backflow correlations are less crucial in the magnetically ordered phases, with respect to the phase described by the BCS wave function, where backflow has been introduced to mimic the effect of the virtual hopping. In fact, a large value for the parameter Δ_{AF} in the antiferromagnetic mean-field Hamiltonian is already able by itself to satisfy the single-occupancy (strong-coupling) constraint, forcing the electrons to lay in a magnetically ordered pattern. Then, the kinetic term in the mean-field Hamiltonian generates the virtual hopping processes, leading to the super-exchange mechanism.

2.4 Comparison with the S -matrix strong-coupling expansion

In the following, we present briefly how backflow correlations compare with a more traditional approach to deal with the strong-coupling regime, based on a unitary transformation [28] which eliminates the terms in the Hubbard model coupling sectors with different number of doubly occupied sites:

$$\mathcal{H}' = e^{iS} \mathcal{H} e^{-iS} = \mathcal{H} + \frac{[iS, \mathcal{H}]}{1!} + \frac{[iS, [iS, \mathcal{H}]]}{2!} + \dots, \quad (2.33)$$

where \mathcal{H} is the Hamiltonian of the Hubbard model and \mathcal{H}' is the transformed Hamiltonian. In particular, by truncating the expansion (2.33) at first order, the transformed Hamiltonian \mathcal{H}' can be mapped into the Heisenberg one.

However, since we are interested in computing expectation values of operators, we can alternatively say that

$$\frac{\langle \Psi_{\mathcal{H}'} | \mathcal{H}' | \Psi_{\mathcal{H}'} \rangle}{\langle \Psi_{\mathcal{H}'} | \Psi_{\mathcal{H}'} \rangle} = \frac{\langle \Psi_{\mathcal{H}'} | e^{iS} \mathcal{H} e^{-iS} | \Psi_{\mathcal{H}'} \rangle}{\langle \Psi_{\mathcal{H}'} | \Psi_{\mathcal{H}'} \rangle} = \frac{\langle \Psi_{\mathcal{H}} | \mathcal{H} | \Psi_{\mathcal{H}} \rangle}{\langle \Psi_{\mathcal{H}} | \Psi_{\mathcal{H}} \rangle}, \quad (2.34)$$

where $|\Psi_{\mathcal{H}'}\rangle$ is the ground state of \mathcal{H}' and we define the ground state of the Hubbard Hamiltonian $|\Psi_{\mathcal{H}}\rangle$ as:

$$|\Psi_{\mathcal{H}}\rangle = \exp(-iS) |\Psi_{\mathcal{H}'}\rangle. \quad (2.35)$$

Wave function	Energy
$J \text{BCS}\rangle$	-0.1317(1)
$J \text{BCS+Backflow}\rangle$	-0.1519(1)
$(1 - iS) \text{RVB}\rangle$	-0.1432(1)
Exact (Lanczos)	-0.1577

Table 2.1: Variational energies for the Hubbard model on a 18-site square lattice at $U/t = 30$ and $t' = 0$, using three different kinds of variational wave functions. Exact energy is given for comparison.

If \mathcal{H}' coincides with the Heisenberg Hamiltonian, $|\Psi_{\mathcal{H}'}\rangle$ is a fully-projected state (with no doubly-occupied sites), that describes accurately a certain phase in the Heisenberg model. For instance, $|\Psi_{\mathcal{H}'}\rangle = |\text{RVB}\rangle$ in the spin liquid phase stabilized for $J_2/J_1 \sim 0.5$.

Though it is possible to define a recursive scheme for determining $|\Psi_{\mathcal{H}}\rangle$ to any order of t/U , this kind of approach is rather difficult to implement for large clusters, since, in contrast to the Jastrow term, S is non diagonal in the natural basis $|x\rangle$ where the electrons with spins quantized along z occupy the lattice sites. However, at high values of U/t , we can approximate, at linear order,

$$\Psi_{\mathcal{H}} \sim (1 - iS)|\text{RVB}\rangle, \quad (2.36)$$

where:

$$S = \frac{i}{U} \sum_{i,j} t_{ij} n_{i,-\sigma} c_{i,\sigma}^\dagger c_{j,\sigma} (1 - n_{j,-\sigma}) + \text{h.c.} . \quad (2.37)$$

Eq. (2.36) is not size-consistent and in fact, as size is increased, the variational energy obtained using $(1 - iS)|\text{RVB}\rangle$ as a variational wave function, loses accuracy. Indeed, already on a small 18-site square lattice, the variational energy in the Hubbard model with parameters $U/t = 30$ and $t' = 0$ is lower for a $J|\text{BCS}\rangle$ trial wave function, with backflow correlations, than for the $(1 - iS)|\text{RVB}\rangle$ wave function (see Table 2.1). By increasing the system size to a 98-site lattice, the ground state energies computed with the $(1 - iS)|\text{RVB}\rangle$ wave function become even worse than the ones obtained within the simple $|\Psi_{\text{SL}}\rangle = J|\text{BCS}\rangle$ wave function, as shown in Table (2.2), up to $U/t = 80$.

2.5 The minimization algorithm

The variational wave functions, introduced in the previous sections, depend, in general, on a set of variational parameters $\alpha = \{\alpha_k\}$, appearing in both the correlation factor and the Slater determinant. These

Wave function	Energy ($U/t = 50$)	Energy ($U/t = 60$)	Energy ($U/t = 80$)
$J \text{BCS}\rangle$	-0.0839(1)	-0.0712(2)	-0.0542(2)
$J \text{BCS}+\text{Backflow}\rangle$	-0.09005(4)	-0.07515(2)	-0.05654(2)
$(1 - iS) \text{RVB}\rangle$	-0.0774(2)	-0.0676(2)	-0.0535(2)

Table 2.2: Variational energies at increasing U/t in the Hubbard model on a 98-site square lattice with only nearest-neighbour coupling, for three different trial wave functions.

parameters have to be optimized in order to minimise the expectation value of the variational energy:

$$E(\alpha) = \frac{\langle \Psi(\alpha) | \mathcal{H} | \Psi(\alpha) \rangle}{\langle \Psi(\alpha) | \Psi(\alpha) \rangle} = \frac{\sum_x |\langle x | \Psi(\alpha) \rangle|^2 E_x}{\sum_x |\langle x | \Psi(\alpha) \rangle|^2} \geq E_0, \quad (2.38)$$

where E_0 is the actual ground-state energy and E_x is the so-called *local energy*, defined as:

$$E_x = \frac{\langle x | \mathcal{H} | \Psi(\alpha) \rangle}{\langle x | \Psi(\alpha) \rangle}. \quad (2.39)$$

Eq. (2.38) shows that the expectation value of the energy corresponds to the mean value of the local energy E_x , calculated among all the possible configurations $|x\rangle$, each weighted according to the square modulus of the normalized wave function. As shown in a previous section, this can be done stochastically, summing over a Markov chain in configuration space.

In the following, we present the so-called stochastic reconfiguration algorithm (SR) [51], that allows us to vary the parameters $\{\alpha_k\}$, in order to minimise the variational energy. Let us consider a starting trial wave function $|\Psi(\alpha^0)\rangle$, where $\alpha^0 = \{\alpha_k^0\}$ is the set of p initial parameters (assuming that $k = 1, \dots, p$). In linear approximation, the new wave function $|\Psi(\alpha')\rangle$, obtained after a small change of the parameters $\delta\alpha = \alpha' - \alpha^0$, can be written as:

$$|\Psi(\alpha')\rangle \simeq |\Psi(\alpha^0)\rangle + \sum_{k=1}^p \delta\alpha_k \frac{\partial |\Psi(\alpha^0)\rangle}{\partial \alpha_k} = \left[1 + \sum_{k=1}^p \delta\alpha_k O_k \right] |\Psi(\alpha^0)\rangle, \quad (2.40)$$

where the operators O_k are defined, for any configuration $|x\rangle$, as the logarithmic derivative of the wave function, with respect to the parameters α_k :

$$O_k(x) = \frac{\partial \ln \langle x | \Psi(\alpha) \rangle}{\partial \alpha_k}. \quad (2.41)$$

Computing the logarithmic derivative can be quite complicated and we shall treat this problem later in the section. Defining $O_0 = 1$ and $\delta\alpha_0 = 1$, Eq. (2.40) can be written in a more compact way:

$$|\Psi(\alpha')\rangle = \sum_{k=0}^p \delta\alpha_k O_k |\Psi(\alpha^0)\rangle. \quad (2.42)$$

However, as a result of the iterative minimization scheme we are going to present, $\delta\alpha_0 \neq 1$, and in this case the variation of the parameters will be obviously scaled

$$\delta\alpha_k \rightarrow \frac{\delta\alpha_k}{\delta\alpha_0}. \quad (2.43)$$

Now, the key point is how to determine the new set of parameters $\{\alpha'_k\}$ so that, applying repeatedly Eq. (2.40), $|\Psi(\alpha')\rangle$ approaches the ground state. We take the clue from projection methods, that filter out the exact ground-state wave function, by iteratively applying the Hamiltonian operator to the trial ground state. In particular, we can apply the *power method* to the starting wave function:

$$|\Psi'(\alpha^0)\rangle = \mathcal{P}_{\text{SR}}(\Lambda - \mathcal{H})|\Psi(\alpha^0)\rangle, \quad (2.44)$$

where Λ is a large positive constant, that ensures convergence to the ground state and \mathcal{P}_{SR} is a projection operator over the $(p+1)$ -dimensional subspace spanned by the basis $\{O_k|\Psi(\alpha^0)\rangle\}$, on which $|\Psi(\alpha')\rangle$ has been expanded. Given this condition, we can equate Eq. (2.40) and Eq. (2.44):

$$\sum_{k=0}^p \delta\alpha_k O_k |\Psi(\alpha^0)\rangle \equiv \mathcal{P}_{\text{SR}}(\Lambda - \mathcal{H})|\Psi(\alpha^0)\rangle. \quad (2.45)$$

This procedure ensures that $|\Psi(\alpha')\rangle$ has energy lower than $|\Psi(\alpha_0)\rangle$. Then, projecting each side of Eq. (2.45) along the k' -th component of the basis $\{O_k|\Psi(\alpha^0)\rangle\}$ we get:

$$\sum_{k=0}^p \delta\alpha_k \langle\Psi(\alpha^0)|O_{k'}O_k|\Psi(\alpha^0)\rangle = \langle\Psi(\alpha^0)|O_{k'}(\Lambda - \mathcal{H})|\Psi(\alpha^0)\rangle. \quad (2.46)$$

The parameters $\delta\alpha_k$ can be calculated by solving this linear system of $(p+1)$ equations, that can be written in a more compact way

$$f_{k'} = \sum_{k=0}^p \delta\alpha_k S_{kk'}, \quad (2.47)$$

where $f_{k'}$ are the generalized forces:

$$f_{k'} = \langle\Psi(\alpha^0)|O_{k'}(\Lambda - \mathcal{H})|\Psi(\alpha^0)\rangle \quad (2.48)$$

and $S_{kk'}$ is a $(p+1) \times (p+1)$ positive definite matrix given by:

$$S_{kk'} = \langle \Psi(\alpha^0) | O_k O_{k'} | \Psi(\alpha^0) \rangle. \quad (2.49)$$

The system can be reduced to p equations since $\delta\alpha_0$ is related to the normalization of the wave function. Indeed, considering Eq. (2.46) for $k' = 0$, the value of $\delta\alpha_0$ reduces to:

$$\delta\alpha_0 = \Lambda - E(\alpha^0) - \sum_{k=1}^p \delta\alpha_k S_{k0}. \quad (2.50)$$

Substituting (2.50) in (2.46), for $k' \neq 0$, we obtain the reduced system of equations:

$$\bar{f}_{k'} = \sum_{k=1}^p \delta\alpha_k \bar{S}_{kk'}, \quad (2.51)$$

where:

$$\bar{f}_k = \langle \Psi(\alpha^0) | O_k | \Psi(\alpha^0) \rangle \langle \Psi(\alpha^0) | \mathcal{H} | \Psi(\alpha^0) \rangle - \langle \Psi(\alpha^0) | O_k \mathcal{H} | \Psi(\alpha^0) \rangle \quad (2.52)$$

and

$$\bar{S}_{kk'} = S_{kk'} - S_{k0} S_{k'0}. \quad (2.53)$$

Now \bar{f}_k are proportional to the true forces, indeed $\bar{f}_k = -\frac{1}{2} \frac{\partial E(\alpha)}{\partial \alpha_k}$. Since at equilibrium $\bar{f}_k = 0$, implying $\delta\alpha_k = 0$, we get that there is no variation in the set of parameters when the stability condition $\frac{\partial E(\alpha)}{\partial \alpha_k} = 0$ is reached.

The stochastic reconfiguration algorithm is similar to a standard steepest descent (SD) calculation, where the expectation value of the energy $E(\alpha)$ is optimized by iteratively changing the parameters $\{\alpha_k\}$, according to the corresponding derivatives of the energy:

$$\alpha_k \rightarrow \alpha_k + \Delta t f_k, \quad (2.54)$$

where

$$f_k = -\frac{\partial E}{\partial \alpha_k} = -\frac{\langle \Psi(\alpha) | O_k \mathcal{H} + \mathcal{H} O_k | \Psi(\alpha) \rangle}{\langle \Psi(\alpha) | \Psi(\alpha) \rangle} + 2 \frac{\langle \Psi(\alpha) | O_k | \Psi(\alpha) \rangle \langle \Psi(\alpha) | \mathcal{H} | \Psi(\alpha) \rangle}{\langle \Psi(\alpha) | \Psi(\alpha) \rangle^2}. \quad (2.55)$$

Δt is a suitable small time step, which can be taken fixed or determined at each iteration by minimizing the energy expectation value. Indeed,

the variation of the total energy ΔE at each step is easily shown to be negative for small enough Δt because, in this limit,

$$\begin{aligned} \Delta E = E(\Psi(\alpha')) - E(\Psi(\alpha)) &= - \sum_{k=1}^p f_k \delta \alpha_k + O(\delta \alpha_k^2) = \\ &= - \Delta t \sum_{k=1}^p f_k^2 + O(\Delta t^2). \end{aligned} \quad (2.56)$$

Thus the method certainly converges to the minimum when all the forces vanish.

Similar considerations hold also for the stochastic reconfiguration algorithm. In fact, inverting Eq. (2.51), we get

$$\alpha_k \rightarrow \alpha_k + \Delta t \sum_{k'} \bar{S}_{k,k'}^{-1} \bar{f}_{k'}, \quad (2.57)$$

where we added a parameter Δt that can be tuned to control the change of the parameters. The energy variation for a small change of the parameters is given by:

$$\Delta E = -\Delta t \sum_{k,k'} \bar{S}_{k,k'}^{-1} \bar{f}_k \bar{f}_{k'}. \quad (2.58)$$

It is easily verified that the above term is always negative because the reduced matrix \bar{S} , as well as \bar{S}^{-1} is positive definite, being \bar{S} an overlap matrix with all positive eigenvalues.

For the SR and SD methods, a basic ingredient is that, at each iteration, the new parameters α' are close to the previous α , according to a prescribed distance. The fundamental difference between the two different techniques is just related to the definition of this distance Δ_α . Within the SR scheme, $\Delta_\alpha^{\text{SR}}$ is chosen to be the square distance between the two normalized wave functions, corresponding to the two different sets of variational parameters α and α' :

$$\Delta_\alpha^{\text{SR}} = ||\Psi(\alpha') - \Psi(\alpha)||^2 = 2 - 2 \frac{\langle \Psi(\alpha) | \Psi(\alpha') \rangle}{\sqrt{\langle \Psi(\alpha) | \Psi(\alpha) \rangle \langle \Psi(\alpha') | \Psi(\alpha') \rangle}}. \quad (2.59)$$

Inserting Eq. (2.40) in the previous one, we can express $\Delta_\alpha^{\text{SR}}$ as a function of the matrix \bar{S} , yielding

$$\Delta_\alpha^{\text{SR}} = \sum_{k,k'} \bar{S}_{k,k'} (\alpha'_k - \alpha_k) (\alpha'_{k'} - \alpha_{k'}). \quad (2.60)$$

Generically speaking, the minimization procedures we introduced are examples of a constrained optimization, because in order to find the

minimum of the energy in a stable way, we want to keep the variations of the wave function small. This is equivalent to find the minimum of the functional

$$\mathcal{F} = \Delta E + \bar{\Lambda} ||\Psi(\alpha')\rangle - |\Psi(\alpha)\rangle|^2 = - \sum_k f_k(\alpha'_k - \alpha_k) + \bar{\Lambda} \Delta_\alpha^{\text{SR}}. \quad (2.61)$$

Then, the stationary condition $\delta\mathcal{F}/\delta(\alpha'_k - \alpha_k) = 0$ lead to the stochastic reconfiguration scheme described in Eq. (2.57), with $\Delta t = 1/(2\bar{\Lambda})$. The steepest descent algorithm can be obtained as the stationary condition of a similar functional, in which there is a less efficient definition of distance. In fact, $\Delta_\alpha^{\text{SD}}$ is simply given by:

$$\Delta_\alpha^{\text{SD}} = \sum_{k=1}^p (\alpha'_k - \alpha_k)^2, \quad (2.62)$$

that is just the square distance among the two set of parameters. The advantage of SR, compared with SD, is now clear: sometimes a small change of the variational parameters correspond to a large change of the wave function, and the SR takes into account this effect through Eq. (2.57).

Now, it is worth to point out that, in order to compute the change in the variational parameters $\{\delta\alpha_k\}$ within the SR scheme, it is necessary to invert the matrix $\bar{S}_{k,k'}$, according to Eq. (2.57). If the eigenvalues of \bar{S} become too small, this leads to a divergence in the matrix elements of $\bar{S}_{k,k'}^{-1}$, making the minimization procedure unstable. In order to overcome this problem we use a combination of the Stochastic Reconfiguration and the Steepest Descent algorithm. Indeed, we define the change of the variational parameters $\{\delta\alpha_k\}$ as:

$$\bar{f}_{k'} = \sum_{k=1}^p \delta\alpha_k (\bar{S}_{kk'} + \epsilon \mathbb{I}), \quad (2.63)$$

where \mathbb{I} is the identity matrix. Eq. (2.63) imposes a cut-off on the eigenvalues of $\bar{S}_{k,k'}$, keeping the minimization procedure stable.

Eq. (2.51) is solved stochastically with the Monte Carlo algorithm. In practice we perform M_{SR} Metropolis steps in order to calculate the expectation values in Eqs. (2.52) and (2.53) with small enough fluctuations. Then, the linear system (2.51) is solved in order to find the variations $\delta\alpha_k$ and the new set of parameters is calculated, according to:

$$\alpha'_k = \alpha_k^0 + \Delta t \delta\alpha_k, \quad (2.64)$$

where Δt is a number that can be tuned in order to control the change of the parameters. Generally, one starts with a large Δt in order to

reach the minimum in few iterations and then Δt is decreased to reduce the fluctuations of the converged parameters. The new wave function $|\Psi(\alpha')\rangle$ is then considered as the starting state $|\Psi(\alpha^0)\rangle$ and the method is reiterated until convergence is achieved. Indeed, the stochastic nature of the system (2.51) implies that the forces \bar{f}_k are always determined with some statistical noise η_k and, even if the variational minimum is reached, the parameters will fluctuate around their mean values. Therefore, once convergence is reached, one must average over a certain number of iterations in order to find the optimal parameters.

2.5.1 The logarithmic derivative of the backflow parameters

In the last part of this section we address briefly the problem of computing the logarithmic derivative of the wave function with respect to the variational parameters. If a parameter α_p is in the Jastrow factor, the logarithmic derivative is very easy to compute. For example, let us consider the spin-Jastrow factor defined by:

$$J_s = \exp \left[\frac{1}{2} \sum_{i,j} v_{ij} S_i^z S_j^z \right], \quad (2.65)$$

where S^z is the z -component of the spin operator. The logarithmic derivative $O_{v_{ij}}(x)$, with respect to a generic parameter v_{ij} , is simply equal to $\langle x | S_i^z S_j^z | x \rangle$, where $|x\rangle$ is the electronic configuration on the lattice. Computing the logarithmic derivative of a parameter defined in the mean-field Hamiltonian (like Δ_{AF} or Δ_{BCS}) is much more difficult and we refer to [19] for a detailed description of the procedure. In this thesis, instead, we want to mention how to compute the logarithmic derivative for the backflow parameters, introduced in a previous section. We remember that the generic wave function for a correlated electron system can be constructed as the product of a Jastrow factor and the Slater determinant of a matrix $\Phi_{k,i,\sigma} \equiv \phi_k^b(\mathbf{r}_{i,\sigma})$, where the matrix elements, defined in Eq. (2.32), are the components of the new electron orbitals ϕ_k^b , that include backflow correlations, over the sites i occupied by the N electrons on the lattice. The index σ accounts for the spin of the electron(s) occupying the site i . Then the logarithmic derivative $O_{\eta_p}(x)$, with respect to a generic backflow parameter η_p , reads:

$$\begin{aligned} \frac{1}{\det[\Phi]} \frac{\partial}{\partial \eta_p} \det[\Phi] &= \frac{\partial}{\partial \eta_p} \ln \det[\Phi] = \frac{\partial}{\partial \eta_p} \text{Tr} \ln(\Phi) = \\ &= \text{Tr} \left(\Phi^{-1} \frac{\partial \Phi}{\partial \eta_p} \right), \end{aligned} \quad (2.66)$$

where $\frac{\partial \Phi}{\partial \eta_p}$ can be easily computed by differentiating every element of the matrix Φ with respect to the parameter η_p . Moreover, the inverse of the matrix Φ , required to compute the logarithmic derivative, does not cost extra computation time because it is already calculated for the Metropolis algorithm.

2.6 Green's Function Monte Carlo

The Green's Function Monte Carlo approach [15, 16] is based on a stochastic implementation of the power method technique that allows, in principle, to extract the actual ground state $|\Psi_{\text{GS}}\rangle$ of a given Hamiltonian \mathcal{H} , from any starting wave function $|\Psi_0\rangle$, provided that $\langle \Psi_{\text{GS}} | \Psi_0 \rangle \neq 0$:

$$|\Psi_{\text{GS}}\rangle = \lim_{n \rightarrow \infty} (\Lambda - \mathcal{H})^n |\Psi_0\rangle. \quad (2.67)$$

On large sizes it is not possible to evaluate exactly this recursive equation, because, after few steps, the application of $\Lambda - \mathcal{H}$ generates transitions to a very large number of different states, implying a huge amount of memory occupation. Therefore, we define a stochastic approach, in the sense that the wave function

$$\langle x | \Psi_n \rangle = \langle x | (\Lambda - \mathcal{H})^n | \Psi_0 \rangle, \quad (2.68)$$

is evaluated in a stochastic way. To this purpose, we define the so-called *walker*, which corresponds, at each iteration n of the Markov chain, to an electronic configuration $|x_n\rangle$ with an associated weight ω_n (roughly speaking associated to the amplitude of the wave function at $|x_n\rangle$, see below). The goal of the Green's function MC approach is to define a Markov process, yielding, after a large number n of iterations, a probability distribution $P_n(x_n, \omega_n)$ ³ for the walker, which determines the ground state wave function $|\Psi_{\text{GS}}\rangle$. To be specific, in the most simple formulation we would require:

$$\int d\omega \omega_n P_n(x_n, \omega_n) = \langle x_n | \Psi_n \rangle, \quad (2.69)$$

i.e., the amplitude of the wave function $|\Psi_n\rangle$ at x_n is obtained by integrating, over all the weights ω_n , the probability $P_n(x_n, \omega_n)$. In order to construct a Markov chain for solving the ground state of the Hamiltonian \mathcal{H} , it is necessary to assume that all the matrix elements of the so-called Green's function

$$G_{x',x} = \langle x' | \Lambda - \mathcal{H} | x \rangle = \Lambda \delta_{x',x} - \mathcal{H}_{x',x}, \quad (2.70)$$

³In the forthcoming we will indicate the electronic configuration $|x\rangle$ just as x .

are positive definite, so that they may have a meaning of probability. For the diagonal element $G_{x',x}$ there is no problem: we can always satisfy this assumption by taking a sufficiently large shift Λ . However, the requirement of positiveness is indeed important, and non trivial, for the non-diagonal elements of G , and is fulfilled only by particularly simple Hamiltonians. If it is not fulfilled, i.e., if $G_{x',x} < 0$ for some pairs (x', x) , we say that we are in presence of the so-called sign problem, that will be discussed in the following. Once positiveness is assumed to hold, we can divide up the Green's function into the product of two factors: a stochastic matrix $p_{x',x}$ (by definition, a matrix with all positive elements and with the normalization condition $\sum_{x'} p_{x',x} = 1$) times a scale factor b_x . Indeed, if we define $b_x = \sum_{x'} G_{x',x}$ to be such a scale factor, then $p_{x',x} = G_{x',x}/b_x$ is trivially positive and column normalized, and is therefore the stochastic matrix we are looking for.

Now we are able to define a Markov process that leads to the condition (2.69) after a large enough number of iterations. Indeed, given (x_n, ω_n) we can generate x_{n+1} with probability p_{x_{n+1},x_n} and update the weight according to $\omega_{n+1} = \omega_n b_{x_n}$. This Markov process can be very easily implemented for generic correlated Hamiltonians on a lattice, since the number of non-zero entries in the stochastic matrix p_{x_{n+1},x_n} , for given x_n , is small, and typically growing only as the number of lattice sites L . Now, it is immediate to verify that the conditional probability K of the new walker (x_{n+1}, ω_{n+1}) , given the old one at (x_n, ω_n) , is simply:

$$K(x_{n+1}, \omega_{n+1} | x_n, \omega_n) = p_{x_{n+1},x_n} \delta(\omega_{n+1} - \omega_n b_{x_n}). \quad (2.71)$$

Thus, the Master equation corresponding to the probability density $P_n(x_n, \omega_n)$ is given by

$$P_{n+1}(x_{n+1}, \omega_{n+1}) = \sum_x \int d\omega K(x_{n+1}, \omega_{n+1} | x_n, \omega_n) P_n(x_n, \omega_n). \quad (2.72)$$

Finally, given Eq. (2.72) it can be proved, by means of the induction principle, that the following relation holds⁴:

$$\Psi_{\text{GS}}(x) = \lim_{n \rightarrow \infty} \langle \omega_n \delta_{x,x_n} \rangle = \lim_{n \rightarrow \infty} \int d\omega \omega_n P_n(x, \omega_n). \quad (2.73)$$

Now, within this formalism, we can compute the ground-state energy, by averaging the random variable $e(x) = \sum_{x'} \mathcal{H}_{x',x} = \Lambda - b_x$. In

⁴We can take as a starting probability distribution $P(x_0, \omega_0) = \delta_{\omega_0-1} \delta_{x_0-x_0}$.

fact:

$$\begin{aligned}
\frac{\langle \omega_n e(x_n) \rangle}{\langle \omega_n \rangle} &= \frac{\sum_{x_n} \int d\omega_n \omega_n e(x_n) P_n(x_n, \omega_n)}{\sum_{x_n} \int d\omega_n \omega_n P_n(x_n, \omega_n)} = \frac{\sum_{x_n} e(x_n) \Psi_n(x_n)}{\sum_{x_n} \Psi_n(x_n)} \\
&= \frac{\sum_{x'x_n} \mathcal{H}_{x'x_n} \Psi_n(x_n)}{\sum_{x_n} \Psi_n(x_n)} = \frac{\sum_{x'} \langle x' | \mathcal{H} | \Psi_n \rangle}{\sum_{x_n} \Psi_n(x_n)},
\end{aligned} \tag{2.74}$$

which, in the limit $n \rightarrow \infty$ tends to the ground state energy, according to Eq. (2.73).

However, in Eq. (2.74), the calculation of the energy, with the above described Green's function technique, will not satisfy the zero variance property, which holds instead for the variational Monte Carlo we introduced before. In fact, the random quantity $e(x)$, defined above, does not depend on any variational guess $|\Psi_g\rangle$ and, therefore, its statistical fluctuations cannot be reduced by a better wave function $|\Psi_g\rangle$, as it is possible in the VMC case.

2.6.1 Importance sampling

It is possible to recover this important property of the variational Monte Carlo, by a slight modification of the iteration technique. To this purpose, it is enough to consider the so-called importance sampling Green's function:

$$\bar{G}_{x',x} = \Psi_g(x') G_{x',x} / \Psi_g(x). \tag{2.75}$$

Whenever $\bar{G}_{x',x} \geq 0$ for every (x', x) we can decompose it in the following manner, to define a Markov chain similar to the one we already introduced:

$$\begin{aligned}
p_{x',x} &= \bar{G}_{x',x} / b_x \\
b_x &= \sum_{x'} \bar{G}_{x',x} = \Lambda - \frac{\sum_{x'} \Psi_g(x') \mathcal{H}_{x',x}}{\Psi_g(x)} = \Lambda - e_L(x),
\end{aligned} \tag{2.76}$$

where $e_L(x)$ is the local energy already defined in Eq. (2.5). Now, if the trial wave function $|\Psi_g\rangle$ used in the importance sampling procedure coincides with the correct ground-state wave function, i.e. $\Psi_g(x) = \Psi_{\text{GS}}(x)$, then $e_L(x) = E_{\text{GS}}$ is a constant, and statistical fluctuations vanish exactly.

All the previous derivations can be repeated also in this case with importance sampling, the difference being only appropriate factors depending on $|\Psi_g\rangle$. We thus obtain for instance:

$$\langle \omega_n \delta_{x,x_n} \rangle = \Psi_g(x) \Psi_n(x) \tag{2.77}$$

$$\begin{aligned}
E_{\text{GS}} &= \lim_{n \rightarrow \infty} \frac{\langle \omega_n e_L(x_n) \rangle}{\langle \omega_n \rangle} = \lim_{n \rightarrow \infty} \frac{\langle \omega_n \sum_{x'} \Psi_g(x') \mathcal{H}_{x', x_n} / \Psi_g(x_n) \rangle}{\langle \omega_n \rangle} = \\
&= \lim_{n \rightarrow \infty} \frac{\langle \Psi_g | \mathcal{H} (\Lambda - \mathcal{H})^n | \Psi_0 \rangle}{\langle \Psi_g | (\Lambda - \mathcal{H})^n | \Psi_0 \rangle}.
\end{aligned} \tag{2.78}$$

The zero variance property is evident from the previous equation. Indeed, if $|\Psi_g\rangle = |\Psi_{\text{GS}}\rangle$, $E_n = \frac{\langle \omega_n e_L(x_n) \rangle}{\langle \omega_n \rangle} = E_{\text{GS}}$, with no statistical fluctuations.

Since the convergence of the above limit is exponentially fast in n (at least for any finite size lattice, where a finite gap to the first excitation exists), it is enough to stop the iteration to a reasonably small finite $n = l$. Then, instead of repeating the Markov chain several times up to $n = l$, to accumulate statistics, it is clearly more convenient to average over a long Markov chain with $N \gg l$, where N is the total number of iterations, and considering the corresponding estimates in Eq. (2.78):

$$E_{\text{GS}} \simeq \frac{\sum_{n > n_0}^N Q_n^l e_L(x_n)}{\sum_{n > n_0}^N Q_n^l}, \tag{2.79}$$

where n_0 is the number of iterations required for the statistical equilibration of the Markov process and the weighting factors Q_n^l are given by:

$$Q_n^l = \prod_{i=1}^l b_{x_{n-i}}. \tag{2.80}$$

So, at each discrete time $n-l$ we can take an equilibrated configuration, and consider l iterations of the Markov process with initial condition $\omega_{n-l} = 1$, leading, after l iterations, to a final weight $\omega_l = Q_n^l$, at time n .

2.6.2 Forward walking technique

Besides energy, Green's function Monte Carlo can be also used efficiently to compute expectation values of local operators \widehat{O} , i.e., operators which are diagonal on all the elements of the configuration basis $|x\rangle$,

$$\widehat{O}|x\rangle = O_x|x\rangle, \tag{2.81}$$

where O_x is the eigenvalue corresponding to the configuration x . Also for local operators we can define local estimators $O_L(x) = \frac{\langle \Psi_g | \widehat{O} | x \rangle}{\langle \Psi_g | x \rangle} = O_x$, but, in contrast with what happens for energy, we *cannot* write the

following equality:

$$O_{\text{GS}} = \lim_{n \rightarrow \infty} \frac{\langle \omega_n O_{x_n} \rangle}{\langle \omega_n \rangle} = \frac{\langle \Psi_g | \widehat{O} | \Psi_{\text{GS}} \rangle}{\langle \Psi_g | \Psi_{\text{GS}} \rangle}, \quad (2.82)$$

because the ground state is not an eigenstate of the operator \widehat{O} . In fact, the quantity $\langle O \rangle_{\text{MA}} = \frac{\langle \Psi_g | \widehat{O} | \Psi_{\text{GS}} \rangle}{\langle \Psi_g | \Psi_{\text{GS}} \rangle}$, called mixed average, is obviously equal to O_{GS} only if the ground state is an eigenstate of \widehat{O} , like happens for the energy.

In order to compute the mean value of a generic local operator \widehat{O} over the ground state, we introduce the so-called *forward walking* technique, i.e., $O_{\text{GS}} = \lim_{n \rightarrow \infty} \frac{\langle \omega_n O_{x_{n-m}} \rangle}{\langle \omega_n \rangle}$. Indeed we have that:

$$\frac{\langle \omega_n O_{x_{n-m}} \rangle}{\langle \omega_n \rangle} = \frac{\langle \Psi_g | (\Lambda - \mathcal{H})^m \widehat{O} (\Lambda - \mathcal{H})^{n-m} | \Psi_0 \rangle}{\langle \Psi_g | (\Lambda - \mathcal{H})^n | \Psi_0 \rangle} \rightarrow \frac{\langle \Psi_{\text{GS}} | \widehat{O} | \Psi_{\text{GS}} \rangle}{\langle \Psi_{\text{GS}} | \Psi_{\text{GS}} \rangle}. \quad (2.83)$$

From a statistical point of view, Eq. (2.83) amounts first to sample a configuration x after $n - m$ Green's Function Monte Carlo steps, then to measure the quantity $\langle x | O | x \rangle$ and finally to let the walker propagate forward for further m steps. In order to evaluate the stochastic average, an approach similar to that done for the energy is possible. Indeed, since the convergence of the above limit is exponentially fast in n , it is enough to stop the iteration to a reasonably small finite $n = l$, and then to average over a long Markov chain with $N \gg l$, where N is the total number of iterations. In particular, in this case we get:

$$E_{\text{GS}} \simeq \frac{\sum_{n > n_0}^N Q_n^l O(x_{n-m})}{\sum_{n > n_0}^N Q_n^l}, \quad (2.84)$$

where

$$Q_n^l = \prod_{i=1}^l b_{x_{n-i}}. \quad (2.85)$$

In the above equation, $\omega_{n-l} = 1$ is assumed, implying that $m \leq l$. However, we need a very large m to filter out the ground state from the left-hand side state $\langle \Psi_g |$.

An alternative approximate way to evaluate the mean value of a generic local operator \widehat{O} over the ground state is to use the so-called *Ceperley approximation*:

$$\langle \Psi_{\text{GS}} | \widehat{O} | \Psi_{\text{GS}} \rangle \sim 2 \langle O \rangle_{\text{MA}} - \langle O \rangle_{\text{VMC}}, \quad (2.86)$$

where $\langle O \rangle_{\text{VMC}} = \frac{\langle \Psi_g | O | \Psi_g \rangle}{\langle \Psi_g | \Psi_g \rangle}$ is the simple variational estimate corresponding to $|\Psi_g\rangle$. This approach is justified provided the variational wavefunction $|\Psi_g\rangle$ is very close to $|\Psi_{\text{GS}}\rangle$, so that it can be written as $|\Psi_g\rangle = |\Psi_{\text{GS}}\rangle + \epsilon|\Psi'\rangle$, with $|\Psi_g\rangle$ and $|\Psi'\rangle$ normalized and $\epsilon \ll 1$.

2.6.3 Many walker formulation

Apart the aforementioned Ceperley approximation, the previously described procedures are, in principle, free from any approximation and they give exact results within the statistical errors (if the condition $\bar{G}_{x',x} \geq 0$ holds). Unfortunately, the weight Q_n^l grows exponentially by increasing l , implying a divergent variance in the energy average. Indeed, Q_n^l is a product of l different factors and it can assume very large or very small values. This problem has a simple solution by considering the Green's Function Monte Carlo technique with many walkers and by introducing a reconfiguration scheme, which enables to drop out the irrelevant walkers with small weights. Calandra and Sorella [16] have introduced a reconfiguration scheme working at fixed number of walkers, in a way that allows us to control the bias due to the finite walker population.

We consider M walkers and label the corresponding configurations and weights with a couple of vectors $(\mathbf{x}, \boldsymbol{\omega})$, with each component (x_i, ω_i) , $i = 1, \dots, M$ corresponding to the i -th walker. It is then easy to generalize the Master equation Eq. (2.72) to many independent walkers. If the evolution of P is done without further restrictions, each walker is uncorrelated from any other one, and we have:

$$P_n(x_1 \dots x_M, \omega_1 \dots \omega_M) = P_n(x_1, \omega_1) \dots P_n(x_M, \omega_M). \quad (2.87)$$

Similarly to the previous case (2.73), we can define the state evolved at iteration n with the Green's function \bar{G} :

$$\Psi_n(x)\Psi_g(x) = \left\langle \frac{1}{M} \sum_{i=1}^M \omega_i \delta_{x,x_i} \right\rangle = \int [d\boldsymbol{\omega}] \sum_{\mathbf{x}} \frac{\sum_j \omega_j \delta_{x,x_j}}{M} P_n(\boldsymbol{\omega}, \mathbf{x}). \quad (2.88)$$

where the symbol $[d\boldsymbol{\omega}]$ indicates the M dimensional integral over the ω_i variables.

Since we are interested in the state $|\Psi_n\rangle$, we can define a reconfiguration process (that is the process of removing the most irrelevant walkers) that changes the probability distribution P_n without changing the statistical average $\langle \frac{1}{M} \sum_{i=1}^M \omega_i \delta_{x,x_i} \rangle$, that is relevant in the calculation of $|\Psi_n\rangle$. This can be obtained by a particular Markov process applied to the configuration $(\mathbf{x}, \boldsymbol{\omega})$, which leads to new walkers $(\mathbf{x}', \boldsymbol{\omega}')$.

Each new walker (x'_j, ω'_j) , with $j = 1, \dots, M$, will have the same weight $\omega'_j = \bar{\omega} = \frac{\sum_j \omega_j}{M}$ and an arbitrary configuration x'_j , among the M possible old configurations $x_k, k = 1, \dots, M$, chosen with a probability p_k proportional to the weight of that configuration, $p_k = \omega_k / \sum_j \omega_j$.

It is clear that, after this reconfiguration, the new set of M walkers have by definition the same weights $\omega_j = \bar{\omega}$, and most of the irrelevant walkers with small weights have dropped out. It is also easy to derive the Master equation corresponding to this reconfiguration Markov process:

$$P'_n(\boldsymbol{\omega}', \boldsymbol{x}') = \sum_{\boldsymbol{x}} \int [d\boldsymbol{\omega}] K(\boldsymbol{x}', \boldsymbol{\omega}' | \boldsymbol{x}, \boldsymbol{\omega}) P_n(\boldsymbol{\omega}, \boldsymbol{x}), \quad (2.89)$$

where the kernel K is given by

$$K(\boldsymbol{x}', \boldsymbol{\omega}' | \boldsymbol{x}, \boldsymbol{\omega}) = \prod_{j=1}^M \left(\frac{\sum_i \omega_i \delta_{x'_j, x_i}}{\sum_i \omega_i} \right) \delta \left(\omega'_j - \frac{\sum_i \omega_i}{M} \right). \quad (2.90)$$

Let us note that K is simple, in this case, because all the new walkers are independent from each other, and K factorizes for each walker. We omit from the thesis the proof that this reconfiguration scheme does not influence the relevant average we are interested in. Such a proof can be found in [16].

2.6.4 Fixed Node approximation

In a fermionic system the condition of positiveness $\bar{G}_{x',x} \geq 0$ for every (x', x) is not fulfilled in general. This is due to the antisymmetric nature of the fermionic wave function. Indeed, starting from a given wave function $|\Psi_0\rangle$, we need to change its nodes in order to converge to the actual ground state $|\Psi_{\text{GS}}\rangle$, recovering the correct sign. In principle, this can be done redefining the key ingredients of the Markov chain:

$$\begin{aligned} p_{x',x} &= |\bar{G}_{x',x}| / |b_x| \\ b_x &= \sum_{x'} |\bar{G}_{x',x}| s_{x',x}, \end{aligned} \quad (2.91)$$

where $s_{x',x}$ is the sign of the Green's function $\bar{G}_{x',x}$ between the configurations x' and x . As a consequence, the weighting factor, appearing in the evaluation of energy and local operators, is modified as well:

$$Q_n^l = \prod_{j=1}^l b_{x_{n-j}} s_{x_{n-j+1}, x_{n-j}}. \quad (2.92)$$

However, this procedure is not applicable in practice, because the average sign,

$$\langle s_l \rangle = \frac{\sum_n Q_n^l}{\sum_n |Q_n^l|}, \quad (2.93)$$

vanishes exponentially with l . Indeed, walkers with positive and negative weights cancel almost exactly, giving rise to an exponentially small quantity to sample, with huge fluctuations. A possible way to overcome this problem is the so-called *fixed node approximation* [17] that allows us to avoid the sign problem.

In this approach, an effective Hamiltonian is defined, starting from \mathcal{H} , by adding a perturbation O :

$$\mathcal{H}_{\text{eff}} = \mathcal{H} + O. \quad (2.94)$$

The operator O is defined through its matrix elements and depends upon a given guiding function $|\Psi\rangle$, which we can take as the best available variational state $|\Psi^{\text{VMC}}\rangle$:

$$O_{x',x} = \begin{cases} -\mathcal{H}_{x',x} & \text{if } x' \neq x \text{ and } s_{x',x} < 0 \\ 0 & \text{if } x' \neq x \text{ and } s_{x',x} \geq 0 \\ \sum_{y:s_{y,x}<0} \mathcal{H}_{y,x} \frac{\Psi_y^{\text{VMC}}}{\Psi_x^{\text{VMC}}} & \text{if } x' = x, \end{cases} \quad (2.95)$$

where $\Psi_x^{\text{VMC}} = \langle x | \Psi^{\text{VMC}} \rangle$. One has to notice that the above operator annihilates the guiding function, namely $O|\Psi^{\text{VMC}}\rangle = 0$. Therefore, whenever the guiding function is close to the exact ground state of \mathcal{H} the perturbation O is expected to be small and the effective Hamiltonian becomes very close to the original one. Moreover, it can be proven that the ground state of \mathcal{H}_{eff} has lower variational energy than the one obtained using $|\Psi_{\text{VMC}}\rangle$ as a trial wave function in VMC. Within \mathcal{H}_{eff} , all the matrix elements of \bar{G} are non-negative and, therefore, it can represent a transition probability in configurations space, apart from a normalization factor $b_x = \sum_{x'} \bar{G}_{x',x}$. Moreover, since the matrix elements of \bar{G} are non-negative, the ground state of \mathcal{H}_{eff} has the same signs of the chosen guiding function. This point is very important, since we need to choose variational wave functions with the best possible nodes to get accurate estimates of the ground-state energy. In this respect, backflow correlations are very important, because they enter the determinantal part of the wave function, being able to change its nodes.

2.7 Testing the accuracy of the backflow wave function

In order to test how backflow correlations can be accurate, improving the ground-state energies obtained with a given trial wave function, we can start considering the comparison of the variational results with the exact ones on the 18-site cluster at half filling. The exact energies are obtained by means of the Lanczos method [52], that is an iterative procedure that allows us to get the lowest eigenstates of Hermitian matrices. In principle, in order to obtain the exact ground-state of the Hamiltonian it is necessary to perform a number of iterations equal to the dimension of the Hilbert space. In practice, the greatest advantage of this method is that a very accurate approximation of the ground state is obtained after a very small number of iterations, typically of the order of 100, depending on the model. The main limitation of this technique is the exponential growing of the Hilbert space, implying huge computer memory requirements, even for small lattices.

In Fig. (2.4), we show the accuracy of the variational $|\Psi_{\text{SL}}\rangle = J|\text{BCS}\rangle$ wave function (with and without backflow correlations) for two values of the frustrating ratio, i.e., $t'/t = 0$ and 0.7 , at half-filling. We remind that $|\Psi_{\text{SL}}\rangle$ is the variational wave function used to describe a spin-liquid state. The accuracy of the energy is defined as $\Delta E/E_0 = (E_0 - E_v)/E_0$, E_0 and E_v being the exact and the variational values, respectively. The backflow term is able to highly improve the accuracy both for weak and strong couplings, especially in presence of frustration, where there is an order of magnitude improvement.

In Fig. (2.5), we show also the overlap between the same variational ground state wave function (with and without backflow correlations) and the exact one, computed within the Lanczos technique, at half-filling, for two values of the frustrating ratio, $t'/t = 0$ and 0.7 . Also in this case backflow correlations bring an improvement, both at intermediate and strong coupling.

The same comparison, between variational and exact results, can be done also away from half-filling. Even if in this thesis we do not address physical problems connected with the doped regime, which may be relevant for High- T_c superconductivity, we studied also this case for completeness. In particular, we focus on the case of 10 electrons on a 18-site lattice. For such a system, in Fig. (2.6) and in Fig. (2.7), we show again the accuracy in the variational ground-state energy of $|\Psi_{\text{SL}}\rangle$, with and without backflow correlations, and the overlap between the variational wave function and the exact one. We notice that also in this less correlated regime, the backflow term allows the variational

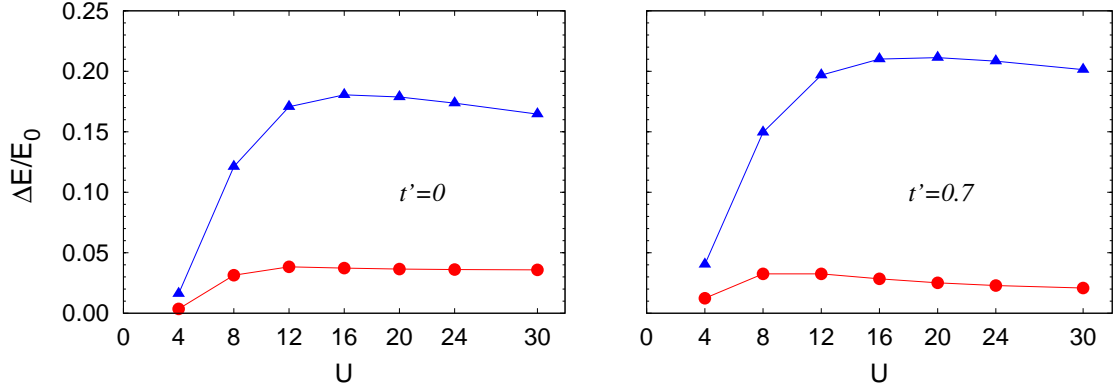


Figure 2.4: Accuracy of the variational energy for the $|\Psi_{\text{SL}}\rangle = J|\text{BCS}\rangle$ wave function (with and without backflow correlations) for two values of the frustrating ratio, $t'/t = 0$ and 0.7 at half-filling on the 18-site lattice. The accuracy of the energy is defined as $\Delta E/E_0 = (E_0 - E_v)/E_0$, E_v and E_0 being the variational value and the exact one, respectively. The BCS state without backflow correlations is denoted by blue triangles, the BCS state with backflow correlations by red circles.

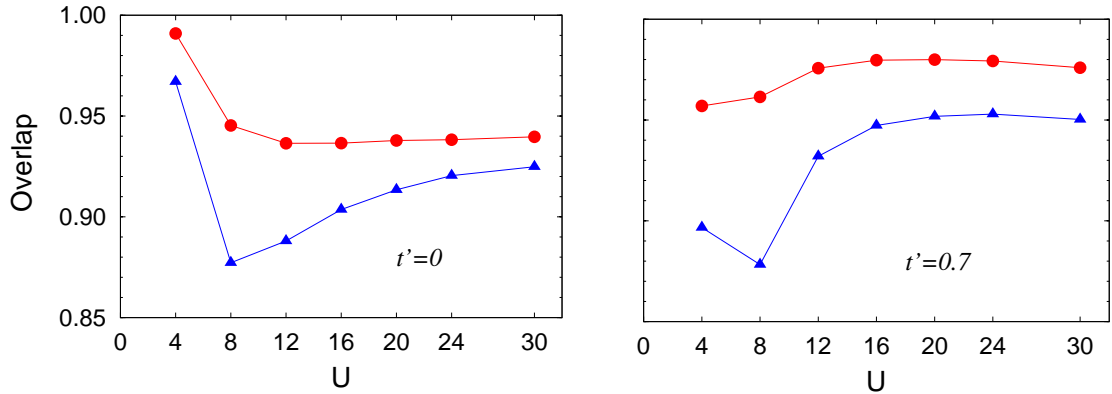


Figure 2.5: Overlap between the variational ground state wave functions and the exact one at half-filling on the 18-site lattice. The overlap between the $|\Psi_{\text{SL}}\rangle$ variational state without backflow correlations and the exact one is denoted by blue triangles, the overlap between the $|\Psi_{\text{SL}}\rangle$ variational state with backflow correlations and the exact one is denoted by red circles.

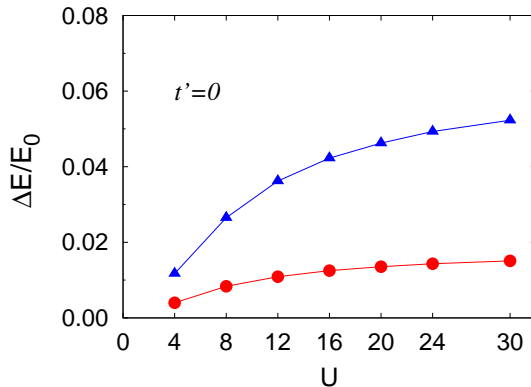


Figure 2.6: Accuracy of the variational energy for the $|\Psi_{\text{SL}}\rangle = J|\text{BCS}\rangle$ wave function (with and without backflow correlations) in the doped regime (10 electrons for 18 sites), for the unfrustrated case, $t' = 0$. The accuracy of the energy is defined as $\Delta E/E_0 = (E_0 - E_v)/E_0$, E_v and E_0 being the variational and the exact values, respectively. The BCS state without backflow correlations is denoted by blue triangles, the BCS state with backflow correlations by red circles.

energy to be very close to the actual ground-state one. However, since we are far from half-filling, electronic correlation is less important and accuracy is quite good already without applying backflow correlations. As far as overlap is regarded, we would like to notice that in this case the behaviour of the overlap is a bit different from what happens in the half-filled regime, because now it becomes smoothly worse as U is increased (even if it is always better when including backflow correlations) (see Fig. (2.7)).

Another useful comparison can be made between the spin liquid wave function with backflow correlations and the wave function obtained applying one Lanczos step over the spin liquid one. The Lanczos step wave function, introduced in [53], is given by:

$$|\Psi_{\text{LS}}\rangle = (1 + \alpha\mathcal{H})|\Psi_{\text{SL}}\rangle, \quad (2.96)$$

where \mathcal{H} is the Hamiltonian of the system and α is a variational parameter to be optimized. The variational wave function introduced in Eq. (2.96) is always an improvement with respect to the simple $|\Psi_{\text{SL}}\rangle$, not only because we add one more variational parameter to be optimized, but mainly because we are applying the first step of the iterative Lanczos method, which converges to the actual ground state in few iterations, as discussed before. In order to compute the energy,

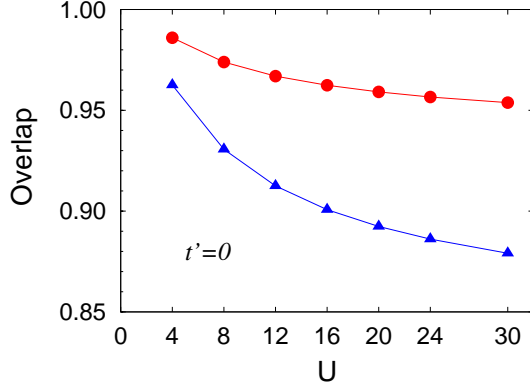


Figure 2.7: Overlap between the variational ground state wave functions and the exact one in the doped regime (10 electrons for 18 sites), for the unfrustrated case. The overlap between the $|\Psi_{\text{SL}}\rangle$ variational state without backflow correlations and the exact one is denoted by blue triangles, the overlap between the $|\Psi_{\text{SL}}\rangle$ variational state with backflow correlations and the exact one is denoted by red circles.

we have that:

$$E^{\text{LS}} = \frac{\langle \Psi_{\text{LS}} | \mathcal{H} | \Psi_{\text{LS}} \rangle}{\langle \Psi_{\text{LS}} | \Psi_{\text{LS}} \rangle} = \frac{\sum_{x',x} \Psi_{\text{LS}}(x') \mathcal{H}_{x',x} \Psi_{\text{LS}}(x)}{\sum_x \Psi_{\text{LS}}^2(x)}. \quad (2.97)$$

By defining the local energy as

$$E_x^{\text{LS}} = \sum_{x'} \mathcal{H}_{x',x} \frac{\Psi_{\text{LS}}(x')}{\Psi_{\text{LS}}(x)}, \quad (2.98)$$

we obtain

$$E^{\text{LS}} = \frac{\sum_x E_x^{\text{LS}} \Psi_{\text{LS}}^2(x)}{\sum_x \Psi_{\text{LS}}^2(x)}, \quad (2.99)$$

which can be stochastically sampled using Monte Carlo by generating configurations according to $\Psi_{\text{LS}}^2 / \sum_{x'} \Psi_{\text{LS}}^2(x')$. Notice that the ratio $\Psi_{\text{LS}}(x') / \Psi_{\text{LS}}(x)$, necessary to the Metropolis algorithm, is evaluated by using the fact that

$$\frac{\Psi_{\text{LS}}(x')}{\Psi_{\text{LS}}(x)} = \frac{\langle x' | (1 + \alpha \mathcal{H}) | \Psi \rangle}{\langle x | (1 + \alpha \mathcal{H}) | \Psi \rangle} = \frac{\Psi(x')}{\Psi(x)} \left(\frac{1 + \alpha E_{x'}}{1 + \alpha E_x} \right). \quad (2.100)$$

Therefore, at each Monte Carlo step, we have to calculate the local energy of the trial wave function $|\Psi\rangle$ both on configurations x and x' . This kind of calculation takes operations of order the linear dimension

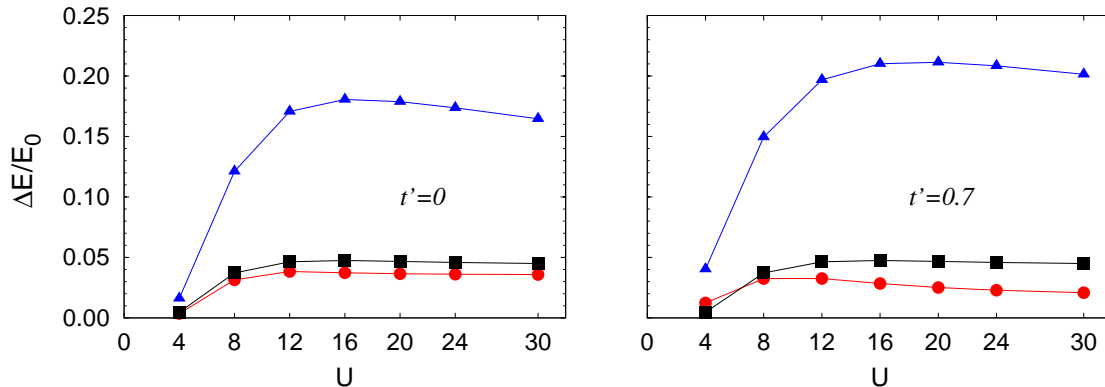


Figure 2.8: Accuracy of the variational energy for the $|\Psi_{\text{SL}}\rangle = J|\text{BCS}\rangle$ wave function, with and without backflow correlations, and the wave function with one Lanczos step introduced in Eq. (2.96). We show data for two values of the frustrating ratio, i.e., $t'/t = 0$ and 0.7 at half-filling on the 18-site lattice. The accuracy of the energy is defined as $\Delta E/E_0 = (E_0 - E_v)/E_0$, E_0 and E_v being the exact and the variational values, respectively. The BCS state without backflow correlations is denoted by blue triangles, the BCS state with backflow correlations by red circles, the Lanczos step by black squares.

of the lattice times a big prefactor. Notice that we have to evaluate all the matrix elements $\langle x' | \mathcal{H} | \Psi \rangle$, even if the movement from x to x' is not accepted.

In Fig. (2.8), we show the accuracy in the variational energy of three different wave functions on an 18-site lattice at half-filling. We report $|\Psi_{\text{SL}}\rangle = J|\text{BCS}\rangle$, with and without backflow correlations, and the wave function introduced in Eq. (2.96). We notice that the wave function with backflow correlations is the best performing among the three ones, except at small U 's in the frustrated regime, where the wave function with one Lanczos step is slightly more accurate.

Moreover, the spin liquid wave function with one Lanczos step $|\Psi_{\text{LS}}\rangle$ is not size-consistent. In fact, the matrix \mathcal{H} allows us to connect configurations x and x' that differ for the hopping of one electron between nearest-neighbour or next-nearest neighbour sites. When the lattice size increases, these two configurations become more and more similar, differing by at most one electron position. This fact makes the effect of the matrix \mathcal{H} negligible in a large size, containing several electrons. As a consequence, the Lanczos step wave function loses accuracy as the system size increases. For example, for 98 sites with $U/t = 20$ and $t'/t = 0.7$, the energy per site with the backflow wave function is $E_{\text{back}} = -0.2352(1)$, while the one with one Lanczos step

is $E_{\text{LS}} = -0.2310(1)$ (for 18 sites they are $E_{\text{back}} = -0.2374(1)$ and $E_{\text{LS}} = -0.2357$). The Fixed Node energy obtained with the backflow state reaches $E_{\text{FN}} = -0.2395(1)$. These numbers can be compared with a non-variational estimate of the exact ground state energy, that can be obtained from the wave functions with zero and one Lanczos step [68], $E \simeq -0.246$.

We also compared our wave functions with backflow correlations, with a variational wave function that is the ground state of the following mean-field Hamiltonian

$$\begin{aligned} \mathcal{H}_{\text{BCS+AF}} = & \sum_{i,j,\sigma} t_{ij} c_{i,\sigma}^\dagger c_{j,\sigma} - \mu \sum_{i,\sigma} c_{i,\sigma}^\dagger c_{i,\sigma} + \sum_{i,j} \Delta_{ij} \left(c_{i,\uparrow}^\dagger c_{j,\downarrow}^\dagger + c_{j,\uparrow}^\dagger c_{i,\downarrow}^\dagger \right) \\ & + \text{H.c.} + \Delta_{\text{AF}} \sum_j \exp[i\mathbf{Q}\mathbf{R}_j] (\mathbf{S}_j \cdot \mathbf{n}_j), \end{aligned} \quad (2.101)$$

that combines the BCS pairing Δ_{ij} with the antiferromagnetic order parameter Δ_{AF} . This Hamiltonian is quadratic in the fermionic operators and so it can be easily diagonalized to get its ground state:

$$|\Psi_{\text{BCS+AF}}\rangle = \exp \left(\frac{1}{2} \sum_{i,j,\sigma_i,\sigma_j} f_{i,j}^{\sigma_i,\sigma_j} c_{i,\sigma_i}^\dagger c_{j,\sigma_j}^\dagger \right) |0\rangle, \quad (2.102)$$

where $f_{i,j}^{\sigma_i,\sigma_j}$ is the pairing function. Notice that in the case of a standard BCS Hamiltonian, with $\Delta_{\text{AF}} = 0$ or even with Δ_{AF} along z , we have that $f_{i,j}^{\uparrow i, \uparrow j} = f_{i,j}^{\downarrow i, \downarrow j} = 0$, while in presence of a magnetic field in the $x - y$ plane the pairing function acquires non-zero contributions also in the triplet channel. This kind of wave function was first introduced in [29] and then used to study ^3He systems and small atoms and molecules [69]. It has been also used to study the doped Heisenberg model (that is the $t - J$ model) where antiferromagnetism vanishes away from half-filling and superconductivity should appear [70, 71]. The technical difficulty when dealing with such a state is that, given a generic configuration $|x\rangle$ with definite z -component of the spin, we have that

$$\langle x | \Psi_{\text{BCS+AF}} \rangle = \mathcal{P}f[\mathcal{F}], \quad (2.103)$$

where $\mathcal{P}f[\mathcal{F}]$ is the Pfaffian of the pairing function matrix $\mathcal{F}_{i,j} = f_{i,j}^{\sigma_i,\sigma_j}$ ⁵. It should be noticed that, whenever $f_{i,j}^{\uparrow i, \uparrow j} = f_{i,j}^{\downarrow i, \downarrow j} = 0$, $\langle x | \Psi \rangle$ reduces to a standard determinant.

⁵The Pfaffian of a $2n \times 2n$ antisymmetric matrix M is equal to the antisymmetric product of its matrix elements, i.e., $\mathcal{P}f[M] = \mathcal{A}\{M_{1,2}M_{3,4} \dots M_{2n-1,2n}\}$, with the constraint that each term $M_{i_1,j_1}M_{i_2,j_2} \dots M_{i_n,j_n}$ has $i_k < j_k$ and $i_1 < i_2 < \dots < i_n$.

Wave functions	$E(n_h = 0)$	$E(n_h = 4)$	$E(n_h = 8)$
$ \Psi_{\text{BCS+AF}}\rangle$	-0.51737(6)	-0.54281(7)	-0.57460(9)
$ \Psi_{\text{SL}}\rangle$	-0.4801(1)	-0.53375(5)	-0.58801(4)
$ \Psi_{\text{AF}}\rangle$	-0.52108(2)		-0.60250(2)

Table 2.3: Variational energies for the Hubbard model on the unfrustrated square lattice with 162 lattice sites and the number of holes $n_h = 0, 4, 8$. Three different wave functions are considered: a combination of BCS pairing and antiferromagnetic order parameter $|\Psi_{\text{BCS+AF}}\rangle$, a spin liquid one with backflow correlations $|\Psi_{\text{SL}}\rangle = J|\text{BCS+Backflow}\rangle$ and an antiferromagnetic one with backflow correlations $|\Psi_{\text{AF}}\rangle = J_s J|\text{AF+Backflow}\rangle$. Notice that the variational energy for $n_h = 4$ and $|\Psi_{\text{AF}}\rangle$ is missing because the system is an open shell.

Wave functions	$E(n_h=0)$	$E(n_h = 4)$	$E(n_h = 8)$
$ \Psi_{\text{BCS+AF}}\rangle$	-0.52165(2)	-0.55880(4)	-0.59788(5)
$ \Psi_{\text{SL}}\rangle$	-0.5156(1)	-0.5618(1)	-0.6075(1)
$ \Psi_{\text{AF}}\rangle$	-0.52344(3)		-0.60687(4)

Table 2.4: Fixed node energies for the Hubbard model on the unfrustrated square lattice with 162 lattice sites and the number of holes $n_h = 0, 4, 8$. Three different wave functions are taken as the guiding ones: a combination of BCS pairing and antiferromagnetic order parameter $|\Psi_{\text{BCS+AF}}\rangle$, a spin liquid one with backflow correlations $|\Psi_{\text{SL}}\rangle = J|\text{BCS+Backflow}\rangle$ and an antiferromagnetic one with backflow correlations $|\Psi_{\text{AF}}\rangle = J_s J|\text{AF+Backflow}\rangle$. Notice that the Fixed Node energy for $n_h = 4$ and $|\Psi_{\text{AF}}\rangle$ is missing because the system is an open shell.

In Table (2.3) we show a comparison between the variational energies of three different wave functions, $|\Psi_{\text{BCS+AF}}\rangle$, $|\Psi_{\text{SL}}\rangle = J|\text{BCS+Backflow}\rangle$ and $|\Psi_{\text{AF}}\rangle = J_s J|\text{AF+Backflow}\rangle$, at half-filling and at low doping, for the Hubbard model on the unfrustrated square lattice. The number of lattice sites is $L = 162$, while the number of holes is $n_h = 0, 4, 8$. We notice that for every value of doping there is at least one wave function with backflow correlations that is more accurate in the variational energy than the one constructed with the Pfaffian. Moreover, it seems that antiferromagnetic correlations are dominant almost up to $n_h = 8$.

In order to conclude this section we show also a comparison between the Fixed Node energies using the three aforementioned wave functions as the guiding ones (see Table (2.4)). Data are shown for the same lattice size and the same dopings. Also in this case there is at least

one guiding wave function with backflow correlations, bringing a Fixed Node energy more accurate than the one we can get using, as a guiding wave function, the one constructed with the Pfaffian. Moreover, the comparison between Fixed Node energies suggests that superconductive pairing may be important already for $n_h = 8$, where the Fixed Node energy obtained using $|\Psi_{\text{SL}}\rangle$ is already a bit lower than the one obtained using $|\Psi_{\text{AF}}\rangle$.

Finally, we would like to mention a recent accurate wave function [72] that has been proposed for the ground state of the Hubbard model, even if we do not provide numerical comparisons:

$$|\Psi\rangle = e^{-h\hat{T}} e^{-g\hat{D}} |\Psi_0\rangle, \quad (2.104)$$

where $|\Psi_0\rangle$ is a mean-field ground state with either superconductivity or antiferromagnetic order parameter, h and g are variational parameters and the operators \hat{T} and \hat{D} are defined as:

$$\hat{T} = \sum_{\langle i,j \rangle, \sigma} c_{i,\sigma}^\dagger c_{j,\sigma} \quad \hat{D} = \sum_i n_{i,\uparrow} n_{i,\downarrow}. \quad (2.105)$$

This wave function has been applied on the unfrustrated square lattice, in presence of doping, and results has been presented for the antiferromagnetic state at half-filling and for the superconducting phase away from half-filling. However, this technique is difficult to implement for large values of the electron-electron repulsion U and for large clusters, because the Hubbard-Stratonovich decomposition of the terms $n_{i,\uparrow} n_{i,\downarrow}$ leads to strong fluctuations in the variational energy.

Chapter 3

The square lattice

The Hubbard model on the square lattice with nearest and next-nearest neighbour couplings, t and t' (see Fig. (3.1)), has been widely studied by many authors with different numerical techniques and contradictory outcomes. Indeed, it represents a simple prototype for frustrated electronic materials: in presence of a next-neighbour hopping t' , there is no more a perfect nesting condition that, in the unfrustrated case, leads to antiferromagnetic order for any finite U .

The first numerical study is due to Lin and Hirsch [73], using an auxiliary-field Monte Carlo approach [74]. They found the existence of a critical U_c for the appearance of antiferromagnetism at finite t' , for the half-filled case in presence of frustration. Their simulations showed also that antiferromagnetism decreases drastically as one moves away from half filling. More recent studies on the square lattice at half-filling were performed by Imada and coworkers [75, 76, 77], who, by using the Path Integral Renormalization Group approach [78], obtained the phase diagram shown in Fig. (3.2). The main result is the presence of an intermediate gapless paramagnetic insulator (denoted by NMI), which is sandwiched between the metallic phase, stable at small U/t ,

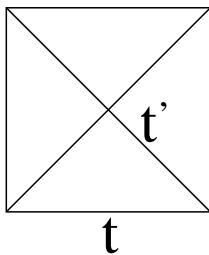


Figure 3.1: Square lattice with nearest neighbour hopping t and next-nearest neighbour hopping t' .

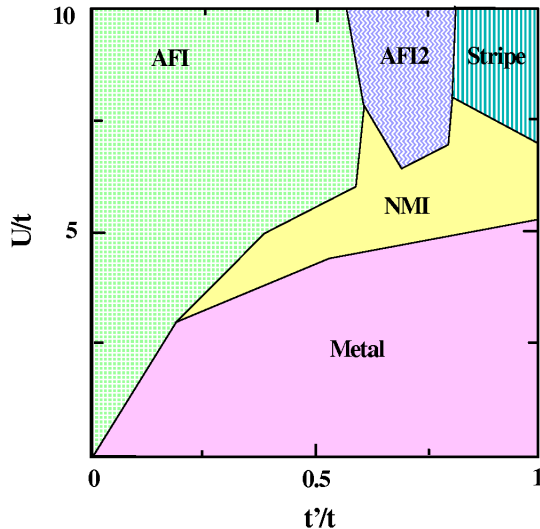


Figure 3.2: Phase diagram of the Hubbard model on the square lattice with nearest and next-nearest neighbour coupling, at half-filling, according to Ref. [77]. The different phases are explained in the text. Maximum lattice size is 10×10

and different magnetic insulators, which appear at strong coupling. The state denoted by AFI has antiferromagnetic Neel order, namely with pitch vector $\mathbf{Q} = (\pi, \pi)$; the phase referred as Stripe, has another kind of magnetic order with two equivalent pitch vectors $\mathbf{Q} = (\pi, 0)$ or $\mathbf{Q} = (0, \pi)$. Furthermore, they found an additional ordered phase, denoted by AFI2, with pitch vector $\mathbf{Q} = (\pi, \pi/2)$.

Another recent study of the Hubbard model on the frustrated square lattice is based on a Variational Monte Carlo approach, using the Jastrow factor introduced by Shiba (see Eq. (2.31)), to improve the variational wave function [79]. The results are shown in Fig. (3.3). The phase called P-I is a paramagnetic insulator that arises from a metallic state, at large enough t'/t , by increasing the value of U/t . The transition is claimed to be first-order. The phase labelled as AF-I is a standard antiferromagnetic phase with Neel order and there is the appearance of a robust superconducting phase, denoted by SC, for moderate values of U/t (i.e., $U/t \sim 6$) and t'/t (i.e., $0.2 \lesssim t'/t \lesssim 0.35$). This SC phase is accompanied by rather enhanced short-range antiferromagnetic spin correlations.

Finally, we would like to mention the work by Tremblay and coworkers [80], which is based upon a Variational Cluster Approximation

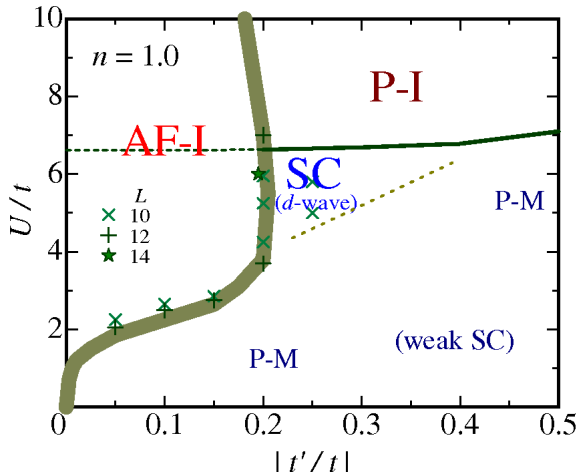


Figure 3.3: Phase diagram of the Hubbard model over the square lattice with nearest and next-nearest neighbour coupling, at half-filling, according to Ref. [79]. The various phases are described in the text. Lattice size lies between 6×6 and 18×18 .

(VCA) [81]. Their results are shown in Fig. (3.4). The phase called SC is a superconducting state with a finite superconductive order parameter, the phase labelled as (π, π) is the standard antiferromagnetic insulator with Neel order, while there is in addition the appearance of a region of homogeneous coexistence of the magnetic and superconducting phases (the blue area on the figure). The intermediate region at $t'/t \sim 0.8$ denotes a spin liquid and the phase indicated with $(\pi, 0)$ is the collinear magnetic phase with pitch vector $\mathbf{Q} = (\pi, 0)$. All the transitions are first-order.

Remarkably, all the previous approaches give very different results for the ground-state properties of this simple correlated model. In fact, the discrepancies arise both from fixing the boundaries of settled phases (like for instance the insulating one with Neel antiferromagnetic order) and from placing novel phases (like the non-magnetic insulating one, which is expected for large frustrating ratios t'/t and intermediate/large Coulomb repulsions). Finally, also the possibility to have superconductivity at small values of U/t is controversial.

In the following we will show our phase diagram obtained using Variational Monte Carlo, by inserting backflow correlations into the trial wave functions [30]. We will compare our results with the other ones presented in this introduction; in this respect we will also apply Green's Function Monte Carlo to confirm the variational results.

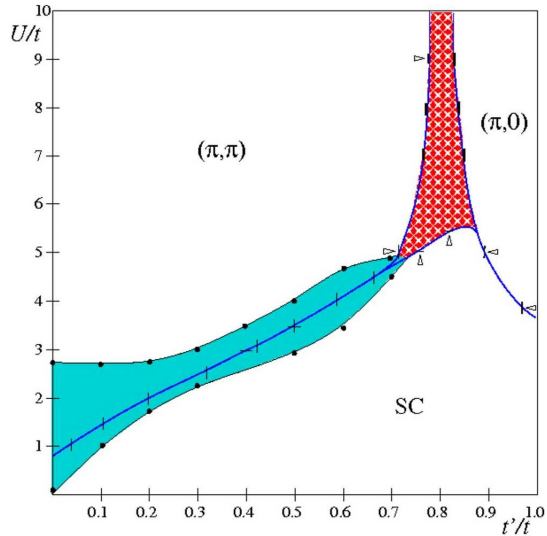


Figure 3.4: Phase diagram of the Hubbard model over the square lattice with nearest and next-nearest neighbour coupling, at half-filling, according to Ref. [80]. The various phases are described in the text. Clusters used in VCA are of four, six and eight sites.

3.1 Connection with the Heisenberg model

As already mentioned in the previous chapter, there is a sizeable difference between the energies of the spin-liquid state in the Hubbard model for large values of U/t and the energy obtained within the Heisenberg model using the fully projected wave function (see Eq. (2.22)), especially for the frustrated case. We anticipated that, by using backflow correlations, we are able to fix this problem. Let us start considering the unfrustrated case $t' = 0$, shown in Fig. (3.5). We notice that the variational energies for the spin liquid state in the Hubbard model, $|\Psi_{\text{SL}}\rangle = J|\text{BCS}\rangle$, are strongly improved by means of backflow correlations and, mainly, they extrapolate correctly to the variational energy of the projected BCS state in the Heisenberg model. On the contrary, the state with Neel antiferromagnetic order and the spin Jastrow factor, i.e., $|\Psi_{\text{AF}}\rangle = J_s J |\text{AF}\rangle$, (see Eq. (2.21) and Fig. (2.2)) is already very accurate to describe the Hubbard model on the square lattice with $t' = 0$. The effect of backflow correlations in this case is almost irrelevant, see Fig. (3.5).

As shown in Fig. (3.6), when we consider the frustrated case with $t'/t = 0.7$, the role of backflow correlations in improving the accuracy of the spin-liquid state for the Hubbard model is even more evident.

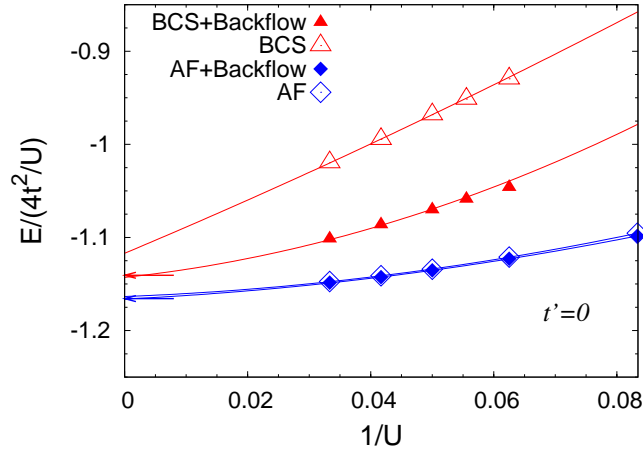


Figure 3.5: Variational energies per site (in unit of $J = 4t^2/U$) for the BCS state with a Jastrow factor, with and without backflow correlations, for $t' = 0$ and 98 sites. The results for the wave function with antiferromagnetic order and no BCS pairing are also shown. Arrows indicate the variational results obtained by applying the full Gutzwiller projector to the mean-field states for the corresponding Heisenberg model.

Also in this case, the correct matching with the variational energy of the $|\text{RVB}\rangle$ state in the Heisenberg model is possible only within backflow correlations. Furthermore, in the frustrated case, we need backflow correlations also to guarantee a correct matching between the variational energies of the antiferromagnetic state in the Hubbard model, for increasing U , and the energy obtained in the Heisenberg model with the magnetic state. However, the most important result that we can observe in Fig. (3.6) is that, *only* thanks to backflow correlations, the energy of the spin-liquid solution becomes lower than the energy of the antiferromagnetic one, in the frustrated regime. This fact will bring the opening of a spin liquid region in the phase diagram of the Hubbard model on the square lattice.

3.2 The variational phase diagram

In order to draw the ground-state phase diagram of the $t - t'$ Hubbard model, we consider three different wave functions, all with backflow correlations: Two antiferromagnetic states $|\Psi_{\text{AF}}\rangle$ with pitch vectors $\mathbf{Q} = (\pi, \pi)$ (the Neel one) and $\mathbf{Q} = (\pi, 0)$ (the collinear one), relevant for small and large t'/t , and the nonmagnetic state $|\Psi_{\text{SL}}\rangle$. The

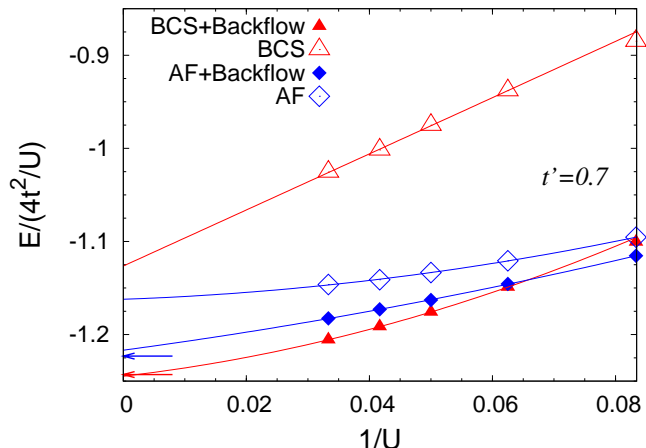


Figure 3.6: Variational energies per site (in unit of $J = 4t^2/U$) for the BCS state with a Jastrow factor, with and without backflow correlations, for $t' = 0.7$ and 98 sites. The results for the wave function with antiferromagnetic order and no BCS pairing are also shown. Arrows indicate the variational results obtained by applying the full Gutzwiller projector to the mean-field states for the corresponding Heisenberg model.

variational phase diagram is reported in Fig. (3.7). The important outcome is that, without backflow terms, the energies of the spin-liquid wave function are *always* higher than those of the magnetically ordered states for any value of the frustration t'/t . Instead, by inserting backflow correlations, a spin-liquid phase can be stabilized at large enough U/t and frustration. For example, in Fig. (3.8), we show the variational energies for the three aforementioned wave functions with and without backflow correlations, at $U/t = 16$. Here, the presence of these many-body correlations allows to have a magnetically disordered phase for intermediate values of the frustrating hopping, namely for $0.67 \lesssim t'/t \lesssim 0.77$.

In order to study the metal-insulator transition, we look at the static density-density correlations $N(q) = \langle n_{-q} n_q \rangle$ (where n_q is the Fourier transform of the local density n_i). Indeed $N(q)$ shows a linear behaviour for $|q| \rightarrow 0$ in the metallic phase and a quadratic behaviour in the insulating region. This property is related to the existence (or not) of a gap between the ground state and the first excited one; a detailed derivation can be found in Ref. [82]. For small Coulomb repulsion and finite t'/t , $N(q)$ has the linear behaviour for $|q| \rightarrow 0$, typical of a conducting phase. A very small superconducting parameter with $d_{x^2-y^2}$ symmetry can be stabilized, suggesting that long-range pairing

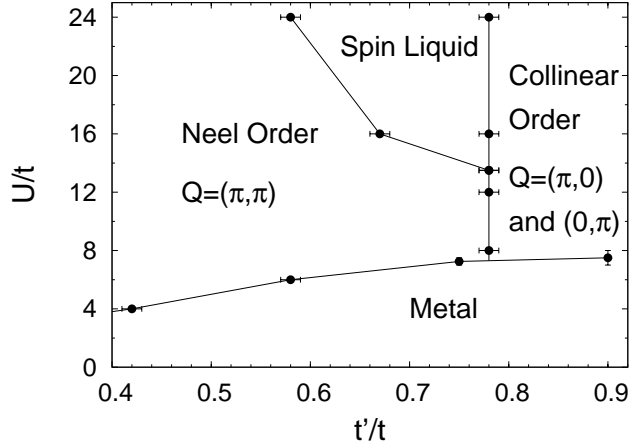


Figure 3.7: Variational phase diagram of the frustrated $t-t'$ Hubbard model, as obtained by comparing the variational energies of different wave functions, all with backflow correlations. Data refer to a 98-site lattice, however the phase diagram is only slightly modified for larger sizes. (We considered clusters of 50, 98 and 162 sites).

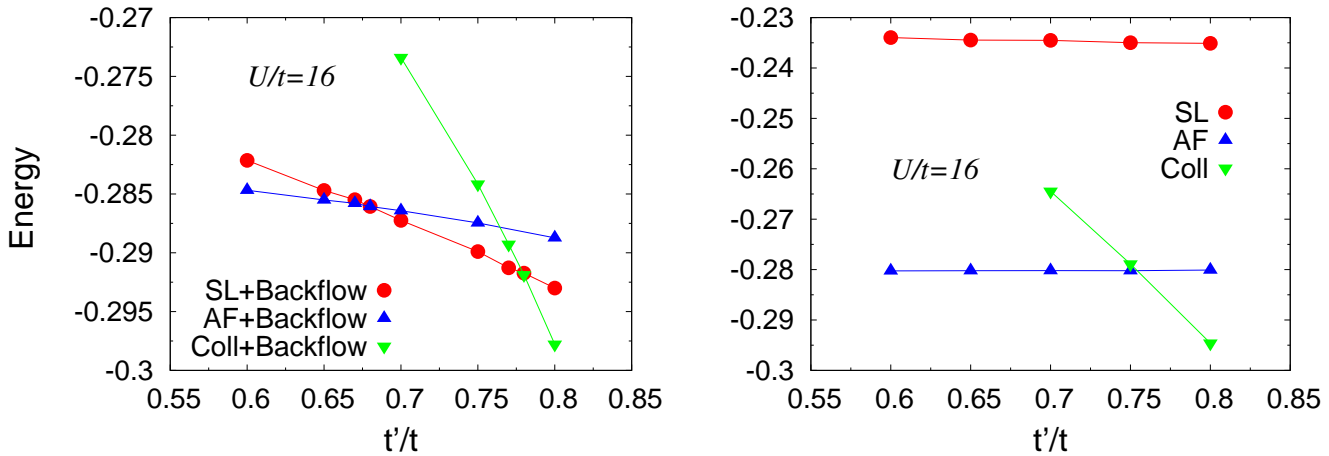


Figure 3.8: Variational energies for three different wave functions on the frustrated square lattice with and without backflow correlations (left and right panel, respectively). Red dots denote the energies of the spin-liquid wave function, blue up triangles denote the energies of the magnetic state with Neel order, while green down triangles denote the energies of the magnetic state with collinear order. Data are shown for $U/t = 16$ and 98 lattice sites.

U/t	Δ_{BCS} with backflow	Δ_{BCS} without backflow
7	0.042(1)	0.305(1)
6	0.031(1)	0.145(1)
4	0.012(1)	0.039(1)
2	0.002(1)	0.021(1)

Table 3.1: BCS pairing Δ_{BCS} , for various U/t in the metallic region at $t'/t = 0.75$. Lattice sites are 98. Data in the second column are obtained when the spin-liquid wave function $|\Psi_{\text{SL}}\rangle$ is improved by means of backflow correlations, while data in the third column refer to a spin-liquid wave function without backflow correlations.

correlations, if any, are tiny. In this respect, we compare in Table (3.1) the optimized Δ_{BCS} , when the spin-liquid wave function $|\Psi_{\text{SL}}\rangle$ contains or not backflow correlations, for various U/t at $t'/t = 0.75$. Data show that when accuracy increases, by means of backflow correlations, BCS pairing is reduced by an order of magnitude.

By increasing U/t , a metal-insulator transition is found and $N(q)$ acquires a quadratic behaviour in the insulating phase, indicating a vanishing compressibility. In Fig. (3.9) we show the variational results for $N(q)$ as a function of U/t for $t'/t = 0.75$. The insulator just above the transition is magnetically ordered and the variational wave function has a large Δ_{AF} ; the transition is likely to be first order. For example, in Fig (3.10) we plot the parameter Δ_{AF} across the metal-insulator transition for a fixed value of U/t and varying the ratio t'/t . It has a jump from the insulating to the metallic state, as expected for a first order transition. Moreover, there is some hysteresis around the transition point and it is possible to stabilize, inside the insulating region, a metallic solution, with energy higher than the insulating one.

In this respect, we would like to stress that, within our variational approach, a finite Δ_{AF} can be stabilized down to very small values of U/t in the unfrustrated regime, $t' = 0$. Indeed, if we compare the variational energies of two wave functions, one with a finite, optimized mean-field antiferromagnetic parameter Δ_{AF} and the other one without Δ_{AF} , we obtain that the former wave function has always a lower variational energy, down to $U/t = 1$. Results are shown in Table (3.2). Of course, for lower values of U/t , the correlation length may be larger than the linear size of the cluster and spurious metallic effects are found.

Going back to the frustrated regime with $t'/t \sim 0.7$, we notice from the phase diagram that, by further increasing U/t , there is a second

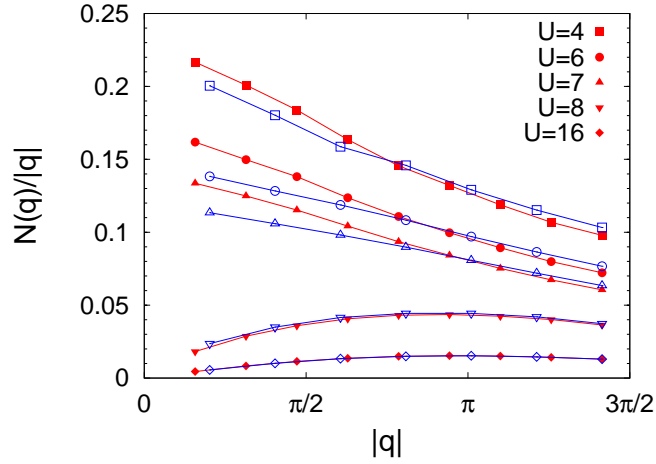


Figure 3.9: Variational results for $N(q)$ divided by $|q|$ for 98 (empty symbols) and 162 (full symbols) lattice sites and $t'/t = 0.75$. The metal-insulator transition takes place between $U/t = 7$ and $U/t = 8$, where $N(q)$ changes from a linear to a quadratic behaviour for $|q| \rightarrow 0$.

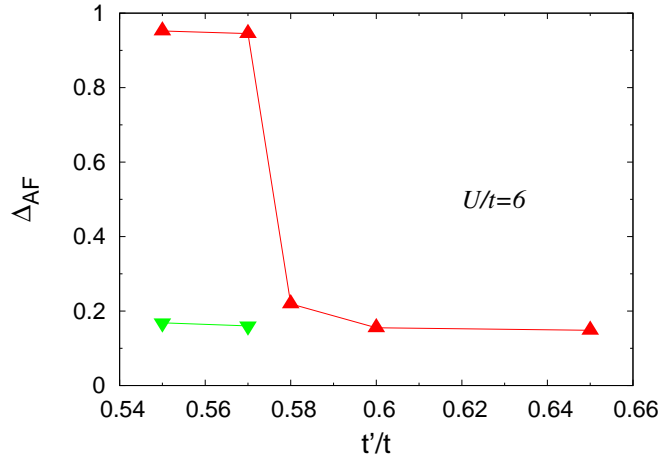


Figure 3.10: Red triangles denote the Δ_{AF} parameter across the metal-insulator transition for $U/t = 6$. Green triangles denote the values of Δ_{AF} for the metallic solution, with higher energy, that can be stabilized inside the insulating region. Lattice sites are 98.

U/t	$E(\Delta_{\text{AF}} \neq 0)$	$E(\Delta_{\text{AF}} = 0)$
4	-0.86041(1)	-0.83914(1)
2	-1.19584(1)	-1.19534(1)
1	-1.41031(1)	-1.41025(1)

Table 3.2: Variational energy at small U/t , in the unfrustrated case $t' = 0$ on a 98-site lattice, for two kinds of variational wave functions. The first one with a finite mean-field antiferromagnetic parameter Δ_{AF} and the second one without Δ_{AF} .

L	$\Delta_{d_{xy}}$
26	-0.077(1)
50	-0.011(1)
82	0.001(1)

Table 3.3: Optimized mean-field BCS parameter with d_{xy} symmetry, for increasing lattice size L , at $U/t = 20$ and $t'/t = 0.7$.

transition to a disordered insulator. Indeed, for $U/t \gtrsim 14$, the energy of the BCS wave function becomes lower than the one of the antiferromagnetic state. In this respect, the key ingredient to have such an insulating behaviour is the presence of a long-range Jastrow term (see Eq. 2.26), which turns a BCS superconductor into a Mott insulator [20]. By further increasing U/t , the spin liquid phase may be connected with the one determined by Capriotti *et al.* [18], in the frustrated Heisenberg model on the square lattice. However, there is an important difference: in fact, the spin liquid found in Ref. [18] is described by a fully projected BCS state having a pairing with both $d_{x^2-y^2}$ symmetry ($\Delta_{\text{BCS}} \propto (\cos k_x - \cos k_y)$) and d_{xy} symmetry ($\Delta_{\text{BCS}} \propto \sin k_x \sin k_y$). This combination modifies the nodal surface of the electronic wave function allowing for better variational energies. Instead, in the Hubbard model, we are able to stabilize just the variational wave function with the $d_{x^2-y^2}$ symmetry, for every values of U/t . In all cases that have been analyzed, we found that the d_{xy} term is not stable in the thermodynamic limit, but converges to zero as the number of lattice sites L is increased. Data are shown in Table (3.3), for $U/t = 20$ and $t'/t = 0.7$. This result implies either that our variational wave function is still not so accurate in the limit of high electron-electron repulsion U/t , or, conversely, that a finite d_{xy} is just an artifact of the Heisenberg model and it is immediately suppressed as soon as charge fluctuations are taken into account.

Our phase diagram is quite different with the other ones that we

Wave function	Energy($U/t = 20, t'/t = 0.7$)	Energy($U/t = 8, t'/t = 0.3$)
$J \text{BCS}\rangle$	-0.1950(1)	-0.4016(1)
$JJ_{\text{Shiba}} \text{BCS}\rangle$	-0.2061(1)	-0.4180(1)
$J \text{BCS} + \text{Backflow}\rangle$	-0.23516(4)	-0.48793(6)
$J_s J \text{AF} + \text{Backflow}\rangle$	-0.23257(3)	-0.52219(1)

Table 3.4: Variational energies for three kinds of wave function simulating the spin-liquid phase and for the best wave function simulating the anti-ferromagnetic state with Neel order. Data are shown for two points of the phase diagram. Lattice sites are 98.

have shown at the beginning of the chapter, especially because in our phase diagram there is not a spin liquid at intermediate values of U/t , emerging directly from the metallic state. On the contrary, our calculations indicate the possibility to have a direct (first order) transition between two magnetic states (see Fig. 3.7). We can make a direct comparison of our energies with the ones obtained by Ref. [79] using a Variational Monte Carlo approach, where the trial wave functions are improved by means of the Jastrow factor introduced by Shiba (see Eq. (2.31)). We show, in Table (3.4), the variational energy of the simple spin-liquid state $|\Psi_{\text{SL}}\rangle = J|\text{BCS}\rangle$, together with the improved variational energies, obtained by adding the Shiba Jastrow factor or backflow correlations to the spin-liquid wave function. We notice that the energy obtained by means of backflow correlations is always much lower than the one obtained with the additional Jastrow factor. Moreover, since the point at $U/t = 8$ and $t'/t = 0.3$ is magnetically ordered according to our simulations, while it is in a spin-liquid phase according to Fig. (3.3), we compare also the variational energy of the magnetically ordered state, with backflow correlations (that is our best variational energy), with the energy of the spin liquid state, improved by means of the Shiba Jastrow factor (that is the best energy according to Ref. [79]). We can observe that the variational energy of the magnetic wave function is much lower than the one corresponding to the spin-liquid solution. All these comparisons suggest that backflow correlations are more accurate than the Shiba Jastrow factor, giving a more reliable phase diagram.

The other two phase diagrams, shown in Fig. (3.2) and in Fig. (3.4), are obtained with different numerical techniques and so a direct comparison among variational energies is no longer possible. Then, in order to make our diagram more robust, we have applied a Green's Function Monte Carlo (GFMC) approach, as explained in the following section.

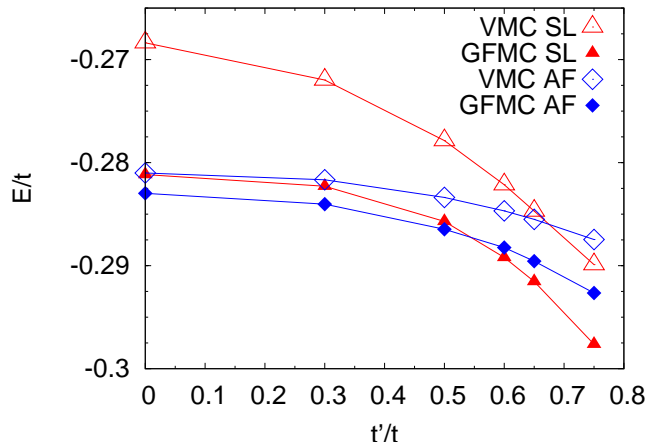


Figure 3.11: Comparison between the variational (VMC) energies per site (with backflow correlations) and the GFMC ones, within the Fixed Node approximation. The VMC wave functions are the guiding ones for the corresponding GFMC iteration. Data are shown for $U/t = 16$ and 98 sites.

3.3 Green's Function Monte Carlo on the square lattice

First of all, we have compared the variational energies and the GFMC ones, obtained using the variational wave functions as the guiding ones in the Fixed Node approximation. For example, in Fig. (3.11), we show the variational energies per site (with backflow correlations) and the GFMC ones for $U/t = 16$ on a 98-site lattice. The small energy difference between the pure variational and the GFMC energies demonstrates the accuracy of the backflow states. Notice that $|\Psi_{AF}\rangle$ and $|\Psi_{SL}\rangle$ have different nodal surfaces, implying different GFMC energies, within the Fixed Node approximation. In fact, as explained in the previous chapter, the variational wave functions are used as guiding functions in the Fixed Node approximation, determining the signs of the Fixed Node ground state, obtained after the iterative application of the Green's function.

Furthermore, in order to verify the magnetic properties obtained within the variational approach, we can consider the static spin-spin correlations $S(q) = \langle S_q^z S_{-q}^z \rangle$. Indeed, a long-range magnetic order at some pitch vector \mathbf{Q} implies a diverging structure factor $S(\mathbf{Q}) \sim N$. We have calculated the static spin-spin correlations over the Fixed Node ground state. Although the Fixed Node approach may break the

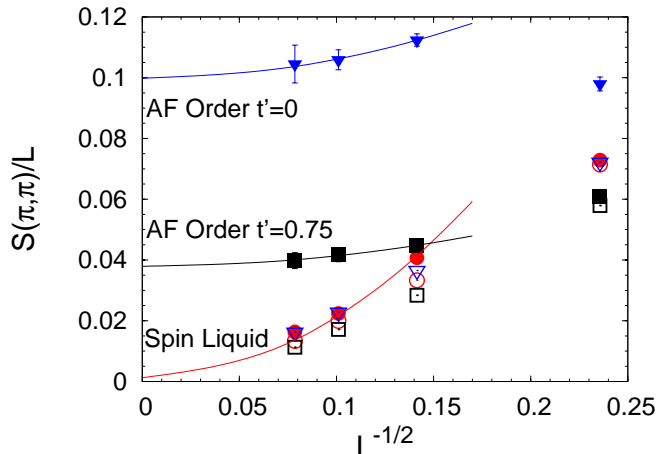


Figure 3.12: Variational (empty symbols) and Fixed Node (full symbols) results for $S(\pi, \pi)$ divided by the number of lattice sites $L = 18, 50, 98, 162$. All the calculations have been done by using the projected BCS wave function; $U/t = 16$ and $t'/t = 0$ (triangles), $U/t = 24$ and $t'/t = 0.7$ (circles) and $U/t = 8$ and $t'/t = 0.75$ (squares). Lines are guides to the eye.

SU(2) spin symmetry, favoring a spin alignment along the z axis, $S(q)$ is particularly simple to evaluate within this approach [17] and it gives important insights into the magnetic properties of the ground state. In Fig. (3.12), we report the comparison between the variational and the FN results by considering the non-magnetic state $|\Psi_{\text{SL}}\rangle$. Remarkably, in the unfrustrated case, where antiferromagnetic order is expected, the FN approach is able to increase spin-spin correlations at $\mathbf{Q} = (\pi, \pi)$, even by considering the nonmagnetic wave function to fix the nodes. A finite value of the magnetization is also plausible in the insulating region just above the metallic phase at strong frustration (i.e. $t'/t \sim 0.75$), confirming the variational calculations. On the contrary, by increasing the electron correlation, the Fixed Node results change only slightly the variational value of $S(\pi, \pi)$, indicating the stability of the disordered state. Fixed Node results confirm that a spin liquid region can be stabilized only at large enough U/t , while the insulator close to the metallic region is magnetically ordered. This is quite in contrast with the previously shown phase diagrams, where the spin-liquid phase emerges directly from a conducting regime, by increasing U/t .

In conclusion, we have presented the variational phase diagram of the half-filled Hubbard model on the frustrated $t - t'$ square lattice, that is a simple prototype for frustrated electronic materials. We are able to recover a spin-liquid region in the strong coupling regime, in

addition to the metal-insulator transition and to two magnetically ordered insulators. In order to confirm the magnetic properties of our variational wave function, we have applied the Green's Function Monte Carlo approach. Finally, we have compared our phase diagram with the other ones existing in literature, showing important evidence for the accuracy of our results.

Chapter 4

The triangular lattice

Here, we discuss the Hubbard model on the anisotropic triangular lattice, in which the ratio between the hoppings t and t' (see Fig. (4.1)) is bigger or smaller than one. The combination of geometrically frustrated magnetic interactions and low dimensionality, in such a lattice, may open the route to a variety of phases: magnetic ordering with commensurate or incommensurate (spiral) order or spin liquids. In our work, we do not address directly the presence of spiral order in the lattice, since it is hard to be detected on finite clusters of reasonable size. However, a fingerprint of spiral order can still be detected by Green's Function Monte Carlo, with the appearance of incommensurate peaks in the static spin-spin correlations $S(q)$, even if the guiding wave function does not account for them [83].

In recent years, several experiments have been performed on compounds described by a quasi-2D triangular lattice, showing the first experimental evidences of spin-liquid phases. In 2001 Coldea and coworkers [11] performed nuclear scattering measurements on the compound

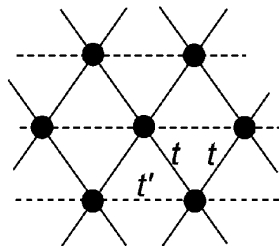


Figure 4.1: Sketch of the anisotropic triangular lattice. t and t' indicate the hopping integrals along the solid-line bonds and the dashed-line bonds, respectively.

Cs_2CuCl_4 , formed by weakly-interacting 2D layers with an anisotropic triangular crystal structure ($J'/J \sim 3$)¹. Their data are consistent with a spin-liquid state at temperatures higher than 0.62 K, whereas at lower temperatures the 3D coupling induces long-range magnetic order. Moreover, they showed that, suppressing the inter-layer coupling by means of a magnetic field, the spin liquid phase can be stabilized down to zero temperature. Other experiments were performed by Kanoda and coworkers [9, 10] on $k - (\text{ET})_2\text{Cu}_2(\text{CN})_3$, an organic salt made of 2D layers with a slightly anisotropic triangular lattice ($t'/t = 1.06$). They observed a spin-liquid phase at ambient pressure, without any evidence of magnetic ordering down to 32 mK, well below the estimated exchange constant of $J \sim 250\text{K}$. This behaviour is in contrast with another salt $k - (\text{ET})_2\text{Cu}[\text{N}(\text{CN})_2]\text{Cl}$, with $t'/t \sim 0.7$, that shows a clear antiferromagnetic transition at $T = 27\text{ K}$. Moreover, in a very recent experiment [84], it was shown that the compound $k - (\text{ET})_2\text{Cu}_2(\text{CN})_3$ exhibits a linear temperature-dependent contribution to the heat capacity. This feature is strongly unusual for an insulating material, resembling much more the behaviour of a one-dimensional antiferromagnetic spin system or of a metal, with continuous excitations around the Fermi surface.

In this thesis, we distinguish, to our convenience, three different regimes in a triangular lattice, according to the ratio t/t' . We do not treat the case $t' \sim t$, when the lattice is isotropic. This regime is believed to show a classical commensurate ordering in the insulating phase. However, in a recent paper [85], it has been suggested that a spin-liquid phase may be present, close to the metal-insulator transition. Furthermore, the presence of incommensurate ordering in the metallic phase has been proposed in Ref. [86], on the basis of a mean-field approach.

In the first section of this chapter, we address the regime $t > t'$, where the lattice can be described as a set of squares, formed by the bonds with hopping t , that are frustrated by the bonds with hopping t' ; when $t' \rightarrow 0$ we approach the unfrustrated square lattice. In this case, by increasing U/t , after the metal-insulator transition, the system is found to be in a magnetically ordered phase. The standard Neel order on the squares formed by the bonds t is recovered. We compare our results with other numerical studies performed by Refs. [87] and [88].

In the second section of this chapter, we deal with the case $t' > t$, in which the lattice can be seen as a set of chains, along which the electrons hop with an amplitude t' , connected by the bonds with hopping

¹Since this compound is strongly interacting, it has been described by the Heisenberg model, using the spin coupling J , instead of the hopping t .

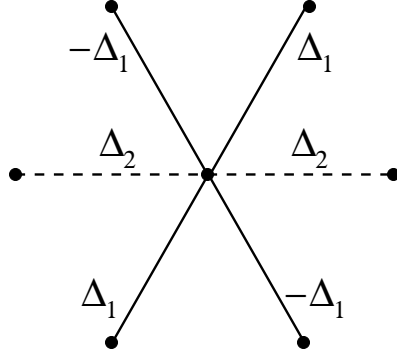


Figure 4.2: Symmetry of the BCS pairings along the triangular lattice, when $t > t'$.

t ; when $t \rightarrow 0$ we approach a set of 1D decoupled chains. We identify the metal-insulator transition and, mainly, we observe signatures that the insulator is in a spin-liquid regime with one-dimensional features. This behaviour is favored by backflow correlations. A one-dimensional character for the ground state has been recently proposed also for the Heisenberg model [89, 90]. Moreover, the nature of our best state is compatible with a projected Fermi sea, since no long-range magnetic order parameter or superconductive pairing may be stabilized. According to Refs. [91, 92], a spin liquid described by a projected Fermi gas has a stable spinon Fermi surface, with low-lying spin excitations², that may lead to the linear temperature-dependent behaviour in the heat capacity, observed in a recent experiment [84].

4.1 The anisotropic triangular lattice with $t > t'$

We present, in this section, the anisotropic triangular lattice with $t > t'$, focusing on the case $t'/t = 0.7$. We start considering only the spin-liquid solution $|\Psi_{\text{SL}}\rangle = J|\text{BCS}\rangle$, including also backflow correlations. The symmetry of the BCS pairing Δ_1 has been chosen to be d -wave with $d_{x^2-y^2}$ symmetry, on the bonds connected by the hoppings t , between nearest-neighbour sites, as shown in Fig. (4.2). An additional small s -wave parameter Δ_2 can be stabilized along the bonds connected by the hoppings t' . This choice connects smoothly with the limit $t' \rightarrow 0$ in which the $d_{x^2-y^2}$ pairing function of the unfrustrated square lattice is recovered. Moreover, the symmetry of the superconductive pairing in the Hubbard model was studied in a recent paper

²Charge excitations are gapped because we are in the insulating regime.

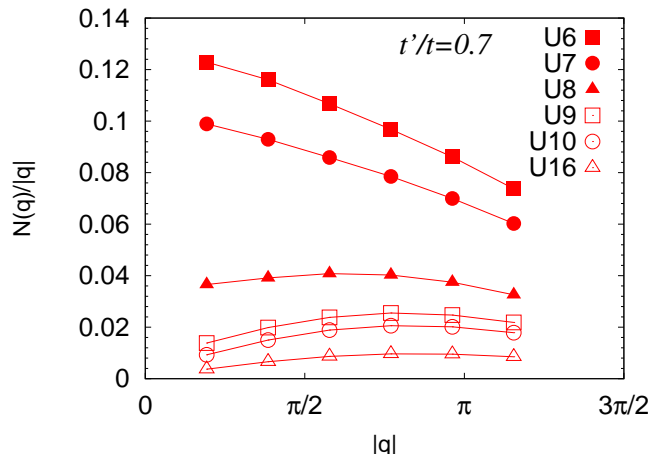


Figure 4.3: Variational results for $N(q)$ divided by $|q|$ for a 144-site lattice at $t'/t = 0.7$, using $|\Psi_{\text{SL}}\rangle$ as a trial wave function. The metal-insulator transition takes place between $U/t = 8$ and $U/t = 9$, where $N(q)$ changes from a linear to a quadratic behaviour for $|q| \rightarrow 0$.

[93], by means of the Gutzwiller approximation, observing that the $d_{x^2-y^2}$ symmetry is stable from $t' = 0$ to $t'/t \sim 0.9$. In addition to Δ_{BCS} , we optimize, in the trial wave function, also the hopping parameter t'_{wf} along the dashed-line bonds of Fig. (4.2).

We identify a metal-insulator transition, by looking at the density-density correlation factor $N(q) = \langle n_{-q} n_q \rangle$. In Fig. (4.3), $N(q)$ changes from a linear behaviour for $|q| \rightarrow 0$, typical of a conducting phase, to a quadratic behaviour in the insulating regime at $U/t \gtrsim 8$. The BCS pairing has a jump at a critical U below the metal-insulator transition, suggesting that a superconductive region may exist, sandwiched between the metallic and the insulating ones (see Fig. (4.4)).

These results are quite in agreement with the ones obtained in Ref. [87], even if the metal-insulator transition is slightly shifted. However, when we take into account also the magnetic trial wave function $|\Psi_{\text{AF}}\rangle = J_s J |\text{AF}\rangle$, with backflow correlations, the results are quite different. The magnetic order parameter is chosen to be the Neel anti-ferromagnetic one on the squares formed by the bonds with hopping t (see Fig. (4.5)). Comparing the variational results obtained with the spin-liquid wave function with the ones obtained by means of $|\Psi_{\text{AF}}\rangle$, we observe that the metal-insulator transition is shifted to lower values of U/t and that the insulator is magnetically ordered, for every value of U/t , above the metal-insulator transition. Indeed, as shown in Fig. (4.6), for $U/t \lesssim 6.5$ $|\Psi_{\text{SL}}\rangle$ has lower energy than $|\Psi_{\text{AF}}\rangle$ and shows a

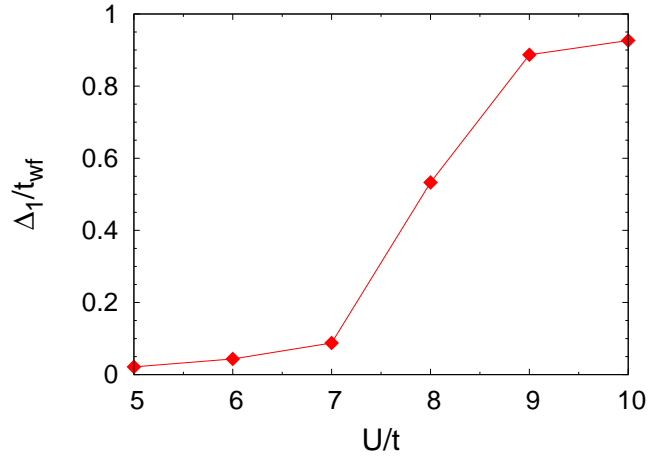


Figure 4.4: BCS pairing at increasing U/t on a triangular lattice with $t'/t = 0.7$ and 144 sites.

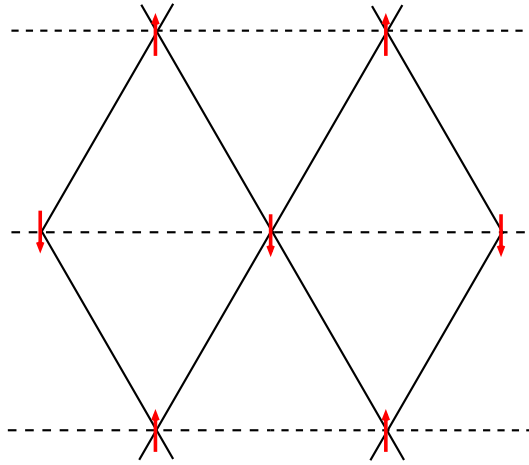


Figure 4.5: Magnetic order relevant on the anisotropic triangular lattice when $t > t'$. Spins are Neel antiferromagnetically ordered on the squares formed by the solid-line bonds.

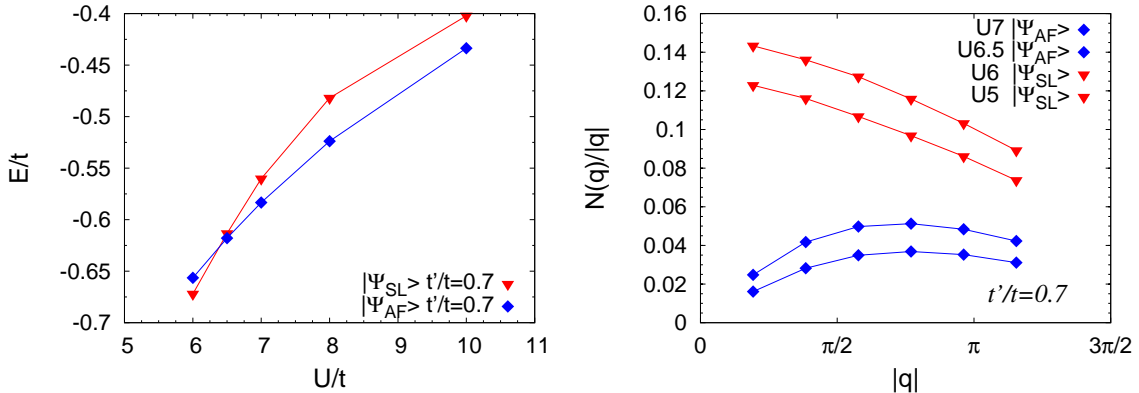


Figure 4.6: Left panel: Variational energy for increasing U/t in the triangular lattice with $t'/t = 0.7$ and 144 lattice sites. Two variational wave functions are compared: $|\Psi_{SL}\rangle$ and $|\Psi_{AF}\rangle$. Right panel: Variational results for $N(q)$ divided by $|q|$. Blue rhombi denote data for the $|\Psi_{AF}\rangle$ wave function, while red triangles denote data for the $|\Psi_{SL}\rangle$ wave function. The metal-insulator transition takes place between $U/t = 6$ and $U/t = 6.5$.

conducting behaviour, according to $N(q)$. Moreover, as shown in Fig. (4.4) $\Delta_1/t_{\text{wf}} \lesssim 0.05$, for $U/t \lesssim 6.5$, suggesting that long-range pairing correlations, if any, are tiny. On the contrary, for $U/t \gtrsim 6.5$, the system is in an insulating state with Neel antiferromagnetic order and a sizeable $\Delta_{AF}/t_{\text{wf}} \sim 1.2$.

In order to confirm the magnetic nature of the insulating state, we have performed a Fixed Node calculation, taking $|\Psi_{SL}\rangle$ as the guiding wave function, for four different lattice sizes. We have calculated the static spin-spin correlations $S(q) = \langle s_{-q}s_q \rangle$ for the point $(0, \frac{2\pi}{\sqrt{3}})$, that corresponds to Neel antiferromagnetic order along the bonds with hopping t . Results are shown in Fig. (4.7) and indicate that the FN approach is able to increase spin-spin correlations at $\mathbf{Q} = (0, \frac{2\pi}{\sqrt{3}})$, even when we consider the nonmagnetic wave function as an initial guess for the FN projection scheme. Indeed, $S(\mathbf{Q})/L$ tends, in the thermodynamic limit, to a value very close to the one obtained for the unfrustrated square lattice (see Fig. (3.12)). Moreover, it is important to stress that our Fixed Node calculations for $S(q)$ do not show evidence for any incommensurate peak, that would correspond to the formation of spiral magnetic order in the lattice.

Since our results are quite in contrast with the ones obtained by Liu and coworkers [87], we should compare our best variational energies in the magnetic insulating phase with their ones for the spin-liquid insulator [94]. They used a $J|\text{BCS}\rangle$ wave function, with in addition

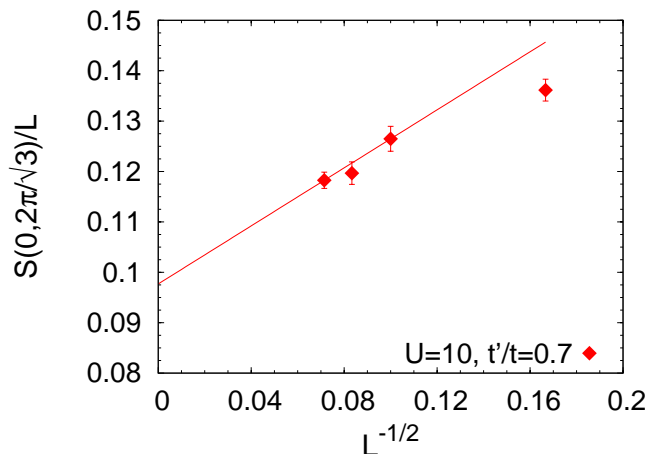


Figure 4.7: Fixed Node results for $S(0, \frac{2\pi}{\sqrt{3}})$ divided by the number of lattice sites $L = 36, 100, 144$ and 196 . All the calculations have been done by using the projected BCS wave function at $U/t = 10$ and $t'/t = 0.7$. The line is just a guide to the eye.

the Jastrow introduced by Shiba (see Eq. (2.31)) to correlate holons and doublons. Moreover, they allowed for an extension of the hopping range in the variational wave function, beyond nearest neighbours, that turned out to be crucial to stabilize the superconducting phase, appearing between the metallic and the insulating regions. In Table (4.1), we show that our energies, at $U/t = 8$ and 10 , which are obtained with a magnetic wave function, are much more accurate than the ones obtained with the Shiba Jastrow factor. Notice that the latter state would predict a spin liquid and a superconductor for $U/t = 10$ and 8 , respectively. Also in the metallic region ($U/t = 6$) our results are more accurate. On the contrary, our work is quite in agreement with a recent paper [88], where a variational Monte Carlo study is performed on the triangular lattice with $t' \leq t$. In this paper, a first-order metal-insulator transition towards a state with Neel antiferromagnetic order has been observed from $t' = 0$ to $t'/t \sim 0.9$. The trial state combines d -wave superconductive pairing with Neel order, through the Pfaffian ansatz. Remarkably, the authors noticed that their previous calculations, which predicted a robust superconductor and a nonmagnetic insulator [95], are modified by the stabilization of a magnetic phase. Finally, we remark that a commensurate magnetic ordering is in agreement with experimental data on $k - (\text{ET})_2\text{Cu}[\text{N}(\text{CN})_2]\text{Cl}$, see Ref. [9].

U/t	E/t (our work)	E/t ($JJ_{\text{Shiba}} \text{BCS}\rangle$)
6	-0.67204(4)	-0.628(1)
8	-0.52383(3)	-0.386(1)
10	-0.43365(3)	-0.285(1)

Table 4.1: Comparison between variational energies at increasing U/t . Left column: Our best variational energies in the magnetic insulating region ($U/t = 8, 10$) and in the metallic region ($U/t = 6$). Right column: Energies obtained by Liu and coworkers [94], for the same values of U/t , using a $JJ_{\text{Shiba}}|\text{BCS}\rangle$ wave function.

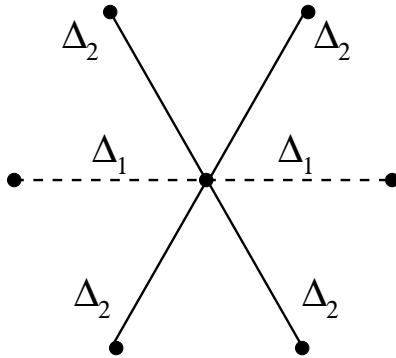


Figure 4.8: Symmetry of the BCS pairings along the triangular lattice, when $t' > t$.

4.2 The anisotropic triangular lattice with $t' > t$

The most interesting results on the triangular lattice appear in the regime $t' > t$, which may be relevant for the experiment described in Ref. [11] and can give some insight also on the experiments performed by Kanoda and coworkers. Indeed, the compound $k - (\text{ET})_2\text{Cu}_2(\text{CN})_3$ should lie in between the two regimes of the isotropic lattice and the anisotropic one with $t' > t$.

Our study is based on a Variational Monte Carlo approach, where we compare a spin-liquid solution $|\Psi_{\text{SL}}\rangle$ and an antiferromagnetic one $|\Psi_{\text{AF}}\rangle$, including also backflow correlations. According to a detailed variational study on the Heisenberg model [19] and to a study of the superconductive pairing in the Hubbard model, by means of the Gutzwiller approximation [93], we have chosen the nearest-neighbour BCS pairing to be an extended s -wave with a parameter Δ_1 along the bond t' and a parameter Δ_2 along the bonds with hopping t (see Fig. (4.8)). The antiferromagnetic order parameter couples the spins in a

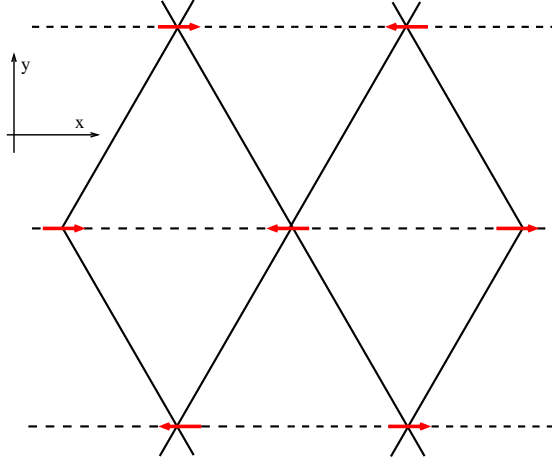


Figure 4.9: Collinear order on the triangular lattice with $t' > t$. Couplings along the chains are antiferromagnetic.

collinear way along the x direction, with antiferromagnetic order along the chains (see Fig. (4.9)). This kind of magnetic order has been also recently proposed as the ground state for the Heisenberg model, when $J' \gg J$ [96]. As already mentioned, the existence of incommensurate spin ordering in the lattice is very difficult to assess in finite clusters and it will not be considered here. However, the presence of spiral order can still be probed by Green's Function Monte Carlo, with the appearance of incommensurate peaks in the static spin-spin correlations $S(q)$. Together with the BCS pairing and the magnetic order parameter, we optimize in the trial wave function also the hopping parameter t_{wf} along the solid-line bonds of Fig (4.8).

A comparison among the variational energies, associated to the two wave functions, $|\Psi_{\text{SL}}\rangle$ and $|\Psi_{\text{AF}}\rangle$, can be seen in Fig. (4.10), for two values of the frustrating ratio $t/t' = 0.7$ and $t/t' = 0.5$. In the second case, we show also the density-density correlation factor $N(q) = \langle n_{-q} n_q \rangle$. For $U/t' \lesssim 4.5$ the system is in a metallic state, without superconducting behaviour. Indeed, the optimized parameters Δ_1 and Δ_2 in $|\Psi_{\text{SL}}\rangle$ tend to zero, suggesting that the presence of BCS pairing does not bring any improvement in the variational energy. On the other hand, for $U/t' \gtrsim 4.5$ the system is in an insulating regime, where the trial wave function $|\Psi_{\text{AF}}\rangle$ gives an energy more accurate than the one associated to the solution $|\Psi_{\text{SL}}\rangle$.

The presence of a finite Δ_{AF} in the variational wave function does not lead to a clear evidence of 2D magnetic order. In fact, by a more careful analysis of the variational parameters Δ_{AF} and t_{wf} , we notice

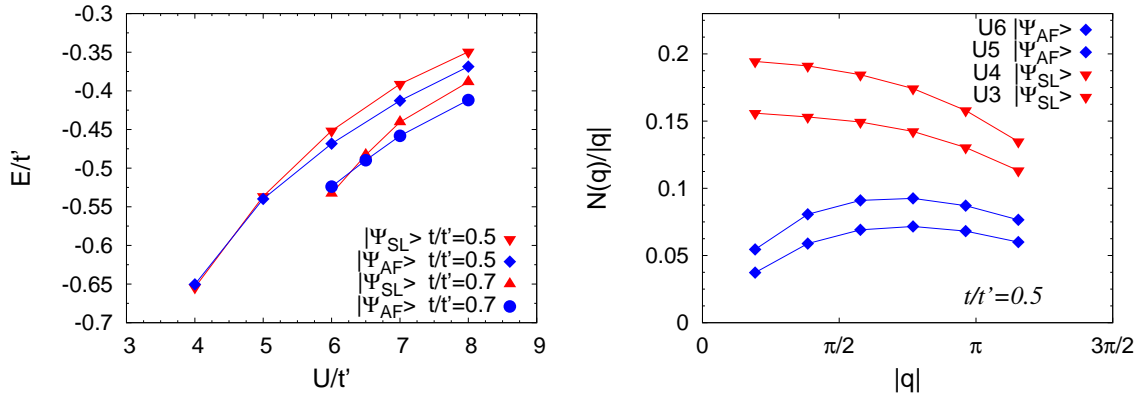


Figure 4.10: Left panel: Variational energy at increasing U/t' for a triangular lattice with $t/t' = 0.7$ and $t/t' = 0.5$, on a 144-site lattice. Two variational wave functions are compared: $|\Psi_{SL}\rangle$ and $|\Psi_{AF}\rangle$. Right panel: Variational results for $N(q)$ divided by $|q|$ for the $t/t' = 0.5$ case. The metal-insulator transition takes place between $U/t' = 4$ and $U/t' = 5$.

that the presence of backflow correlations, that strongly improve the accuracy of variational wave functions, reduces of an order of magnitude the antiferromagnetic order parameter Δ_{AF} , acting against the formation of magnetic order in the system, see Fig. (4.11). Moreover, the optimized t_{wf} in the wave function is also strongly renormalized in presence of backflow correlations, converging to zero as U is increased. These facts suggest a one-dimensionalization of the system and the one dimensional nature of the optimized wave function is clearly in contrast with the presence of bidimensional long-range order.

In order to analyze in more detail the effect of a finite Δ_{AF} , we have compared our variational energy, when the trial wave function contains a finite, optimized, magnetic order parameter Δ_{AF} , with the energy obtained within the spin-liquid guess for the ground state. For $U/t' \gtrsim 10$, the two energies coincide, within the error bar, and, remarkably, they are the same of a projected Fermi gas wave function, where no magnetic order parameter or BCS pairing is present. This result suggests that the ground state has no long-range magnetic order. On the contrary, for $5 \lesssim U/t' \lesssim 8$, a trial wave function with a finite Δ_{AF} is favoured. However, following the same procedure adopted for the square lattice, we have considered the Fixed Node results for the static spin-spin correlations $S(q) = \langle s_{-q} s_q \rangle$, using the non-magnetic wave function as the guiding one. Data show the absence of a long-range magnetic order in the lattice, even if there is an enhancement of spin-spin correlations at $q_x = \pi$, corresponding to some antiferromagnetic coupling along the

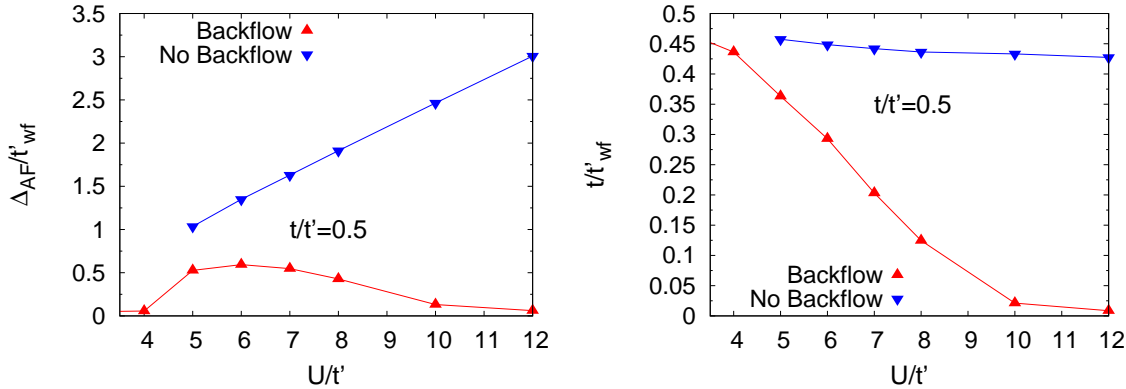


Figure 4.11: Left panel: Optimized antiferromagnetic order parameter Δ_{AF} , with and without backflow correlations, on a 144-site lattice with $t/t' = 0.5$. Right panel: Optimized hopping integral t_{wf} , with and without backflow correlations, on a 144-site lattice with $t/t' = 0.5$.

chains. Furthermore, there is no evidence of incommensurate peaks in $S(q)$, that would correspond to the presence of spiral magnetic order in the lattice.

The presence of a small Δ_{AF} could be just an artifact of the variational approach on a finite size; indeed, the presence of a magnetic order parameter allows more freedom in constructing the single-particle orbitals, which are the eigenstates of our mean-field Hamiltonian. In this respect, an extension of the BCS pairing to larger distances could be a promising tool to reduce the energy of the non-magnetic state, making it competitive with the energy obtained by means of a trial wave function with a finite Δ_{AF} . Indeed, a sizeable Δ_{BCS} that couples sites at a distance of three lattice spacings along the chains has been shown to improve the variational energy in the quasi-1D Heisenberg model [19].

The peculiar spin-liquid behaviour, described above, must be compared to the case in which the one-dimensional chains are coupled in a non-frustrated way, sketched in Fig. (4.12). In order to show that, within the same variational approach, it is possible to detect a strong antiferromagnetic coupling between chains with similar values of t/t' , but with a different geometry, we have compared two trial wave functions. The first one has a magnetic parameter such to induce antiferromagnetic correlations in both directions. The second one, instead, corresponds to have antiferromagnetic and ferromagnetic order along the strongest and the weakest bond, respectively. While the latter parameter is set to zero by the optimization procedure, the first one

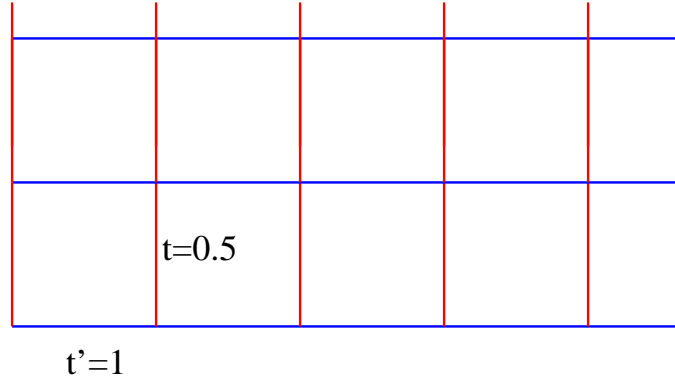


Figure 4.12: Square lattice with no rotation symmetry. Hopping integrals are $t' = 1$ and $t = 0.5$.

converges to a finite value, of order unity, with a substantial improvement in the variational energy. This result suggests that, even if t' is just one half of t , the square lattice is truly bidimensional, developing long-range antiferromagnetic Neel order.

In order to give more evidences to the absence of long-range magnetic order in the anisotropic triangular lattice with weakly coupled chains, we have studied in more details the static spin-spin correlations $S(q) = \langle s_{-q} s_q \rangle$. Following the same procedure adopted for the square lattice, we compare variational and Fixed Node results, by considering a non-magnetic wave function as the guiding one. In Fig. (4.13), we compare the static spin-spin correlations for the variational and for the Fixed Node calculations, at $U/t' = 10$ and $t/t' = 0.5$ for a 144-site lattice. For more clarity, we also show in Fig. (4.15) the data along a line of the Brillouin zone of the triangular lattice (the solid red line of Fig. (4.14)) In the variational calculation, $S(q)$ shows a clear one-dimensional behaviour: Spin-spin correlations are enhanced at $q_x = \pi$, corresponding to antiferromagnetic correlations along the chains and are completely flat in the direction orthogonal to the chains. In the Fixed Node calculation, there is actually the formation of a small peak at $(\pi, 0)$ ³, signaling the presence of some short-range bidimensional correlations. Indeed, even if there is a strong one-dimensionality in our system, some inter-chain coupling must be present, as detected by Fixed Node calculations for $S(q)$. However, as shown in Fig. (4.16), this small peak does not give rise to any sizeable long-range order, since

³The peak at $(\pi, 0)$ corresponds to a kind of coplanar order in which the spins in each chain are antiferromagnetically ordered in the x direction or in the y direction, alternatively.

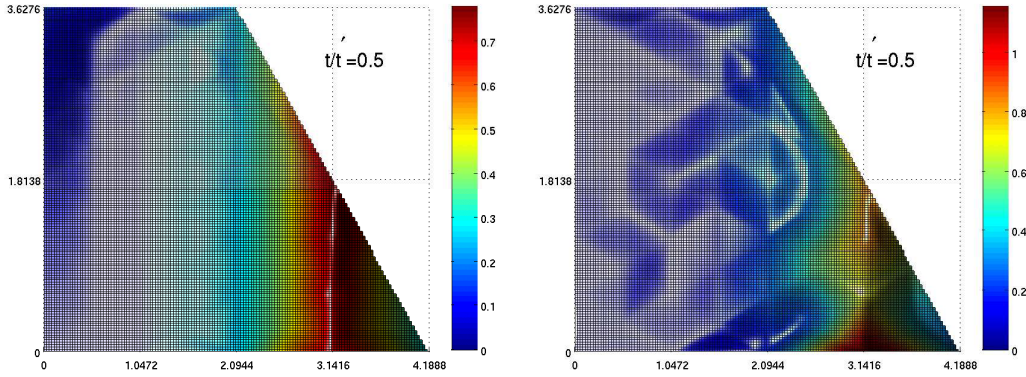


Figure 4.13: Left panel: Variational results for the static spin-spin correlations $S(q)$ at $U/t' = 10$ and $t'/t = 0.5$. Lattice sites are 144. Right panel: Fixed Node results for the static spin-spin correlations $S(q)$, with the same value of the parameters. Data are shown in the independent part of the Brillouin zone for the triangular lattice.

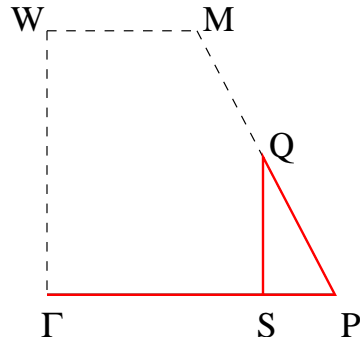


Figure 4.14: Sketch of the independent part of the Brillouin zone for the triangular lattice. Labelled points have coordinates: $\Gamma = (0, 0)$, $S = (\pi, 0)$, $P = (\frac{4\pi}{3}, 0)$, $Q = (\pi, \frac{\pi}{\sqrt{3}})$, $M = (\frac{2\pi}{3}, \frac{2\pi}{\sqrt{3}})$ and $W = (0, \frac{2\pi}{\sqrt{3}})$.

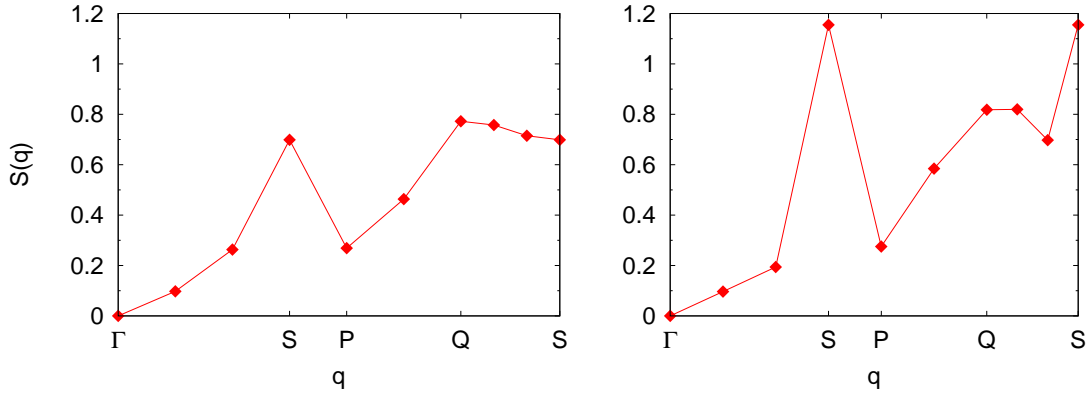


Figure 4.15: Left panel: Variational results for the static spin-spin correlations $S(q)$ along the red solid line of Fig. (4.14). Parameters are set to $U/t' = 10$, $t'/t = 0.5$ and 144 lattice sites. Right panel: Fixed Node results for the static spin-spin correlations $S(q)$, with the same value of the parameters, along the red solid line of Fig. (4.14).

$S(\pi, 0)/L$ approaches zero, or almost a very small value of magnetization, as the lattice size L is increased. Moreover, we would like to stress that there is no formation of incommensurate peaks in the Fixed Node calculations for $S(q)$, as shown in Fig. (4.13).

In conclusion, we have presented evidence that, in the anisotropic triangular lattice with $t' > t$, long-range magnetic order is destroyed or almost strongly suppressed. Moreover, short-range correlations may be strongly one-dimensional, since the optimized hopping parameter in the wave function t_{wf} is renormalized to zero and static spin-spin correlations $S(q)$ are enhanced for $q_x = \pi$. The particular nature of the best trial wave function, where no relevant long-range magnetic order or superconductive pairing can be stabilized, suggests that the ground state of this system could be a projected Fermi gas. Following Refs. [91, 92], this kind of wave function has a stable spinon Fermi surface, with low-lying spin excitations, that may lead to the linear behaviour observed in the heat capacity of $k - (\text{ET})_2\text{Cu}_2(\text{CN})_3$, when $T \rightarrow 0$ [84]. Also one-dimensionalization may explain the behaviour observed in Ref. [84], since one-dimensional chains with antiferromagnetic couplings are known to exhibit a large linear temperature-dependent contribution to the heat capacity.

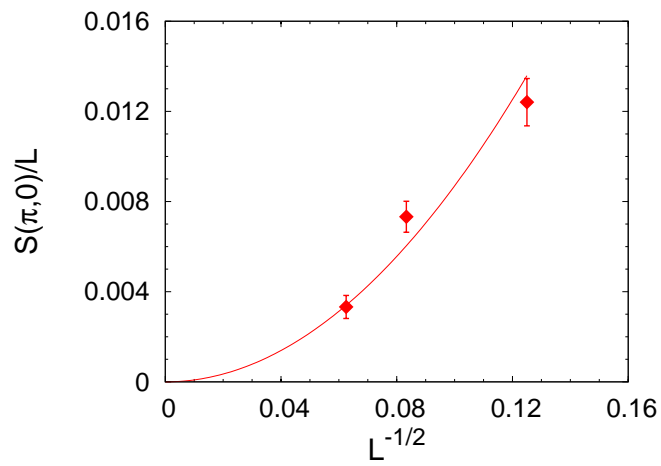


Figure 4.16: Fixed Node results for $S(\pi, 0)$ divided by the number of lattice sites $L = 64, 144$ and 256 , at $U/t' = 10$ and $t/t' = 0.5$. All the calculations have been done by using a non-magnetic wave function as the guiding one. The line is just a guide to the eye.

Conclusions and perspectives

In this thesis, we have treated the problem of strong correlation in 2D itinerant electron systems on a lattice. The primary interest in this subject comes from the fact that a sufficiently strong electron-electron repulsion may lead to unconventional phases. For example, in this limit, an insulating behavior with no magnetic order can be obtained, in contrast to what the independent-electron picture would naively predict. These insulators are usually called spin liquids and they naturally emerge in presence of frustrating interactions. Their behavior cannot be captured by any weak-coupling approach and novel techniques that may handle with strongly-correlated electrons are needed. In this respect, even simplified models, like the Hubbard one, where electrons hop among lattice sites and correlation is introduced through an on-site repulsive term U , cannot be exactly solved; then we need very accurate numerical techniques to describe their ground-state properties. A particularly insightful method is based upon the definition of a given variational ansatz, that defines an approximate ground-state wave function. Unfortunately, within previous conventional approaches, the accuracy of wave functions describing a spin liquid can be rather poor, especially in presence of frustration. Although a sufficiently long-range Jastrow factor is able to stabilize a disordered insulator [20], a magnetic ground state is always favoured in the insulating region. In order to overcome this problem, we have improved the trial wave functions by means of the so-called *backflow* correlations, which we have applied, for the first time, in a strongly correlated lattice model. This represents the first main result of the thesis.

Backflow correlations allow us to get a remarkably accurate ground-state energy in different regimes, both for conducting and insulating phases. We have compared our results with other techniques that have been proposed in the recent past. Backflow correlations turn out to be the most accurate approach among all the ones are usually considered to deal with the Hubbard model. In particular, the backflow wave function gives better energies than the ones obtained by the recently introduced Pfaffian state that combines magnetism with superconduct-

ing pairing [29]. Furthermore, only by including backflow correlations, we are able to reach the strong-coupling limit without losing accuracy [30].

The second main result of this thesis is the variational study of the ground-state properties for the Hubbard model on the *square lattice* with nearest and next-nearest neighbour hoppings [30], denoted by t and t' , respectively. We have determined with great accuracy the metal-insulator transition, occurring in this model, and have discussed the properties of both phases. In the metallic region, we have presented evidence that there is no relevant long-range superconductive pairing. In the insulating regime, our remarkable result is the stabilization of a spin-liquid phase at strong coupling $U \gtrsim 14$ and large enough frustrating ratio $t'/t \sim 0.7$. This result has been possible only by means of backflow correlations. Moreover, we have determined the boundaries of two magnetically ordered regions, the Neel antiferromagnetic one with pitch vector $\mathbf{Q} = (\pi, \pi)$ and the collinear one with pitch vector $\mathbf{Q} = (\pi, 0)$ or $\mathbf{Q} = (0, \pi)$. In particular, the insulator immediately close to the metallic region is magnetically ordered, with a first-order transition between the two magnetic phases at $t'/t = 0.78$.

We have compared our results on the square lattice with the ones obtained in Ref. [79], in which a similar variational Monte Carlo approach was used. We have shown that our ground-state energies are much more accurate than the ones obtained in Ref. [79]. Finally, in order to assess our variational results, we have applied Green's Function Monte Carlo, confirming the magnetic properties in the insulating region.

The third main result of this thesis is the study of the anisotropic *triangular lattice* [31]. We have considered two main regimes of anisotropy: the first one is the large inter-chain coupling limit, in which the lattice can be described as a set of squares coupled by t , frustrated by a weak diagonal bond t' . In this case, we have determined the metal-insulator transition and we have shown that the insulating phase is always accompanied by a magnetic order. Moreover, the magnetic ordering stays commensurate even close to the isotropic point $t' = t$. This result is in agreement with recent numerical calculations [88] and also with experiments performed in Ref. [9].

In the other case, that corresponds to a set of weakly coupled chains (i.e. $t \ll t'$), we have presented evidence that the insulator does not show any magnetic order and, therefore, it is a spin liquid. The nature of the ground state is compatible with a projected Fermi-sea (no magnetic order or superconductive pairing can be stabilized in the mean-field Hamiltonian that defines the variational wave function). More-

over, the system shows a strong one-dimensional behaviour, since the inter-chain hopping parameter of the mean-field Hamiltonian is renormalized to a very small value. Most importantly, the static spin-spin correlations present one-dimensional features. The spin-liquid nature of the ground state is in agreement with recent experiments on compounds with a triangular crystal structure [9, 11]; moreover, according to Refs. [91, 92], a projected Fermi sea has a stable spinon Fermi surface, with low-lying spin excitations, that may lead to the linear behaviour in the heat capacity of $k - (\text{ET})_2\text{Cu}_2(\text{CN})_3$, when $T \rightarrow 0$ [84]. Also one-dimensionalization may explain the behaviour observed in Ref. [84], since one-dimensional chains with antiferromagnetic couplings are known to exhibit a large linear temperature-dependent contribution to the heat capacity.

In summary, the new variational technique that has been introduced in this thesis opens a lot of perspectives for future works. Indeed, we have shown that its great accuracy and, in particular, its ability to recover the super-exchange mechanism in the spin liquid wave function make it a suitable candidate to study strongly correlated models on frustrated lattices, both in 2D and in 3D. In particular, backflow correlations can help us in giving a definite answer about the complete phase diagram of the anisotropic triangular lattice, from the limit $t' \rightarrow 0$ (that corresponds to a square lattice) to decoupled 1D chains ($t \rightarrow 0$). In this thesis, we have already presented important results in the two anisotropic regimes; immediate future work will be to treat the isotropic case, introducing a complex order parameter in the wave function, to reproduce the correct symmetries that are expected in this limit.

Acknowledgments

First of all, I would like to thank my supervisor Prof. Sandro Sorella for his support during my Ph.D. studies, which took origin from his pioneering idea of applying backflow correlations to a strongly interacting electron system on the lattice. His ability to understand the physics lying beyond the numerics has always been enlightening for me.

Then, I am also indebted to Federico Becca, who followed me during every-day work providing me with many useful tips. His incitements motivated me during these years, shaking, sometimes, my quietness :) Moreover, his careful reading of my thesis was of great help in improving the quality of the writing.

I acknowledge Prof. Alberto Parola for providing me with exact results on small clusters and for the irony with which he faces research.

I would like to mention also Manuela Capello for her help on the numerics during the early stage of this work.

Finally, I thank all the people who made my life in Trieste a unique experience: Giuliano, for all the time spent together, my loved flat-mates Carlotta, Valeria and in particular Marietta, that shared with me also the Ph.D. experience in Sissa, my great friends Mattia and Alice, my colleagues Paola, Marco S., Riccardo, Viet and Tatjana, Serena, Fabio, Lucio, Paolo, Francesco B., Marco M., Laura, Daniel, Nicola . . .

Bibliography

- [1] C. Kittel, *Introduction to Solid State Physics*, (John Wiley & Sons, Inc., 1953).
- [2] N.W. Ashcroft and N.D. Mermin, *Solid State Physics*, (Thomson Brooks/Cole, 1976).
- [3] G. Grosso and G. Pastori Parravicini, *Solid State Physics*, (Academic Press, 2000).
- [4] D. Pines and P. Nozières, *The theory of quantum liquids*, (Westview Press, Boulder, Colorado, 1989).
- [5] N.F. Mott, *Proc. Phys. Soc. (London)* **62**, 416 (1949).
- [6] M. Imada, A. Fujimori and Y. Tokura, *Rev. Mod. Phys.* **70**, 1039 (1998).
- [7] R.M. Martin, *Electronic Structure*, (Cambridge University Press, 2004).
- [8] A. Fujimori, I. Hase, H. Namatame, Y. Fujishima, Y. Tokura, H. Eisaki, S. Uchida, K. Takegahara and F.M.F. de Groot, *Phys. Rev. Lett.* **69**, 1796 (1992).
- [9] Y. Shimizu, K. Miyagawa, K. Kanoda, M. Maesato, and G. Saito, *Phys. Rev. Lett.* **91**, 107001 (2003).
- [10] Y. Kurosaki, Y. Shimizu, K. Miyagawa, K. Kanoda, and G. Saito, *Phys. Rev. Lett.* **95**, 177001 (2005).
- [11] R. Coldea, D.A. Tennant, A.M. Tsvelik and Z. Tylczynski, *Phys. Rev. Lett.* **86**, 1335 (2001).
- [12] J.S. Helton, K. Matan, M.P. Shores, E.A. Nytko, B.M. Bartlett, Y. Yoshida, Y. Takano, A. Suslov, Y. Qiu, J.-H. Chung, D.G. Nocera and Y.S. Lee, *Phys. Rev. Lett.* **98**, 107204 (2007).

- [13] O. Ofer, A. Karen, E.A. Nytko, M.P. Shores, B.M. Bartlett, D.G. Nocera, C. Baines and A. Amato, cond-mat/0610540 (2006).
- [14] P. Mendels, F. Bert, M.A. de Vries, A. Olariu, A. Harrison, F. Duc, J.C. Trombe, J.S. Lord, A. Amato and C. Baines, *Phys. Rev. Lett.* **98**, 077204 (2007).
- [15] N. Trivedi and D.M. Ceperley, *Phys. Rev. B* **41**, 4552 (1990).
- [16] M. Calandra and S. Sorella, *Phys. Rev. B* **57**, 11446 (1998).
- [17] D.F.B. ten Haaf, H.J.M. van Bommel, J.M.J. van Leeuwen, W. van Saarloos, and D.M. Ceperley, *Phys. Rev. B* **51**, 13039 (1995).
- [18] L. Capriotti, F. Becca, A. Parola, and S. Sorella, *Phys. Rev. Lett.* **87**, 097201 (2001).
- [19] S. Yunoki and S. Sorella, *Phys. Rev. B* **74**, 014408 (2006).
- [20] M. Capello, F. Becca, M. Fabrizio, S. Sorella, and E. Tosatti, *Phys. Rev. Lett.* **94**, 026406 (2005).
- [21] R.P. Feynman and M. Cohen, *Phys. Rev.* **102**, 1189 (1956).
- [22] M.A. Lee, K.E. Schmidt, M.H. Kalos, and G.V. Chester, *Phys. Rev. Lett.* **46**, 728 (1981).
- [23] K.E. Schmidt, M.A. Lee, M.H. Kalos, and G.V. Chester, *Phys. Rev. Lett.* **47**, 807 (1981).
- [24] Y. Kwon, D.M. Ceperley, and R.M. Martin, *Phys. Rev. B* **48**, 12037 (1993).
- [25] Y. Kwon, D.M. Ceperley, and R.M. Martin, *Phys. Rev. B* **58**, 6800 (1998).
- [26] M. Holzmann, D.M. Ceperley, C. Pierleoni, and K. Esler, *Phys. Rev. E* **68**, 046707 (2003).
- [27] N.D. Drummond, P. López Ríos, A. Ma, J.R. Trail, G.G. Spink, M.D. Towler and R.J. Needs, *J. Chem. Phys.* **124**, 224104 (2006); P. López Ríos, A. Ma, N.D. Drummond, M.D. Towler and R.J. Needs, *Phys. Rev. E* **74**, 066701 (2006).
- [28] A. H. MacDonald, S.M. Girvin and D. Yoshioka, *Phys. Rev. B* **37**, 9753 (1988).
- [29] J.P. Bouchaud, A. Georges and C. Lhuillier, *J. de Physique* **49**, 553 (1988).

- [30] L.F. Tocchio, F. Becca, A. Parola and S. Sorella, *Phys. Rev. B* **78**, 041101(R) (2008).
- [31] L.F. Tocchio, F. Becca and S. Sorella, in preparation.
- [32] J.G. Bednorz and K.A. Müller, *Z. Phys. B* **64**, 189 (1986).
- [33] M. Foex, *C. R. Hebd. Sean. Acad. Sci. B* **223**, 1126 (1946); D.B. McWhan and J.P. Remeika, *Phys. Rev. B* **2**, 3734 (1970).
- [34] D.B. McWhan, A. Menth, J.P. Remeika, W.F. Brinkman and T.M. Rice, *Phys. Rev. B* **7**, 1920 (1973).
- [35] R.H. McKenzie, *Comments Condens. Matter Phys.* **18**, 309 (1998) and references therein.
- [36] P. Lecheminant, B. Bernu, C. Lhuillier, L. Pierre and P. Sindzingre, *Phys. Rev. B* **56**, 2521 (1997); R. Budnik and A. Auerbach, *Phys. Rev. Lett.* **93**, 187205 (2004).
- [37] J.T. Chalker and J.F.G. Eastmond, *Phys. Rev. B* **46**, 14201 (1992).
- [38] Ch. Waldtmann, H.-U. Everts, B. Bernu, C. Lhuillier, P. Sindzingre, P. Lecheminant and L. Pierre, *Eur. Phys. J. B* **2**, 501 (1998).
- [39] C. Castelnovo, R. Moessner and S.L. Sondhi, *Nature* **451**, 42 (2008).
- [40] P.W. Anderson, *Science* **235**, 1196 (1987).
- [41] X.-G. Wen *Phys. Rev. B* **65**, 165113 (2002).
- [42] J. Hubbard, *Proc. Roy. Soc. London A* **276**, 238 (1963).
- [43] M.C. Gutzwiller, *Phys. Rev. Lett.* **10**, 159 (1963).
- [44] J. Kanamori, *Progr. Theor. Phys.* **30**, 275 (1963).
- [45] E.H. Lieb and F.Y. Wu, *Phys. Rev. Lett.* **20**, 1445 (1968).
- [46] T.A. Maier, M. Jarrell, T.C. Schulthess, P.R.C. Kent and J.B. White, *Phys. Rev. Lett.* **95**, 237001 (2005).
- [47] J.E. Hirsch, *Phys. Rev. B* **31**, 4403 (1985).
- [48] I. Affleck, *J. Phys. A: Math. Gen.* **31**, 4573 (1998).

- [49] S. Sorella, G.E. Santoro and F. Becca, *SISSA Lecture notes on numerical methods for strongly correlated electrons*,
http://www.sissa.it/cm/index.php?contents=phd/phd_time.htm
- [50] N. Metropolis, A. Rosenbluth, M. Rosembluth, A. Teller and E. Teller, *J. Chem. Phys.* **21**, 1087 (1953).
- [51] S. Sorella, *Phys. Rev. B* **64**, 024512 (2001).
- [52] C. Lanczos, *J. Res. Nat. Bur. Stand.* **45**, 255 (1950).
- [53] E.S. Heeb and T.M. Rice, *Europhys. Lett.* **27**, 673 (1994).
- [54] P. Chandra and B. Doucot, *Phys. Rev. B* **38**, 9335(R) (1988).
- [55] E. Manousakis, *Rev. Mod. Phys.* **63**, 1 (1991); Z. Liu and E. Manousakis, *Phys. Rev. B* **40**, 11437(R) (1989); F. Franjic and S. Sorella, *Prog. Theor. Phys.* **97**, 399 (1997).
- [56] B. Edegger, V.N. Muthukumar and C. Gros, *Adv. Phys.* **56**, 927 (2007).
- [57] M.C. Gutzwiller, *Phys. Rev. Lett.* **10**, 159 (1963).
- [58] T.A. Kaplan, P. Horsch and P. Fulde, *Phys. Rev. Lett.* **49**, 889 (1982).
- [59] H. Yokoyama and S. Shiba, *J. Phys. Soc. Jpn.* **56**, 1490 (1987).
- [60] W. Metzner and D. Vollhardt, *Phys. Rev. Lett.* **59**, 121 (1987).
- [61] P. Fazekas and K. Penc, *Int. J. Mod. Phys. B* **1**, 1021 (1988).
- [62] H. Yokoyama and H. Shiba, *J.Phys.Soc. Jpn.* **59**, 3669 (1990).
- [63] W.L. McMillan, *Phys. Rev.* **138**, A442 (1965).
- [64] L. Reatto and G.V. Chester, *Phys. Rev.* **155**, 88 (1967).
- [65] G. Gaglione, G.L. Masserini and L. Reatto, *Phys. Rev. B* **22**, 1237 (1980).
- [66] P.A. Whitlock, D.M. Ceperley, G.V. Chester and M.H. Kalos, *Phys. Rev. B* **19**, 5598 (1979).
- [67] T. MacFarland, S.A. Vitiello, L. Reatto, G.V. Chester and M.H. Kalos, *Phys. Rev. B* **50**, 13577 (1994).
- [68] F. Becca, Ph.D. thesis (SISSA, Trieste),
<http://www.sissa.it/cm/phd.php>

- [69] J. Carlson, S.-Y. Chang, V.R. Pandharipande and K.E. Schmidt, *Phys. Rev. Lett.* **91**, 050401 (2003); M. Bajdich, L. Mitas, G. Drobný, L.K. Wagner and K.E. Schmidt, *Phys. Rev. Lett.* **96**, 130201 (2006).
- [70] C. Weber, A. Lauchli, F. Mila and T. Giamarchi, *Phys. Rev. B* **73**, 014519 (2006).
- [71] M. Lugas, L. Spanu, F. Becca and S. Sorella, *Phys. Rev. B* **74**, 165122 (2006); L. Spanu, M. Lugas, F. Becca and S. Sorella, *Phys. Rev. B* **77**, 024510 (2008).
- [72] D. Eichenberger and D. Baeriswyl, *Phys. Rev. B* **76**, 180504(R) (2007).
- [73] H.Q. Lin and J.E. Hirsch, *Phys. Rev. B* **35**, 3359 (1987).
- [74] J.E. Hirsch, *Phys. Rev. B* **31**, 4403 (1985); S. Sorella, S. Baroni, R. Car and M. Parrinello, *Europhys. Lett.* **8**, 663 (1989).
- [75] T. Kashima and M. Imada, *J. Phys. Soc. Jpn.* **70**, 3052 (2001).
- [76] H. Morita, S. Watanabe, and M. Imada, *J. Phys. Soc. Jpn.* **71**, 2109 (2002).
- [77] T. Mizusaki and M. Imada, *Phys. Rev. B* **74**, 014421 (2006).
- [78] M. Imada and T. Kashima, *J. Phys. Soc. Jpn.* **69**, 2723 (2000); T. Kashima and M. Imada, *J. Phys. Soc. Jpn.* **70**, 2287 (2001); T. Mizusaki and M. Imada, *Phys. Rev. B* **69**, 125110 (2004).
- [79] H. Yokoyama, M. Ogata, and Y. Tanaka, *J. Phys. Soc. Jpn.* **75**, 114706 (2006).
- [80] A.H. Nevidomskyy, C. Scheiber, D. Senechal, and A.-M.S. Tremblay, *Phys. Rev. B* **77**, 064427 (2008).
- [81] M. Potthoff, M. Aichhorn and C. Dahnken, *Phys. Rev. Lett.* **91**, 206402 (2003).
- [82] M. Capello, Ph.D. thesis (SISSA, Trieste), <http://www.sissa.it/cm/phd.php>
- [83] F. Becca, L. Capriotti and S. Sorella, *Phys. Rev. Lett.* **87**, 167005 (2001)
- [84] S. Yamashita, Y. Nakazawa, M. Oguni, Y. Oshima, H. Nojiri, Y. Shimizu, K. Miyagawa and K. Kanoda, *Nature Physics* **4**, 459 (2008).

- [85] P. Sahebsara and D. Sénéchal, *Phys. Rev. Lett.* **100**, 136402 (2008).
- [86] H.R. Krishnamurthy, C. Jayaprakash, S. Sarker and W. Wenzel, *Phys. Rev. Lett.* **64**, 950 (1990).
- [87] J. Liu, J. Schmalian and N. Trivedi, *Phys. Rev. Lett.* **94**, 127003 (2005).
- [88] T. Watanabe, H. Yokoyama, Y. Tanaka and J. Inoue, cond-mat/07111702 (2007).
- [89] Y. Hayashi and M. Ogata, *J. Phys. Soc. Jpn.* **76**, 053705 (2007).
- [90] D. Heidarian, private communication.
- [91] O.I. Motrunich, *Phys. Rev. B* **72**, 045105 (2005).
- [92] S.-S. Lee and P.A. Lee, *Phys. Rev. Lett.* **95**, 036403 (2005).
- [93] B.J. Powell and R.H. McKenzie, *Phys. Rev. Lett.* **98**, 027005 (2007).
- [94] N. Trivedi, private communication.
- [95] T. Watanabe, H. Yokoyama, Y. Tanaka and J. Inoue, *J. Phys. Soc. Jpn.* **75**, 074707 (2006).
- [96] O.A. Starykh and L. Balents, *Phys. Rev. Lett.* **98**, 077205 (2007).